Nonlinear Applications using Silicon Nanophotonic Wires

Xiaoping Liu

Submitted in partial fulfillment of the
requirements for the degree
of Doctor of Philosophy
in the Graduate School of Arts and Sciences

COLUMBIA UNIVERSITY

2011

ABSTRACT

Nonlinear Applications using Silicon Nanophotonic Wires

Xiaoping Liu

This thesis is concerned with an emerging set of nonlinear-optical applications using silicon nanophotonic "wires" fabricated on a silicon-on-insulator photonic chip. These deeply scaled silicon nanophotonic wires are capable of confining the telecom and mid-infrared (mid-IR) light tightly into an optical-modal area ~ 0.1 μm^2. The tight optical confinement leads to many advantageous physical properties including enhanced effective nonlinearity, flexible control of waveguide dispersion, and short free-carrier lifetime. All these advantages make silicon nanophotonic wires an ideal platform for a variety of nonlinear applications.

The first part of my thesis study is focused on nonlinear applications in the telecom bands. In Chapter 3, I study the frequency dependence of optical nonlinearity in silicon nanophotonic wires, and its influence on the propagation of ultra-short optical pulses in such wires. I show that silicon nanophotonic wires possess a remarkably large characteristic time associated with the self-steepening effect and optical-shock formation. In Chapter 4, I present an experimental demonstration of an ultrafast cross-phase-modulation-based wavelength-conversion (XPM-WC) technique for telecom RZ-OOK data. I also investigate the effect of pump-probe detuning on the efficacy of this XPM-WC technique. In Chapter 5, I show a (primarily) numerical study of a method for dispersion-engineering of silicon nanophotonic wires using a conformal thin-silicon-nitride dielectric film deposited around the silicon wire core. My simulation results show

that this approach may be used to achieve the dispersion characteristics required for broadband phase-matched four-wave-mixing processes, while simultaneously maintaining strong modal confinement within the silicon core for high effective nonlinearity.

The second part of my thesis is devoted to investigations of nonlinear applications in mid-IR spectral region, in which nonlinear optical loss due to parasitic two-photon absorption can be significantly reduced and therefore a large nonlinear figure of merit can be achieved in order to facilitate efficient nonlinear processes. In Chapter 6, I present an experimental demonstration of a mid-IR-silicon-nanophotonic-wire optical parametric amplifier with 25.4 dB on-chip gain. This gain achieved with only a 4-mm-long silicon nanophotonic wire is sufficient enough to overcome all the insertion loss, resulting in 13 dB net off-chip amplification. In addition, I show, on the same waveguide, efficient generation of 4 orders of cascaded FWM products enabled by the large on-chip gain. In Chapter 7, I report a comprehensive study of the propagation characteristics of a picosecond pulse through a 4-mm-long silicon nanophotonic wire with normal dispersion with excitation wavelengths crossing the mid-infrared two-photon absorption edge at λ = 2200 nm. Significant reduction in nonlinear loss due to two-photon absorption is demonstrated as the excitation wavelengths approach 2200 nm. Self-phase modulation at high input power is also observed. Analysis of experimental data and comparison with numerical simulations illustrates that the two-photon absorption coefficient obtained from nanophotonic wire measurements is in reasonable agreement with prior measurements of bulk silicon crystals, and that bulk silicon values of the nonlinear refractive index can be confidently incorporated in the modeling of pulse propagation in deeply-scaled waveguide structures. In Chapter 8, I investigate a higher-order phase matching technique utilizing the 4th-order dispersion term for realizing a broadband or discrete band parametric process in silicon nanophotonic wires. I demonstrate experimentally, on a silicon nanophotonic wire designed to exhibit a desired 2nd-order and 4th-order dispersion, broadband/discrete-band modulation instability and 50 dB Raman assisted parametric gain.

Table of Contents

List of Figures

List of Tables

Acknowledgements

I feel really honored and privileged to spend the past four years at Columbia University studying towards my doctoral degree. During this period, I received continuous help, support and encouragement from many people around me. This thesis would not be possible without them.

First and foremost, I own my deepest gratitude to **Professor Richard M. Osgood Jr.**, a great advisor and mentor to me both academically and intellectually. His enthusiasm in science and engineering inspired me from the beginning of my graduate study. His continuous encouragement and guidance helped me in all the time of research and writing of this thesis, made me realize my own capacities, and more importantly facilitated my transition from a student to a mature researcher. I could not have imaged having a better advisor and mentor for my Ph.D. study.

Secondly, my sincere appreciation goes to many amazing collaborators that I have had the honor to work with on diverse exciting projects. I thank **Dr. Yurii A. Vlasov** and **Dr. William M. J. Green** from IBM T. J. Watson Research Center for offering me the summer internship opportunities in their group and leading me exploring a new field. Dr. Green's investment in several key equipments made possible major part of my thesis work. His technical support helped me overcome many hurdles in several projects. I am truly grateful to Dr. Green since I have benefited a great deal from working with him. I also thank **Professor Gary Carter** and **Dr. William Astar** from University of Maryland at Baltimore County for giving me the opportunities to conduct several experiments in their lab and for their kind help and suggestions during the experiments.

Thirdly, I extend my thanks to my colleagues in the Osgood Research Group, all of whom have contributed so much to my studies and lives in their own way: **Jerry I. Dadap**, **Nicolae C. Panoiu**, **Xiaogang Chen**, **I-Wei Hsieh**, **Tsung-Liang Chen**, **Lina Cao**, **Jeffrey B. Driscoll**, **Ophir Gaathon**, **Avishai Ofan**, **Richard Grote**, **Kevin Knox**, **Nader Zaki** and **Denis Potapenko**.

Last and most importantly, I would like to thank my wonderful parents and my dearest wife, **Jie Ren**. I thank them for pushing me to be the best and for their unconditional support in every aspect of my life.

Chapter 1

Introduction

1.1 Silicon as a photonic platform

Photonic technology becomes increasing important due to its potential for helping the microelectronics industry to maintain “Moore’s law” scaling. This law describes the trend of doubling the performance in a computational system every 18 months. Prior to year 2000, the performance of a microprocessor could be scaled by increasing its clock frequency. However, when the clock frequency reaches a few GHz, further increasing the clock frequency to improve the performance becomes problematic since power dissipation scales nonlinearly with the clock frequency, power efficiency drops dramatically, and the resulting thermal density in the microprocessor becomes difficult to maintain [1]. Multiprocessor architecture has been developed to overcome this thermal density issue. However, as the number of integrated processors increase, the microprocessor becomes more and more demanding in bandwidth for both on-chip and off-chip communication, and the electric communication network traditionally built inside the multiprocessor eventually reaches its bandwidth limit and becomes the performance bottleneck. By manipulating photons instead of electrons, this bandwidth limitation on the microprocessor may be overcome thanks to the tremendous available bandwidth of optical carriers. For this application, silicon photonics, built on silicon-on-insulator platform, is a promising way to tackle the chip-level bandwidth issue by developing a number of CMOS compatible integration technologies with a high level of functionality that can address a broad range of applications. In addition, commercial CMOS fabrication compatibility is a major advantage and driving force for the silicon integrated photonic platform. Once this CMOS photonic platform technology becomes mature, it may have an impact far beyond chip-scale applications and perhaps even revolutionize the entire telecommunication and/or system communication industry by bringing in highly reliable, low-cost, ultra-compact and high-speed photonic components.

Silicon, as the foundation of modern microelectronics industry, is heavily researched and by far the most understood semiconductor material. The ideas for using silicon as a promising photonic material for photonic and optoelectronic devices have been pioneered by Soref through 1980s – 1990s [2-4]. Throughout the past decade, with the help of advanced fabrication techniques, a consistent number of breakthroughs in silicon photonic platform have been achieved. First silicon waveguide propagation loss has been reduced dramatically [5-10]. Second, efficient coupling methods for power coupling from fiber to waveguide have been developed, e.g. a SU8 polymer edge coupler [11], a SiON edge coupler [12, 13], a nano-taper [14], and a vertical grating coupler [15-17]. In addition, many high-performance passive photonic building blocks have been successfully demonstrated such as optical buffers [18] and delay lines [19-21], optical add/drop filters [22-24], and wavelength-division-multiplexers/demultiplexers [25-29]. Furthermore, many active devices have also been demonstrated; these include Raman Lasers [30-33], high-speed electro-optical modulators [34-37] and switches [12, 38], signal regenerators [39], parametric wavelength converters [6, 40-44] and parametric amplifiers [45-47], high speed Silicon/Germanium integrated photodetectors [48, 49] and so forth. Finally, although most of the research activities in this area remain device oriented, especially at universities, part of the research focus has been geared towards the system-integration side and towards product development as illustrated by the recent CMOS photonic technologies developed by Luxtera, Kotura, Lightwire, Ghent University-IMEC, Intel and IBM.

1.2 Silicon's optical properties

When considered for photonic applications, silicon has many attractive optical properties. It has a band gap of ~ 1.12 eV at room temperature corresponding to a wavelength of 1.1 μm and thus is transparent over the most important wavelength windows between 1.3 μm to 1.7 μm for telecommunication applications. Silicon is by far the purest material made by man, so it is possible to make low-absorption and low-impurity-scattering optical waveguides. In addition, silicon's index of refraction at the telecommunication bands is very high ($n_{\mathrm{Si}} \sim 3.5$) compared with that of the common cladding dielectrics in CMOS processes (air: $n_{\mathrm{air}} \sim 1$; silicon dioxide: $n_{\mathrm{SiO_2}} \sim 1.45$; silicon nitride: $n_{\mathrm{Si_3N_4}} \sim 2$). This large index contrast gives rise to very tight optical confinement, high photonic-integration density and small optical circuit foot-print.

The phase of optical waves travelling in silicon waveguides can be manipulated by changing the index of refraction through electro-optical and/or thermo-optical effects to create various photonic devices such as modulators and switches. However, silicon has a negligible linear electro-optical (Pockels) effect because its crystal lattice is centro-symmetric. In addition, under typical conditions the Kerr effect in silicon is much weaker than the plasma dispersion caused by free carriers. For example, with an applied electrical field close to the silicon's breakdown field ~ 3×10^5 V/cm [50], the change of refractive index, Δn, in silicon is less than 10^{-4} at λ = 1.55 μm. However, with a moderate carrier-injection level $N_{\text{e-h}}$ ~ 10^{18} cm^{-3}, the index of refraction change can be as large as $\Delta n \sim 2\times10^{-3}$ at λ = 1.55 μm [51]. Such a readily available index-of-refraction change makes the plasma dispersion the most widely used electro-optical modulation method in silicon. It is also important to note that the injected free carriers in silicon not only change the index of refraction but also introduce additional loss originating from the interaction of optical field with the carriers. Finally, silicon has very large thermo-optical coefficient ($dn/dT = 1.84\times10^{-4}$ K^{-1} at λ = 1.55 μm) and high thermal conductivity (1.4 W/cm-K), which allow for fast response and low-power operation in thermally tuned silicon photonic devices [52-55]. In fact, the thermal-optical effect is widely used to study modulators and switching devices because of ease in fabrication compared with the junction-based carrier-injection method.

1.3 Silicon waveguides

Optical waveguides are fundamental components of integrated photonic circuits because they act as the signal transportation medium and provide the basic connectivity among various components. The widely used silicon nanophotonic “wires” are typically patterned on silicon-on-insulator (SOI) wafers with a silicon-photonic-layer thickness of from several hundred nanometers to a few micrometers. These SOI wafers are readily available on the commercial market because of the use in the microelectronic industry. A buried oxide (BOX) layer is inserted in between the thin silicon photonic layer and the silicon substrate to optically isolate them. The thickness of this buried oxide layer is typically larger than 1 μm to enable a good optical isolation at the telecommunication bands [56]. A thicker BOX layer is often used for devices operating in longer-wavelength region [47]. The top dielectric cladding of a silicon nanophotonic "wire" varies depending on the specific application. The family of silicon waveguides extensively used in research can be loosely divided into rib and strip waveguide according geometry configuration. Single-mode rib silicon waveguides are dominantly used by Intel [57] and have a cross-section area usually larger than 1 μm^2. The most obvious advantage of such waveguides is their low propagation loss (~ 0.1 dB/cm) [6]. However, the foot-print of photonic devices using these waveguide tends to be "bulky" preventing high density integration since the radii of waveguide bends cannot be too small without significant loss. In addition, TPA-generated free carriers live much longer in wide waveguides than in narrow single-mode waveguides, and as a result often a reverse bias p-i-n diode needs to be used to actively remove free carriers to reduce the loss by FCA. Single-mode silicon strip waveguides typically have extremely small cross-section area ~ 0.1 μm^2. Such waveguides are sometimes called silicon nanophotonic "wires". Figure 1-1 shows a scanning electron microscope (SEM) picture of a typical silicon nanophotonic wire fabricated on a CMOS pilot line in IBM T. J. Watson Research Center. As illustrated in Figure 1-1 by the overlayed modal profile for the fundamental quasi-TE mode (major electrical field parallel to silicon-BOX interface), the silicon nanophotonic wire has very tight optical confinement at λ = 1.55 μm due to the large refractive index contrast despite its sub-micrometer dimension ($w \times h$ = 400 × 220 nm). Typical linear propagation losses are in the range of 2 – 4 dB/cm [5, 45, 58] depending on the dimensions and processing conditions for such silicon nanophotonic wires. Due to the large surface to volume ration, the free-carrier lifetime in silicon nanophotonic wires can be less than 1 ns [34, 59] as opposed to tens of ns in silicon rib waveguides used by Intel [31]. Tight bends are possible in these silicon nanophotonic wires as illustrated by the example of a 6.5 μm bend radius with a measured bend losing ~ 0.005 dB per 90° bend [18]. These single-mode silicon nanophotonic wires can be used to build a robust compact high speed transmission link as demonstrated in Ref [60].

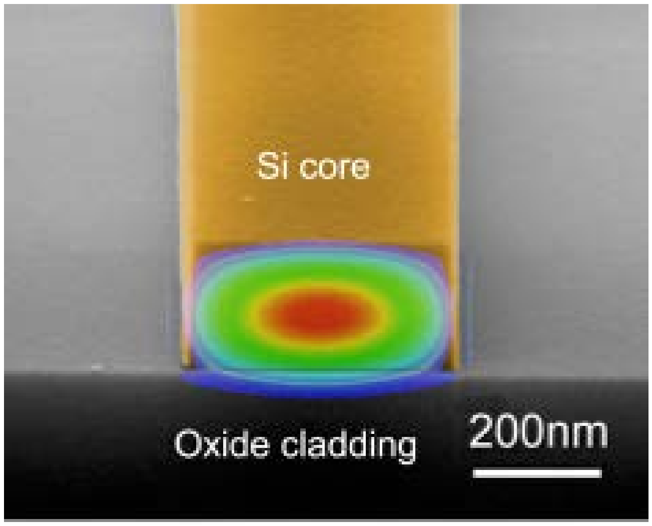

Figure 1-1 A SEM picture of a typical silicon nanophotonic wire overlayed with its fundamental quasi-TE mode profile at λ = 1.55 μm. (Courtesy of Dr. William Green from IBM T. J. Watson Research Center)

In addition, there also exist other types of silicon waveguides. Silicon slot waveguides, first proposed by researchers at Cornell University [61, 62], consisted of two silicon strips separated by a subwavelength-scale low refractive index slot region, where the light is strongly confined. However, this kind of waveguides does not benefit from silicon's photonic properties, since the optical modal overlap with silicon is minimal. In order for the silicon slot waveguides to be more useful, the slot region is usually filled with other materials that can bring added functionalities into the system, e.g. Er-doped-

SiO_2 for light emission/amplification [63] and organic materials with a large nonlinearity for all optical signal processing [64]. However, incorporating these functional components may also introduce major constrains for a CMOS compatible process. Last, a low-loss etchless silicon waveguide was demonstrated by the same group of researchers at Cornell University [8]. Selective oxidation was used to define the silicon waveguide instead of using an etch mask and plasma assisted chemical etching. Using this fabrication technique, the waveguide's sidewall was found to be ultra-smooth with width variation of 0.3 nm and waveguide loss was as low as ~ 0.3 dB/cm at λ = 1.55 μm. The disadvantage of this kind of waveguide is its low optical confinement, and thus large minimum bending radius.

1.4 Nonlinear applications in silicon waveguides

Besides acting as the fundamental building blocks for a photonic communication network, the silicon waveguide platform can also be an ideal host for a variety of ultra-fast nonlinear applications. Silicon is particularly useful in these cases, since it has a very large bulk optical nonlinearity in the telecommunication bands [65, 66]. Table 1-1 shows a comparison of physical properties for a single-mode fiber and a silicon nanophotonic wire. For example, the nonlinear refractive index of bulk silicon is $n_2 \sim 4\times10^{-14}\ \mathrm{cm}^2/\mathrm{W}$, more than two orders of magnitude larger than that of silicon dioxide ($n_2 \sim 2\times10^{-16}\ \mathrm{cm}^2/\mathrm{W}$).

The large index contrast in silicon nanophotonic wires further enhances the effective optical nonlinearity by means of a reduced optical modal area. Because the optical intensity in a waveguide is inversely proportional to the optical modal area, small modal area leads to very large optical intensity for a given optical power. The optical modal area in a typical silicon nanophotonic wire is ~ 0.1 μm^2, which is about 10^3 times less than the modal area of single-mode fiber ~ 10^2 μm^2. This large reduction in optical modal area gives rise to an effective optical nonlinearity in silicon nanophotonic wires that is 10^5 times larger than that of single-mode fiber. Such large effective nonlinearity enables silicon nanophotonic-wire-based nonlinear devices to be deeply "scaled down" to a device length on the order of a centimeter as opposed to a few kilometers in an optical fiber system.

Table 1-1 Comparison of physical properties: single mode fiber versus silicon nanophotonic wire.

	Single mode fiber (SMF28)	Silicon nanophotonic wire	ratio
Bulk material (n_2)	$\sim 4\times10^{-14}\,\text{cm}^2/\text{W}$	$\sim 2\times10^{-16}\,\text{cm}^2/\text{W}$	~ 10^2
Effective optical modal area (A_{eff})	~ 100 μm^2	~ 0.1 μm^2	~ 10^3
Effective nonlinear parameter (γ)	~ 1 $W^{-1}km^{-1}$	~ 100 $W^{-1}m^{-1}$	~ 10^5
Typical device length (L)	~ 1 km	~ 1 cm	~ 10^5
Dispersion parameter (D_λ)	~ 16 ps/nm-km	Can be dispersion engineered	

Over the past decade, various fundamental nonlinear effects have been demonstrated in silicon nanophotonic wires such as self-phase modulation (SPM) [67, 68], cross-phase modulation (XPM) [69], and optical-soliton propagation [70, 71] and supercontinuum generation [72, 73], and many important applications using these nonlinear effects have also been proposed and demonstrated, e.g. all optical switching [74-76] and data-format conversion [77-80]. In addition, the large index contrast also offers great flexibility for control of waveguide dispersion by manipulating the geometric dispersion contribution. Such phase matching is necessary for phase coherent nonlinear processes such as four-wave mixing (FWM) [81]. Waveguide dispersion can be easily engineered by choosing different cross-section dimensions and/or varying cladding materials and their thickness [82, 83]. Using silicon nanophotonic wires exhibiting anomalous dispersion properties, very broadband parametric processes have been realized in the telecommunication bands [84].

1.5 Silicon photonic in mid-infrared region

Though silicon has a very large optical nonlinearity in the telecommunication bands, it also exhibits strong two-photon absorption (TPA) [66]. Single-photon absorption in silicon stops at λ = 1.1 μm, but silicon continues to absorb via a two-photon process for photon wavelengths up-to λ = 2.2 μm. This process generates free carriers, which then create free-carrier absorption (FCA) to further absorb optical power. This process is described in the form of carrier injection as discussed in Section 1.2. Certain application such as all optical signal modulation and switching could benefit from this strong TPA in silicon [75], because it allows for fast carrier injection by optically “bombarding” the silicon. However, TPA and its induced FCA introduce strong nonlinear optical limiting in the telecommunication bands, which places a restriction on the achievable power level in the silicon nanophotonic wires [68]. The efficiency of parametric processes in this wavelength region is severely limited, and it is shown that even in a pulsed measurement , the achievable parametric gain is restricted to only a few decibels [45].

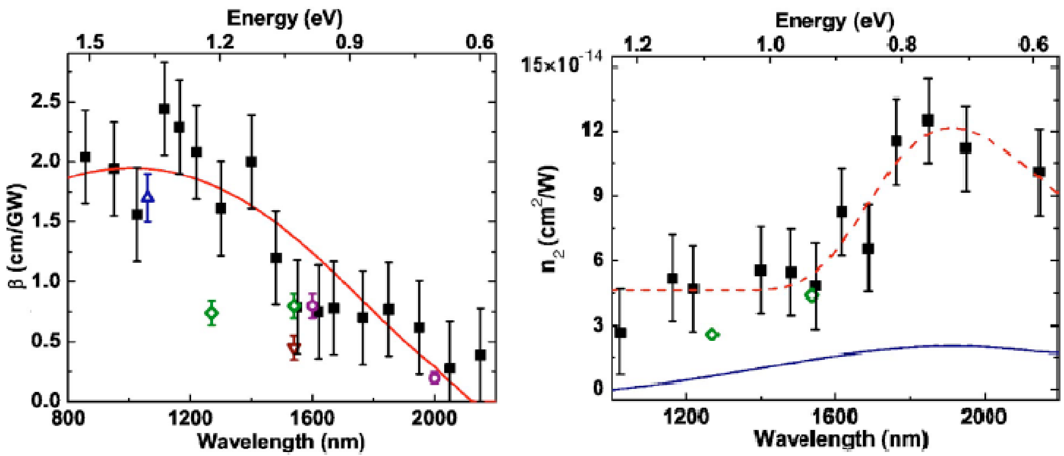

Figure 1-2 Measured wavelength dependent TPA coefficient β_{TPA} and nonlinear refractive index n_2 for bulk silicon [66].

While the strong TPA in the telecommunication bands is a major obstacle to efficient nonlinear processes, in the case of long-wavelength photonic device applications in the mid-infrared (mid-IR), TPA absorption is small to nonexistent. Based on the experimentally measured frequency-dependant material nonlinear properties of bulk silicon shown in Figure 1-2, the nonlinear loss by TPA can be significantly reduced when the photon energy approaches half of silicon's bandgap ~ 0.56 eV, which corresponds to a wavelength of ~ 2.2 μm. Consequently in this wavelength region, the Si nonlinear figure of merit (FOM), defined as $n_2/(\beta_{TPA}\lambda)$, where n_2 is the Kerr nonlinearity, β_{TPA} is the two-photon absorption coefficient, and λ is the wavelength, should be dramatically increased if the excitation wavelength is moved from telecommunication bands to the mid-Infrared (mid-IR) (λ > 2.0 μm). In this case, the resultant large figure of merit makes possible the construction of highly efficient nonlinear optical devices using the silicon platform, some of which are essential for ultra-high speed optical communication in all optical domains. For example, as in the case of telecommunication, a broadband optical amplifier is a key element used to boost the power level in all optical channels avoiding the use of complicated optical-electric-optical signal repeating system. Silicon's large nonlinear FOM may make possible a broadband parametric-process-based optical amplifier, which is otherwise not allowed in silicon through electrical pumping due to the nature of its indirect band-gap.

Indeed a mid-IR bulk silicon Raman amplifier has been successfully experimentally demonstrated [85] and a waveguide silicon parametric oscillator working at mid-IR wavelength region has been proposed and studied theoretically [86]. Moreover, researchers have also successfully demonstrated efficient parametric wavelength conversion [44, 84] and amplification [47] in the near/mid-IR regions using silicon nanophotonic wires. While research into this mid-IR wavelength region using silicon nanophotonic wires may not be directly related to the traditional telecommunication applications, it could open up a whole new field that has immediate impact in applications such as free-space communications, molecular spectroscopy, and environmental monitoring/sensing [87, 88].

Reference

1. S. Borkar, "Design challenges of technology scaling," IEEE Micro **19**, 23-29 (1999).
2. R. A. Soref and J. P. Lorenzo, "Single-crystal silicon - a new material for 1.3 and 1.6 um integrated optical components," Electronics Letters **21**, 953-954 (1985).

3. R. A. Soref and J. P. Lorenzo, "All-silicon active and passive guided-wave componets for l =1.3 and 1.6 mm," IEEE Journal of Quantum Electronics **22**, 873-879 (1986).

4. R. A. Soref, "Silicon-based optoelectronics," Proceedings of the IEEE **81**, 1687-1706 (1993).

5. Y. A. Vlasov and S. J. McNab, "Losses in single-mode silicon-on-insulator strip waveguides and bends," Optics Express **12**, 1622-1631 (2004).

6. H. S. Rong, Y. H. Kuo, A. S. Liu, M. Paniccia, and O. Cohen, "High efficiency wavelength conversion of 10Gb/s data in silicon waveguides," Optics Express **14**, 1182-1188 (2006).

7. J. J. Hu, N. N. Feng, N. Carlie, L. Petit, J. F. Wang, A. Agarwal, K. Richardson, and L. Kimerling, "Low-loss high-index-contrast planar waveguides with graded-index cladding layers," Optics Express **15**, 14566-14572 (2007).

8. J. Cardenas, C. B. Poitras, J. T. Robinson, K. Preston, L. Chen, and M. Lipson, "Low loss etchless silicon photonic waveguides," Optics Express **17**, 4752-4757 (2009).

9. S. K. Selvaraja, W. Bogaerts, P. Absil, D. V. Thourhout, and R. Baets, "Record low-loss hybrid rib/wire waveguides for silicon photonic circuits," in *Group IV Photonics*, Beijing, PR China, 2010

10. B. Jalali and S. Fathpour, "Silicon photonics," Journal of Lightwave Technology **24**, 4600-4615 (2006).

11. S. J. McNab, N. Moll, and Y. A. Vlasov, "Ultra-low loss photonic integrated circuit with membrane-type photonic crystal waveguides," Optics Express **11**, 2927-2939 (2003).

12. J. Van Campenhout, W. M. J. Green, S. Assefa, and Y. A. Vlasov, "Low-power, 2x2 silicon electro-optic switch with 110-nm bandwidth for broadband reconfigurable optical networks," Optics Express **17**, 24020-24029 (2009).

13. S. Assefa, C. Jahnes, and Y. Vlasov, "CMOS compatible integrated dielectric optical waveguide coupler and fabrication," US Patent US7738753B2 (2010).

14. V. R. Almeida, R. R. Panepucci, and M. Lipson, "Nanotaper for compact mode conversion," Optics Letters **28**, 1302-1304 (2003).

15. D. Taillaert, P. Bienstman, and R. Baets, "Compact efficient broadband grating coupler for silicon-on-insulator waveguides," Optics Letters **29**, 2749-2751 (2004).

16. G. Roelkens, D. Van Thourhout, and R. Baets, "High efficiency grating coupler between silicon-on-insulator waveguides and perfectly vertical optical fibers," Optics Letters **32**, 1495-1497 (2007).

17. P. Paddon and J. F. Young, "Simple approach to coupling in textured planar waveguides," Optics Letters **23**, 1529-1531 (1998).

18. F. N. Xia, L. Sekaric, and Y. Vlasov, "Ultracompact optical buffers on a silicon chip," Nature Photonics **1**, 65-71 (2007).

19. Y. Okawachi, M. A. Foster, J. E. Sharping, A. L. Gaeta, Q. F. Xu, and M. Lipson, "All-optical slow-light on a photonic chip," Optics Express **14**, 2317-2322 (2006).

20. Y. Okawachi, M. A. Foster, X. P. Chen, A. C. Turner-Foster, R. Salem, M. Lipson, C. Xu, and A. L. Gaeta, "Large tunable delays using parametric mixing and phase conjugation in Si nanowaveguides," Optics Express **16**, 10349-10357 (2008).

21. Y. T. Dai, X. P. Chen, Y. Okawachi, A. C. Turner-Foster, M. A. Foster, M. Lipson, A. L. Gaeta, and C. Xu, "1 mu s tunable delay using parametric mixing and optical phase conjugation in Si waveguides," Optics Express **17**, 7004-7010 (2009).

22. F. N. Xia, M. Rooks, L. Sekaric, and Y. Vlasov, "Ultra-compact high order ring resonator filters using submicron silicon photonic wires for on-chip optical interconnects," Optics Express **15**, 11934-11941 (2007).

23. L. J. Zhou and A. W. Poon, "Electrically reconfigurable silicon microring resonator-based filter with waveguide-coupled feedback," Optics Express **15**, 9194-9204 (2007).

24. S. Xiao, M. H. Khan, H. Shen, and M. Qi, "Multiple-channel silicon micro-resonator based filters for WDM applications," Optics Express **15**, 7489-7498 (2007).

25. F. Horst, W. M. J. Green, B. J. Offrein, and Y. A. Vlasov, "Silicon-on-Insulator Echelle Grating WDM Demultiplexers With Two Stigmatic Points," IEEE Photonics Technology Letters **21**, 1743-1745 (2009).

26. G. Roelkens, D. Van Thourhout, and R. Baets, "Silicon-on-insulator ultra-compact duplexer based on a diffractive grating structure," Optics Express **15**, 10091-10096 (2007).

27. W. Bogaerts, D. Taillaert, P. Dumon, D. Van Thourhout, and R. Baets, "A polarization-diversity wavelength duplexer circuit in silicon-on-insulator photonic wires," Optics Express **15**, 1567-1578 (2007).

28. D. W. Kim, A. Barkai, R. Jones, N. Elek, H. Nguyen, and A. S. Liu, "Silicon-on-insulator eight-channel optical mulltiplexer based on a cascade of asymmetric Mach-Zehnder interferometers," Optics Letters **33**, 530-532 (2008).

29. A. S. Liu, L. Liao, Y. Chetrit, J. Basak, H. Nguyen, D. Rubin, and M. Paniccia, "Wavelength Division Multiplexing Based Photonic Integrated Circuits on Silicon-on-Insulator Platform," IEEE Journal of Selected Topics in Quantum Electronics **16**, 23-32 (2010).
30. O. Boyraz and B. Jalali, "Demonstration of a silicon Raman laser," Optics Express **12**, 5269-5273 (2004).
31. H. S. Rong, R. Jones, A. S. Liu, O. Cohen, D. Hak, A. Fang, and M. Paniccia, "A continuous-wave Raman silicon laser," Nature **433**, 725-728 (2005).
32. H. S. Rong, A. S. Liu, R. Jones, O. Cohen, D. Hak, R. Nicolaescu, A. Fang, and M. Paniccia, "An all-silicon Raman laser," Nature **433**, 292-294 (2005).
33. O. Boyraz and B. Jalali, "Demonstration of directly modulated silicon Raman laser," Optics Express **13**, 796-800 (2005).
34. Q. F. Xu, B. Schmidt, S. Pradhan, and M. Lipson, "Micrometre-scale silicon electro-optic modulator," Nature **435**, 325-327 (2005).
35. W. M. J. Green, M. J. Rooks, L. Sekaric, and Y. A. Vlasov, "Ultra-compact, low RF power, 10 Gb/s silicon Mach-Zehnder modulator," Optics Express **15**, 17106-17113 (2007).
36. Q. F. Xu, S. Manipatruni, B. Schmidt, J. Shakya, and M. Lipson, "12.5 Gbit/s carrier-injection-based silicon micro-ring silicon modulators," Optics Express **15**, 430-436 (2007).
37. L. Liao, A. Liu, D. Rubin, J. Basak, Y. Chetrit, H. Nguyen, R. Cohen, N. Izhaky, and M. Paniccia, "40 Gbit/s silicon optical modulator for highspeed applications," Electronics Letters **43**, 1196-1197 (2007).

38. H. L. R. Lira, S. Manipatruni, and M. Lipson, "Broadband hitless silicon electro-optic switch for on-chip optical networks," Optics Express **17**, 22271-22280 (2009).

39. R. Salem, M. A. Foster, A. C. Turner, D. F. Geraghty, M. Lipson, and A. L. Gaeta, "All-optical regeneration on a silicon chip," Optics Express **15**, 7802-7809 (2007).

40. V. Raghunathan, R. Claps, D. Dimitropoulos, and B. Jalali, "Wavelength conversion in silicon using Raman induced four-wave mixing," Applied Physics Letters **85**, 34-36 (2004).

41. R. L. Espinola, J. I. Dadap, R. M. Osgood, S. J. McNab, and Y. A. Vlasov, "C-band wavelength conversion in silicon photonic wire waveguides," Optics Express **13**, 4341-4349 (2005).

42. Y. H. Kuo, H. S. Rong, V. Sih, S. B. Xu, M. Paniccia, and O. Cohen, "Demonstration of wavelength conversion at 40 Gb/s data rate in silicon waveguides," Optics Express **14**, 11721-11726 (2006).

43. B. G. Lee, A. Biberman, A. C. Turner-Foster, M. A. Foster, M. Lipson, A. L. Gaeta, and K. Bergman, "Demonstration of Broadband Wavelength Conversion at 40 Gb/s in Silicon Waveguides," IEEE Photonics Technology Letters **21**, 182-184 (2009).

44. S. Zlatanovic, J. S. Park, S. Moro, J. M. C. Boggio, I. B. Divliansky, N. Alic, S. Mookherjea, and S. Radic, "Mid-infrared wavelength conversion in silicon waveguides using ultracompact telecom-band-derived pump source," Nature Photonics **4**, 561-564 (2010).

45. M. A. Foster, A. C. Turner, J. E. Sharping, B. S. Schmidt, M. Lipson, and A. L. Gaeta, "Broad-band optical parametric gain on a silicon photonic chip," Nature **441**, 960-963 (2006).

46. M. A. Foster, A. C. Turner, R. Salem, M. Lipson, and A. L. Gaeta, "Broad-band continuous-wave parametric wavelength conversion in silicon nanowaveguides," Optics Express **15**, 12949-12958 (2007).

47. X. P. Liu, R. M. Osgood, Y. A. Vlasov, and W. M. J. Green, "Mid-infrared optical parametric amplifier using silicon nanophotonic waveguides," Nature Photonics **4**, 557-560 (2010).

48. L. Chen, K. Preston, S. Manipatruni, and M. Lipson, "Integrated GHz silicon photonic interconnect with micrometer-scale modulators and detectors," Optics Express **17**, 15248-15256 (2009).

49. S. Assefa, F. N. Xia, W. M. J. Green, C. L. Schow, A. V. Rylyakov, and Y. A. Vlasov, "CMOS-Integrated Optical Receivers for On-Chip Interconnects," IEEE Journal of Selected Topics in Quantum Electronics **16**, 1376-1385 (2010).

50. S. M. Sze, *Physics of Semiconductor Devices* (John Wiley and Sons, New York, 1981).

51. R. A. Soref and B. R. Bennett, "Electrooptical effects in silicon," IEEE Journal of Quantum Electronics **23**, 123-129 (1987).

52. N. Sherwood-Droz, H. Wang, L. Chen, B. G. Lee, A. Biberman, K. Bergman, and M. Lipson, "Optical 4x4 hitless silicon router for optical Networks-on-Chip (NoC)," Optics Express **16**, 15915-15922 (2008).

53. L. Chen, N. Sherwood-Droz, and M. Lipson, "Compact bandwidth-tunable microring resonators," Optics Letters **32**, 3361-3363 (2007).

54. J. Teng, P. Dumon, W. Bogaerts, H. B. Zhang, X. G. Jian, X. Y. Han, M. S. Zhao, G. Morthier, and R. Baets, "Athermal Silicon-on-insulator ring resonators by overlaying

a polymer cladding on narrowed waveguides," Optics Express **17**, 14627-14633 (2009).

55. T. Chu, H. Yamada, S. Ishida, and Y. Arakawa, "Compact 1 x N thermo-optic switches based on silicon photonic wire waveguides," Optics Express **13**, 10109-10114 (2005).

56. W. Bogaerts, R. Baets, P. Dumon, V. Wiaux, S. Beckx, D. Taillaert, B. Luyssaert, J. Van Campenhout, P. Bienstman, and D. Van Thourhout, "Nanophotonic waveguides in silicon-on-insulator fabricated with CMOS technology," Journal of Lightwave Technology **23**, 401-412 (2005).

57. A. Barkai, Y. Chetrit, O. Cohen, R. Cohen, N. Elek, E. Ginsburg, S. Litski, A. Michaeli, O. Raday, D. Rubin, G. Sarid, N. Izhaky, M. Morse, O. Dosunmu, A. H. Liu, L. Liao, H. H. Rong, Y. H. Kuo, S. B. Xu, D. Alduino, J. Tseng, H. F. Liu, and M. Paniccia, "Integrated silicon photonics for optical networks Invited," Journal of Optical Networking **6**, 25-47 (2007).

58. D. K. Sparacin, S. J. Spector, and L. C. Kimerling, "Silicon waveguide sidewall smoothing by wet chemical oxidation," Journal of Lightwave Technology **23**, 2455-2461 (2005).

59. J. van Campenhout, W. M. J. Green, X. P. Liu, S. Assefa, R. M. Osgood, and Y. A. Vlasov, "Silicon-nitride surface passivation of submicrometer silicon waveguides for low-power optical switches," Optics Letters **34**, 1534-1536 (2009).

60. B. G. Lee, X. G. Chen, A. Biberman, X. P. Liu, I. W. Hsieh, C. Y. Chou, J. I. Dadap, F. N. Xia, W. M. J. Green, L. Sekaric, Y. A. Vlasov, R. M. Osgood, and K. Bergman,

"Ultrahigh-bandwidth silicon photonic nanowire waveguides for on-chip networks," IEEE Photonics Technology Letters **20**, 398-400 (2008).

61. V. R. Almeida, Q. F. Xu, C. A. Barrios, and M. Lipson, "Guiding and confining light in void nanostructure," Optics Letters **29**, 1209-1211 (2004).
62. Q. F. Xu, V. R. Almeida, R. R. Panepucci, and M. Lipson, "Experimental demonstration of guiding and confining light in nanometer-size low-refractive-index material," Optics Letters **29**, 1626-1628 (2004).
63. C. A. Barrios and M. Lipson, "Electrically driven silicon resonant light emitting device based on slot- waveguide," Optics Express **13**, 10092-10101 (2005).
64. C. Koos, P. Vorreau, T. Vallaitis, P. Dumon, W. Bogaerts, R. Baets, B. Esembeson, I. Biaggio, T. Michinobu, F. Diederich, W. Freude, and J. Leuthold, "All-optical high-speed signal processing with silicon-organic hybrid slot waveguidesx," Nature Photonics **3**, 216-219 (2009).
65. M. Dinu, F. Quochi, and H. Garcia, "Third-order nonlinearities in silicon at telecom wavelengths," Applied Physics Letters **82**, 2954-2956 (2003).
66. A. D. Bristow, N. Rotenberg, and H. M. van Driel, "Two-photon absorption and Kerr coefficients of silicon for 850-2200 nm," Applied Physics Letters **90**, 191104-191106 (2007).
67. H. K. Tsang, C. S. Wong, T. K. Liang, I. E. Day, S. W. Roberts, A. Harpin, J. Drake, and M. Asghari, "Optical dispersion, two-photon absorption and self-phase modulation in silicon waveguides at 1.5 mu m wavelength," Applied Physics Letters **80**, 416-418 (2002).

68. E. Dulkeith, Y. A. Vlasov, X. G. Chen, N. C. Panoiu, and R. M. Osgood, "Self-phase-modulation in submicron silicon-on-insulator photonic wires," Optics Express **14**, 5524-5534 (2006).

69. I. W. Hsieh, X. G. Chen, J. I. Dadap, N. C. Panoiu, R. M. Osgood, S. J. McNab, and Y. A. Vlasov, "Cross-phase modulation-induced spectral and temporal effects on co-propagating femtosecond pulses in silicon photonic wires," Optics Express **15**, 1135-1146 (2007).

70. L. H. Yin, Q. Lin, and G. P. Agrawal, "Dispersion tailoring and soliton propagation in silicon waveguides," Optics Letters **31**, 1295-1297 (2006).

71. J. D. Zhang, Q. Lin, G. Piredda, R. W. Boyd, G. P. Agrawal, and P. M. Fauchet, "Optical solitons in a silicon waveguide," Optics Express **15**, 7682-7688 (2007).

72. I. W. Hsieh, X. G. Chen, X. P. Liu, J. I. Dadap, N. C. Panoiu, C. Y. Chou, F. N. Xia, W. M. Green, Y. A. Vlasov, and R. M. Osgood, "Supercontinuum generation in silicon photonic wires," Optics Express **15**, 15242-15249 (2007).

73. L. H. Yin, Q. Lin, and G. P. Agrawal, "Soliton fission and supercontinuum generation in silicon waveguides," Optics Letters **32**, 391-393 (2007).

74. T. K. Liang, L. R. Nunes, T. Sakamoto, K. Sasagawa, T. Kawanishi, M. Tsuchiya, G. R. A. Priem, D. Van Thourhout, P. Dumon, R. Baets, and H. K. Tsang, "Ultrafast all-optical switching by cross-absorption modulation in silicon wire waveguides," Optics Express **13**, 7298-7303 (2005).

75. Y. Vlasov, W. M. J. Green, and F. Xia, "High-throughput silicon nanophotonic wavelength-insensitive switch for on-chip optical networks," Nature Photonics **2**, 242-246 (2008).

76. B. G. Lee, A. Biberman, P. Dong, M. Lipson, and K. Bergman, "All-optical comb switch for multiwavelength message routing in silicon photonic networks," IEEE Photonics Technology Letters **20**, 767-769 (2008).

77. W. Astar, J. B. Driscoll, X. P. Liu, J. I. Dadap, W. M. J. Green, Y. A. Vlasov, G. M. Carter, and R. M. Osgood, "Conversion of 10 Gb/s NRZ-OOK to RZ-OOK utilizing XPM in a Si nanowire," Optics Express **17**, 12987-12999 (2009).

78. W. Astar, J. B. Driscoll, X. P. Liu, J. I. Dadap, W. M. J. Green, Y. A. Vlasov, G. M. Carter, and R. M. Osgood, "All-Optical Format Conversion of NRZ-OOK to RZ-OOK in a Silicon Nanowire Utilizing Either XPM or FWM and Resulting in a Receiver Sensitivity Gain of similar to 2.5 dB," IEEE Journal of Selected Topics in Quantum Electronics **16**, 234-249 (2010).

79. W. Astar, J. B. Driscoll, X. P. Liu, J. I. Dadap, W. M. J. Green, Y. A. Vlasov, G. M. Carter, and R. M. Osgood, "Tunable Wavelength Conversion by XPM in a Silicon Nanowire, and the Potential for XPM-Multicasting," Journal of Lightwave Technology **28**, 2499-2511 (2010).

80. J. B. Driscoll, W. Astar, X. Liu, J. I. Dadap, W. M. J. Green, Y. A. Vlasov, G. M. Carter, and R. M. Osgood, "All-Optical Wavelength Conversion of 10 Gb/s RZ-OOK Data in a Silicon Nanowire via Cross-Phase Modulation: Experiment and Theoretical Investigation," IEEE Journal of Selected Topics in Quantum Electronics **16**, 1448-1459 (2010).

81. G. P. Agrawal, *Nonlinear Fiber Optics* (Academic, San Diego, 2001).

82. A. C. Turner, C. Manolatou, B. S. Schmidt, M. Lipson, M. A. Foster, J. E. Sharping, and A. L. Gaeta, "Tailored anomalous group-velocity dispersion in silicon channel waveguides," Optics Express **14**, 4357-4362 (2006).

83. X. P. Liu, W. M. J. Green, X. G. Chen, I. W. Hsieh, J. I. Dadap, Y. A. Vlasov, and R. M. Osgood, "Conformal dielectric overlayers for engineering dispersion and effective nonlinearity of silicon nanophotonic wires," Optics Letters **33**, 2889-2891 (2008).

84. A. C. Turner-Foster, M. A. Foster, R. Salem, A. L. Gaeta, and M. Lipson, "Frequency conversion over two-thirds of an octave in silicon nanowaveguides," Optics Express **18**, 1904-1908 (2010).

85. V. Raghunathan, D. Borlaug, R. R. Rice, and B. Jalali, "Demonstration of a mid-infrared silicon Raman amplifier," Optics Express **15**, 14355-14362 (2007).

86. Q. Lin, T. J. Johnson, R. Perahia, C. P. Michael, and O. J. Painter, "A proposal for highly tunable optical parametric oscillation in silicon micro-resonators," Optics Express **16**, 10596-10610 (2008).

87. M. Ebrahim-Zadeh and I. T. Sorokina, *Mid-Infrared Coherent Sources and Applications* (Springer, Dordreht, 2007).

88. R. A. Soref, S. J. Emelett, and A. R. Buchwald, "Silicon waveguided components for the long-wave infrared region," Journal of Optics a-Pure and Applied Optics **8**, 840-848 (2006).

Chapter 2

Simulation, modeling and experimental techniques

2.1 Calculation of waveguide modes and dispersion properties

Unlike wave-propagation in free space, electromagnetic waves possess certain spatial distributions in a guided medium. These spatial distributions are called waveguide optical modes, which are the eigenfunctions of Maxwell's equations satisfying boundary conditions at all interfaces in the waveguide. The optical modes usually are mostly confined to a region, which has the highest index of refraction in the waveguide structure, although they also extend to low index region because of the boundary conditions. Such modal overlap with different index regions gives rise to effective indices of the optical modes, which have values between the lowest index and highest index in the waveguide structures. A more detailed theoretical discussion of optical modes in dielectric waveguides can be found in Ref [1-3].

Analytic solutions for optical modes only exist in simple guiding structures such as 2-dimensional slab dielectric waveguides and step-index optical fibers. For more complicated guiding structures such as 3-dimensional waveguides, which is the case for the silicon nanophotonic wires studied in this thesis, numerical techniques are usually needed to solve Maxwell equations and to find approximate but relatively accurate optical modes. Several such numerical techniques exist [4, 5], e.g. beam propagation method (BPM) [6-8], finite difference method (FDM) [9, 10], and finite element method (FEM) [5, 9, 11]. BPM is usually used to model low-index-contrast waveguides, while

FDM and FEM have no such limitation. FEM is known to be the most powerful technique and generally gives the most accurate solutions for optical modes. For this thesis, a commercial full-vectorial FEM mode-solver package *FemSIM* implemented by *Rsoft Design Group* [12] is used to solve the optical modes supported by silicon nanophotonic wires.

This thesis concerns the physical properties of silicon nanophotonic wires from the infrared to mid-IR region. Thus in simulations wavelength sweeping from 1.2 μm to 3.0 μm is typical. The material dispersion (wavelength dependent material index of refraction) in this wavelength region is incorporated via the Sellmeier equations for Si [13],

$$n_{\mathrm{Si}}^2 = 11.6858 + 0.939816 \big/ \lambda^2 + 8.10461\times10^{-3}\times1.1071^2 \big/ (\lambda^2 - 1.1071^2), \qquad (2.1.1)$$

for SiO_2 [14],

$$n_{\mathrm{SiO_2}}^2 = 1.300 + 0.81996\lambda^2 \big/ (\lambda^2 - 0.10396^2) - 0.01082\lambda^2, \qquad (2.1.2)$$

for Si_3N_4 [15, 16],

$$n_{\mathrm{Si_3N_4}}^2 = 1 + 2.8939\lambda^2 \big/ (\lambda^2 - 0.13967^2), \qquad (2.1.3)$$

where λ is the free-space wavelength in micrometers in the above three equations. Waveguide modes in silicon nanophotonic wires can be classified into two categories namely quasi-TE and quasi-TM modes. Figure 2-1 shows the calculated contour plots of transverse electric field components for fundamental quasi-TE and quasi-TM modes at a wavelength of 1.55 μm in a 600 nm × 220 nm ($w \times h$) silicon nanophotonic wire. The fundamental quasi-TE modes have this major electric field distribution E_x parallel to the silicon/BOX interface and a minor electric field distribution E_y perpendicular to that interface, while the quasi-TM modes correspond to the opposite case.

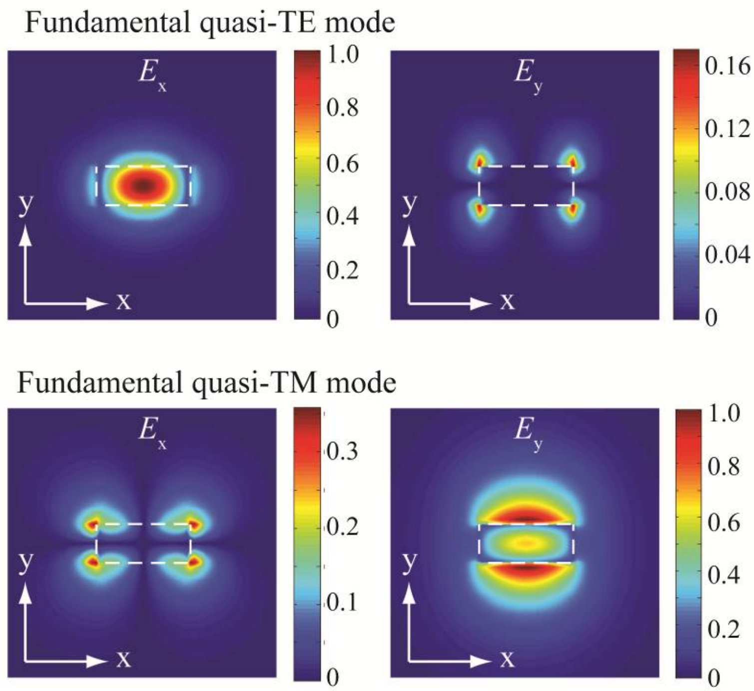

Figure 2-1 Contour plots of transverse electric field components for fundamental quasi-TE and quasi-TM modes of a $w \times h$ = 600 nm × 220 nm silicon waveguide. The dotted lines illustrate the boundary of the silicon nanophotonic wire. Colorbar represents the normalized field amplitude.

Guided optical modes in waveguides exhibit dispersion, which is determined by the interplay of material's intrinsic dispersion and geometric contribution due to the optical confinement. The amount of dispersion in the waveguide is typically characterized by the group velocity dispersion (GVD) parameter D_λ, which describes the slope of inverse group velocity v_g versus wavelength λ and is related with the wavelength-dependent modal effective index n_{eff} by

$$D_{\lambda} = \frac{d}{d\lambda}\left(\frac{1}{v_g}\right) = -\frac{\lambda}{c}\frac{d^2 n_{eff}}{d\lambda^2} \tag{2.1.4}$$

where c is the speed of light in vacuum [17]. Numerically, the raw wavelength-dependent modal effective index data (usually by advancing in 2 nm wavelength steps) are first fitted with a 9th polynomial in order to smooth out the small numerical discontinuities introduced by the mode-solver and then differentiated twice according to Eq. (2.1.4) to obtain the GVD dispersion. It is also convenient to characterize the waveguide dispersion using the dispersion term β_n,

$$\beta_n = \frac{d^n \beta_0}{d\omega^n} \tag{2.1.5}$$

where β_0 is the propagation constant and is related to n_{eff} according to $\beta_0 = 2\pi n_{eff} / \lambda$. A similar numerical approach is used to calculate β_n based on the raw effective index data.

2.2 Simulation of pulse dynamics

Significant efforts have been devoted to understand the properties of picoseconds and subpicosecond pulse dynamics in the silicon nanophotonic wires. Several theoretical models have been developed to account for the ultrafast pulse dynamics by a number of groups in the past decade [18-23]. Despite the subtle differences, all of these models show great similarities in dealing with various nonlinear effects. The model used in this thesis is adopted from the model developed by the Osgood group at Columbia University. A comprehensive description of the original model can be found in Ref [18, 23].

2.2.1 Pulse dynamics for a single optical pulse

The dynamics of an optical pulse propagating in a silicon nanophotonic wire is governed by a perturbed nonlinear Schrödinger equation (NLSE):

$$
\begin{aligned}
i\frac{\partial u}{\partial z}+\sum_{n\geq 1}\frac{i^n\beta_n}{n!}\frac{\partial^n u}{\partial t^n} &= -\frac{ic\kappa}{2n_{si}v_g}\left(\alpha_{\ln}+\alpha_{FC}\right)u-\frac{\omega\kappa}{n_{si}v_g}\delta n_{FC}u \\
&\quad -\frac{3\omega P\Gamma}{4\varepsilon_0 A_0 v_g^2}\left(1+i\tau_s\frac{\partial}{\partial t}\right)|u|^2 u.
\end{aligned}
\tag{2.2.1}
$$

Note in this thesis the temporal width of optical pulses under investigation is on the order of picoseconds or less. Thus in the above model, Raman scattering is neglected since an interaction time on the order of 10 picoseconds is necessary for Raman scattering to become significant [24]. In Eq. (2.2.1), z (t) is the distance (time), u is the normalized pulse envelop, ω is the angular frequency, β_n is the n$^{\text{th}}$ order dispersion term, P is the peak power, n_{si} is bulk silicon's index of refraction, $\alpha_{\ln}$ is the linear propagation loss, α_{FC} (δ_{FC}) is the free carrier (FC) loss (FC-induced refractive index change), and $A_0 = wh$ is the geometrical area of the silicon core. Based on a Drude model, δ_{FC} and α_{FC} are given by [25]

$$
\begin{aligned}
\delta n_{FC} &= -\frac{e^2 N}{2\varepsilon_0 n\omega^2}\left(\frac{N}{m_{ce}^*}+\frac{N^{0.8}}{m_{ch}^*}\right) \\
\alpha_{FC} &= \frac{e^3 N}{\varepsilon_0 c n\omega^2}\left(\frac{1}{\mu_e m_{ce}^{*\,2}}+\frac{1}{\mu_h m_{ch}^{*\,2}}\right)
\end{aligned}
\tag{2.2.2}
$$

where N is the FC density, $m_{ce}^* = 0.26m_0$ ($m_{ch}^* = 0.39m_0$) is the effective mass of electrons (holes), with m_0 the mass of the electron, and u_e (u_h) is the electron (hole) mobility. κ is the power confinement factor defined as

$$\kappa = \frac{n_{si}^2 \int_{A_0} |e|^2 \, dA}{\int n^2(r_t) |e|^2 \, dA} \tag{2.2.3}$$

where $n(r_t)$ is the index distribution in the transverse plane, and $e \equiv e(\omega; r_t)$ are the waveguide modes. Also, Γ is waveguide effective third-order nonlinearity defined as

$$\Gamma = \frac{A_0 \int e^* \cdot \hat{\chi}^{(3)} \vdots e e^* e dA}{\left(\int n^2(r_t) |e|^2 \, dA \right)^2} \tag{2.2.4}$$

where $\hat{\chi}^{(3)}$ is the third order susceptibility of silicon. Note that $\hat{\chi}^{(3)}$ for silicon has two independent components, $\hat{\chi}_{1111}^{(3)}$ and $\hat{\chi}_{1122}^{(3)}$; however, a recent experiment has shown that $\hat{\chi}_{1111}^{(3)}$ = 2.36 $\hat{\chi}_{1122}^{(3)}$ within a broad frequency range [26]. The remaining component is determined from the experimentally measured values of Kerr coefficient, n_2 and the two-photon absorption (TPA) coefficient, β_{TPA} , by using $n_2 = 3\hat{\chi}_{eff}^{'(3)} / 4\varepsilon_0 c n_{si}^2$ and $\beta_{TPA} = 3\omega \hat{\chi}_{eff}^{''(3)} / 2\varepsilon_0 c^2 n_{si}^2$. For silicon nanophotonic wires fabricated along the $[1\bar{1}0]$ direction $\hat{\chi}_{eff}^{''(3)} = (\hat{\chi}_{1111}^{(3)} + 3\hat{\chi}_{1122}^{(3)})/2$ [24]. Furthermore, the last term in Eq. (2.2.1) describes the self-steepening of the pulse and the formation of optical shock, a nonlinear effect characterized by the shock time [17, 27]. The shock time is defined as $\tau_s = \partial \ln(\gamma) / \partial \omega = \tau_0 + \tau_{wm}$, where $\gamma = 3\omega\Gamma / 4\varepsilon_0 A_0 v_g^2$ is the waveguide complex effective nonlinear parameter, $\tau_0 = 1/\omega$ is related to the noninstantaneous response of the nonlinearity in a bulk material, and $\tau_{wm} = \partial \ln(\Gamma / v_g^2) / \partial \omega$ gives the waveguide contribution including that due to dispersions in $\chi^{(3)}$. Finally, the FC dynamics are determined by [24]

$$\frac{\partial N}{\partial t} = -\frac{N}{t_c} + \frac{3P^2\Gamma''}{4\varepsilon_0 \hbar A_0^2 v_g^2}|u|^4 \qquad (2.2.5)$$

where t_c is free carrier lifetime in the silicon nanophotonic wire, and Γ'' is the imaginary part of the Γ.

2.2.2 Pulse dynamics for multiple optical pulses

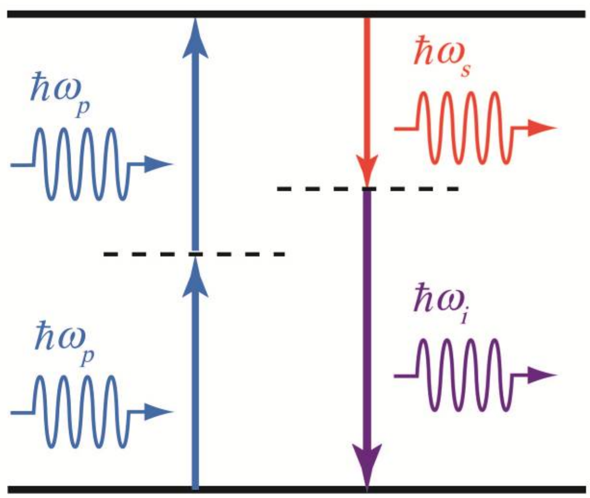

Figure 2-2 Energy diagram for a degenerate FWM process, where two pump photons are annihilated to create a signal and idler photon.

When two optical pulses with different carrier frequencies are mixed and co-propagating inside the silicon nanophotonic wires, coupled nonlinear Schrödinger equations are needed to characterize the added nonlinear interactions between these two pulses. Typical only two NLSEs, one for each optical pulse, are sufficient. However, as shown in Figure 2-2, a degenerate FWM process [17], which involves the annihilation of two pump photons to create a signal and idler photon ($2\hbar\omega_p = \hbar\omega_s + \hbar\omega_i$), could also happen. If this FWM process is efficient under certain conditions, a third NLSE is necessary in order to account for the pulse dynamics of the parametrically generated idler wave.

Considering a case of a strong pump pulse mixing with a weak probe signal ($P_p \gg P_s$) and assuming they have same polarization, the set of coupled NLSEs could be expressed in terms of the pump, signal, and idler,

$$
\begin{aligned}
i\frac{\partial u_p}{\partial z}+\sum_{n\geq 1}\frac{i^n\beta_n^p}{n!}\frac{\partial^n u_p}{\partial t^n} &= -\frac{ic\kappa_p}{2n_{si}v_g^p}\left(\alpha_{\ln}^p+\alpha_{FC}^p\right)u_p-\frac{\omega_p\kappa_p}{nv_g^p}\delta n_{FC}^p u_p \\
&\quad -\frac{3\omega_p P_p\Gamma_p}{4\varepsilon_0 A_0 v_g^{p2}}\left|u_p\right|^2 u_p,
\end{aligned}
\tag{2.2.6}
$$

$$
\begin{aligned}
i\frac{\partial u_s}{\partial z}+\sum_{n\geq 1}\frac{i^n\beta_n^s}{n!}\frac{\partial^n u_s}{\partial t^n} &= -\frac{ic\kappa_s}{2n_{si}v_s^p}\left(\alpha_{\ln}^s+\alpha_{FC}^s\right)u_s-\frac{\omega_s\kappa_s}{nv_s^p}\delta n_{FC}^s u_s \\
&\quad -\frac{3\omega_s}{4\varepsilon_0 A_0 v_g^s}\left(2\frac{\Gamma_{sp}P_p}{v_g^p}\right)\left|u_p\right|^2 u_s-\frac{3\omega_i}{4\varepsilon_0 A_0 v_g^i}\frac{\Gamma_{spip}P_p}{v_g^p}u_p^2 u_i^* e^{i\Delta k_l z},
\end{aligned}
\tag{2.2.7}
$$

$$
\begin{aligned}
i\frac{\partial u_i}{\partial z}+\sum_{n\geq 1}\frac{i^n\beta_n^i}{n!}\frac{\partial^n u_i}{\partial t^n} &= -\frac{ic\kappa_i}{2n_{si}v_i^p}\left(\alpha_{\ln}^i+\alpha_{FC}^i\right)u_i-\frac{\omega_i\kappa_i}{nv_s^p}\delta n_{FC}^i u_i \\
&\quad -\frac{3\omega_i}{4\varepsilon_0 A_0 v_g^i}\left(2\frac{\Gamma_{ip}P_p}{v_g^p}\right)\left|u_p\right|^2 u_i-\frac{3\omega_s}{4\varepsilon_0 A_0 v_g^s}\frac{\Gamma_{ipsp}P_p}{v_g^p}u_p^2 u_s^* e^{i\Delta k_l z}.
\end{aligned}
\tag{2.2.8}
$$

Note that the above model treats the pulse dynamics for pulses with picosecond temporal width such that the self-steepening effect can be neglected [17]. u_j, ω_j, β_n^j, P, $\alpha_{\ln}^j$, α_{FC}^j, δn_{FC}^j, κ_j, and v_g^j in the above three equations have the same definition as in Section 2.2.1 for $j = p,s,i$ corresponding to pump, signal and idler respectively. $\Delta k_l = 2\beta_0^p - 2\beta_0^s - 2\beta_0^i$ describes the linear phase mismatch between pump, signal and idler waves. In order to have an efficient FWM parametric process, this linear phase mismatch needs to be balanced by a nonlinear phase-shift induced by the strong pump to create a near zero net phase mismatch [17], i.e. $2\gamma_p P_p - \Delta k_l \approx 0$, where γ_p is the waveguide effective nonlinearity parameter at the pump wavelength and is related to Γ_p by $\gamma_p = 3\omega_p P_p \Gamma_p / \left(4\varepsilon_0 A_0 v_g^{p2}\right)$. Γ_{jl} and Γ_{jlmn} $(j,l,m,n = p,s,i)$ are the nondegenerate effective third order nonlinearity defined by

$$\Gamma_{jl} = \Gamma_{jllj},$$
$$\Gamma_{jlmn} = \frac{A_0 \int_{A_0} e_j^* \cdot \overset{\wedge}{\chi}^{(3)} \left(-\omega_j; \omega_l, -\omega_m, \omega_n\right) \vdots e_l e_m^* e_n}{\varsigma_j \varsigma_l \varsigma_m \varsigma_n} \tag{2.2.9}$$

where $e_j \equiv e\left(\omega_j; r_t\right)$, $\varsigma_j = \left(\int n^2(r_t)\left|e_j\right|^2 dA\right)^{1/2}$, and $\overset{\wedge}{\chi}^{(3)}\left(-\omega_j; \omega_l, -\omega_m, \omega_n\right)$ is the bulk silicon's nondegenerated third order susceptibility. An accurate description of XPM, TPA and FWM requires complete information about $\overset{\wedge}{\chi}^{(3)}\left(-\omega_j; \omega_l, -\omega_m, \omega_n\right)$. However, only the degenerated $\overset{\wedge}{\chi}^{(3)}\left(-\omega_j; \omega_j, -\omega_j, \omega_j\right)$ for silicon is available based on the current experiment knowledge [28, 29]. In the simulation, $\overset{\wedge}{\chi}^{(3)}\left(-\omega_j; \omega_l, -\omega_m, \omega_n\right)$ is approximated by $\overset{\wedge}{\chi}^{(3)}\left(-\overline{\omega}; \overline{\omega}, -\overline{\omega}, \overline{\omega}\right)$, where $\overline{\omega} = (\omega_j + \omega_l + \omega_m + \omega_n)/4$ is the average angular frequency. The FC dynamics are governed by the pump pulse under the assumption $P_p \gg P_s$,

$$\frac{\partial N}{\partial t} = -\frac{N}{\tau_c} + \frac{6}{4\varepsilon_0 \hbar A_0^2}\left(\frac{\Gamma_p''}{2 v_g^{p2}}\left|u_p\right|^4\right) \tag{2.2.10}$$

where u_p is the normalized pulse envelope for pump, v_g^p is the group velocity of pump, Γ_p'' is the imaginary part of pump's effective third order nonlinearity Γ_p and other parameters have the same definition as in Section 2.2.1. α_{FC}^{j} and δn_{FC}^{j} are defined using Eq. (2.2.2) where ω is replaced with ω_j for $j = p, s, i$.

The above model soon becomes cumbersome if cascaded FWM processes are possible, since the corresponding number of NLSEs has to be added in order to take care of the cascading FWM products. In this case, a less rigorous but more efficient approach can be used to describe the pulse dynamics. Instead of having one NLSE for each optical pulse (launched or parametrically generated), the sum of all the input optical envelopes can be treated as a whole input envelope [30], e.g.

$$u = u_p e^{-j\omega_p t} + u_s e^{-j\omega_s t} = u_p (1 + \frac{u_s}{u_p} e^{-j(\omega_s - \omega_p)t}) e^{-j\omega_p t}. \qquad (2.2.11)$$

This sum launch envelope can then be inserted into the model described in Section 2.2.1 to characterize the pulse dynamics. In this way, all the possible nonlinear interactions will be treated naturally by using one NSLE.

To solve NSLE, the linear part of the NSLE is solved in the Fourier domain using symmetrized split-step Fourier transformation, whereas the nonlinear part is integrated in the temporal domain with a 4th-order Runge–Kutta algorithm [31]. The carrier density is obtained by solving the carrier dynamics equation with a 4th-order Runge–Kutta algorithm before the pulse advances to a next spatial step. In case of solving the coupled NLSEs as described in Section 2.2.2, the pump pulse advances to the next spatial step first followed by signal and idler pulses. Numerical convergence is studied before a final temporal step size and a final spatial step size is settled.

2.3 Experimental techniques

2.3.1 Fabrication of silicon waveguides

Our silicon nanophotonic wires are fabricated at the IBM Microelectronics Research Laboratory using 200 mm silicon-on-insulator (SOI) wafers from SOITEC. SOI wafers with 2 μm thick buried oxide (BOX) layer are primarily used for applications in the telecommunication bands. However, for mid-IR applications, SOI wafers with 3 μm thick BOX are used. The typical silicon-layer thickness is 220 nm and if needed this silicon layer is thickened by epitaxial growth of undoped single-crystal silicon [32]. A 100 nm-thick SiO_2 hardmask is deposited on the silicon layer by LPCVD. Nanophotonic waveguide patterns of variable width are exposed into a layer of resist by dose-striping (varying exposure time), using 248 nm deep-UV lithography. The patterns are then transferred into the SiO_2 hardmask by RIE. After stripping the resist, the waveguides are etched into the SOI layer using a HBr-based RIE chemistry. A thick SiO_2 layer is deposited on the formed silicon waveguides if necessary.

2.3.2 Study of optical transmission characteristics

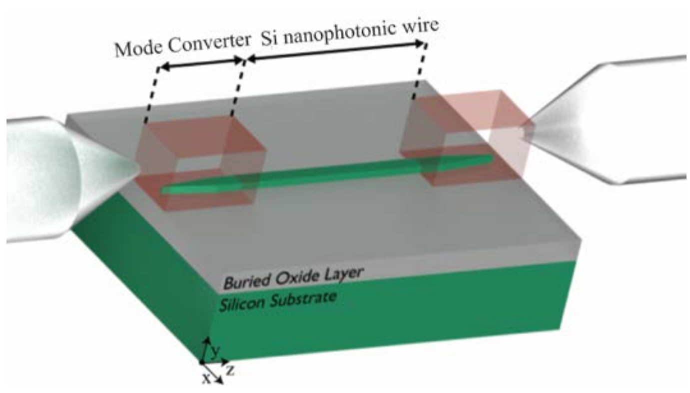

Figure 2-3 Light coupling schematic for silicon nanophotonic wires. Lensed tapered fibers are used for coupling light between fibers and mode converters.

Power-dependent transmission characteristics of an optical wave or mixed optical waves through silicon nanophotonic wires are studied experimentally. Optical inputs are either from connectorized laser/amplifier systems or fiber coupled from the free-space outputs of solid-state lasers. In some experiments, these optical inputs are modulated to carry data with an on-off-keying (OOK) format using a high-speed pulse-pattern generator (PPG) [33, 34]. The polarization of each optical input is individually controlled by an in-line fiber polarization controller by twisting and/or applying pressure to the build-in fiber section. These optical inputs are then multiplexed together using regular telecom fused single-mode fiber directional couplers. The optical coupling between an input fiber to a silicon waveguide is via edge coupling with a lensed tapered fiber and a mode converter as shown in Figure 2-3. The lensed tapered fiber used in the experiments is manufactured by OZ Optics and it has a spot size of 2.5 μm and a working distance of 14 μm at λ = 1.55 μm. The input and output lensed tapered fibers are mounted on high-accuracy piezo-driven XYZ translational stages for precise alignment with mode converters. The mode converter consists of a section of silicon inverse taper with a length ~ 250 μm and a low-index waveguide region which clads the silicon inverse taper. It couples optical power efficiently between the low-index waveguide section and the silicon nanophotonic wire. The low-index waveguide is designed to be mode-matched to the lensed tapered fibers for the best coupling. It has a typical length of several mm and is patterned with SU8 polymer [35] or SiO_xN_y [36] which is particularly useful for a CMOS compatible process. The transmitted optical power through silicon nanophotonic wire is collected by a second lensed tapered fiber, and is then directed to a telecom optical spectrum analyzer (OSA) for integrated power and spectral analysis or to a bit error rate testing (BERT) system for bit error rate (BER) measurement if optical outputs carry data.

When shifting the wavelength operation from telecommunication to mid-IR, there are several modifications made to the test system described above. First of all, the total length of single-mode fiber used in the system is largely reduced to avoid the increasing propagation loss in the fiber. For example, while the propagation loss in a single-mode fiber at $\lambda = 1550$ nm is less than 0.2 dB/km, it could be as large as 1 dB/m at $\lambda = 2200$ nm and increase to 3dB/m at $\lambda = 2500$ nm. Secondly, the coupling ratio for the telecom fused single-mode-fiber directional couplers is recalibrated for multiplexing mid-IR waves. Thirdly, the polymer-based mode-converters are discarded because of the polymer's strong absorption loss in mid-IR region. Instead, a SiO_xN_y-based mode converter specifically designed for coupling mid-IR light or a cleaved facet through the silicon nanophotonic wires is used. Finally, the power and spectral information of transmitted light is analyzed on a mid-IR OSA (Yokogawa AQ6375) that is sensitive up-to $\lambda = 2500$ nm.

Reference

1. A. W. Snyder and J. Love, *Optical Waveguide Theory* (Kluwer Academic Publishers, Norwell, 1983).
2. D. Marcuse, *Theory of Dielectric Opitcal Waveguides (2nd Edition)* (Academic Press, Inc., Boston, 1991).
3. A. Yariv, *Optical Electronics in Modern Communications (5th Edition)* (Oxford University Press, New York, 1997).

4. R. Scarmozzino, A. Gopinath, R. Pregla, and S. Helfert, "Numerical techniques for modeling guided-wave photonic devices," IEEE Journal of Selected Topics in Quantum Electronics **6**, 150-162 (2000).

5. D. Yevick, "A guide to electric-field propagation techniques for guided-wave optics," Optical and Quantum Electronics **26**, S185-S197 (1994).

6. P. E. Lagasse and R. Baets, "Application of propagating beam methods to electromagnetic and acoustic-wave propagation problems - a review," Radio Science **22**, 1225-1233 (1987).

7. R. Clauberg and P. Vonallmen, "Vectorial beam-propagation method for integrated-optics," Electronics Letters **27**, 654-655 (1991).

8. C. L. Xu, W. P. Huang, and S. K. Chaudhuri, "Efficient and accurate vector mode calculations by beam-propagation method," Journal of Lightwave Technology **11**, 1209-1215 (1993).

9. T. B. Koch, J. B. Davies, and D. Wickramasinghe, "Finite-element finite-difference propagation algorithm for integrated optical-device," Electronics Letters **25**, 514-516 (1989).

10. R. Accornero, M. Artiglia, G. Coppa, P. Divita, G. Lapenta, M. Potenza, and P. Ravetto, "Finite-difference methods for the analysis of integrated optical wave-guides," Electronics Letters **26**, 1959-1960 (1990).

11. S. Selleri, L. Vincetti, A. Cucinotta, and M. Zoboli, "Complex FEM modal solver of optical waveguides with PML boundary conditions," Optical and Quantum Electronics **33**, 359-371 (2001).

12. Available: http://www.rsoftdesign.com.

13. E. D. Palik, *Handbook of Optical Constants of Solid* (Academic, San Diego, 1998).

14. C. M. Herzinger, B. Johs, W. A. McGahan, J. A. Woollam, and W. Paulson, "Ellipsometric determination of optical constants for silicon and thermally grown silicon dioxide via a multi-sample, multi-wavelength, multi-angle investigation," Journal of Applied Physics **83**, 3323-3336 (1998).

15. H. R. Philipp, "Optical properties of silicon-nitride," Journal of the Electrochemical Society **120**, 295-300 (1973).

16. T. Baak, "Silicon oxynitride - a material for GRIN optics," Applied Optics **21**, 1069-1072 (1982).

17. G. P. Agrawal, *Nonlinear Fiber Optics* (Academic, San Diego, 2001).

18. J. I. Dadap, N. C. Panoiu, X. G. Chen, I. W. Hsieh, X. P. Liu, C. Y. Chou, E. Dulkeith, S. J. McNab, F. N. Xia, W. M. J. Green, L. Sekaric, Y. A. Vlasov, and R. M. Osgood, "Nonlinear-optical phase modification in dispersion-engineered Si photonic wires," Optics Express **16**, 1280-1299 (2008).

19. Q. Lin, O. J. Painter, and G. P. Agrawal, "Nonlinear optical phenomena in silicon waveguides: Modeling and applications," Optics Express **15**, 16604-16644 (2007).

20. I. D. Rukhlenko, M. Premaratne, and G. P. Agrawal, "Nonlinear Silicon Photonics: Analytical Tools," IEEE Journal of Selected Topics in Quantum Electronics **16**, 200-215 (2010).

21. A. V. Shahraam and T. M. Monro, "A full vectorial model for pulse propagation in emerging waveguides with subwavelength structures part I: Kerr nonlinearity," Optics Express **17**, 2298-2318 (2009).

22. M. D. Turner, T. M. Monro, and S. V. Afshar, "A full vectorial model for pulse propagation in emerging waveguides with subwavelength structures part II: Stimulated Raman Scattering," Optics Express **17**, 11565-11581 (2009).
23. R. M. Osgood, N. C. Panoiu, J. I. Dadap, X. Liu, X. Chen, I. W. Hsieh, E. Dulkeith, W. M. J. Green, and Y. A. Vlasov, "Engineering nonlinearities in nanoscale optical systems: physics and applications in dispersion-engineered silicon nanophotonic wires," Advances in Optics and Photonics **1**, 162-235 (2009).
24. X. G. Chen, N. C. Panoiu, and R. M. Osgood, "Theory of Raman-mediated pulsed amplification in silicon-wire waveguides," IEEE Journal of Quantum Electronics **42**, 160-170 (2006).
25. R. A. Soref and B. R. Bennett, "Electrooptical effects in silicon," IEEE Journal of Quantum Electronics **23**, 123-129 (1987).
26. J. Zhang, Q. Lin, G. Piredda, R. W. Boyd, G. P. Agrawal, and P. M. Fauchet, "Anisotropic nonlinear response of silicon in the near-infrared region," Applied Physics Letters **91**(2007).
27. K. J. Blow and D. Wood, "Theoretical description of transient stimulated Raman-scattering in optical fibers," IEEE Journal of Quantum Electronics **25**, 2665-2673 (1989).
28. A. D. Bristow, N. Rotenberg, and H. M. van Driel, "Two-photon absorption and Kerr coefficients of silicon for 850-2200 nm," Applied Physics Letters **90**, 191104-191106 (2007).

29. Q. Lin, J. Zhang, G. Piredda, R. W. Boyd, P. M. Fauchet, and G. P. Agrawal, "Dispersion of silicon nonlinearities in the near infrared region," Applied Physics Letters **91**, 021111-021113 (2007).

30. P. L. Francois, "Nonlinear propagation of ultrashort pulses in optical fibers - total field formulation in the frequency-domain," Journal of the Optical Society of America B-Optical Physics **8**, 276-293 (1991).

31. W. H. Press, S. A. Teukolsky, W. T. Vetterling, and B. P. Flannery, *Numerical Recipes 3rd Edition: The Art of Scientific Computing* (Cambridge University Press, New York, 2007).

32. X. P. Liu, R. M. Osgood, Y. A. Vlasov, and W. M. J. Green, "Mid-infrared optical parametric amplifier using silicon nanophotonic waveguides," Nature Photonics **4**, 557-560 (2010).

33. W. Astar, J. B. Driscoll, X. P. Liu, J. I. Dadap, W. M. J. Green, Y. A. Vlasov, G. M. Carter, and R. M. Osgood, "Conversion of 10 Gb/s NRZ-OOK to RZ-OOK utilizing XPM in a Si nanowire," Optics Express **17**, 12987-12999 (2009).

34. J. B. Driscoll, W. Astar, X. Liu, J. I. Dadap, W. M. J. Green, Y. A. Vlasov, G. M. Carter, and R. M. Osgood, "All-Optical Wavelength Conversion of 10 Gb/s RZ-OOK Data in a Silicon Nanowire via Cross-Phase Modulation: Experiment and Theoretical Investigation," IEEE Journal of Selected Topics in Quantum Electronics **16**, 1448-1459 (2010).

35. S. J. McNab, N. Moll, and Y. A. Vlasov, "Ultra-low loss photonic integrated circuit with membrane-type photonic crystal waveguides," Optics Express **11**, 2927-2939 (2003).

36. S. Assefa, C. Jahnes, and Y. Vlasov, "CMOS compatible integrated dielectric optical waveguide coupler and fabrication," US Patent US7738753B2 (2010).

Chapter 3

Self-steepening of ultrashort pulses in silicon nanophotonic wires

3.1 Introduction

In recent years, research in the optical properties of deep subwavelength guiding structures, such as silicon nanophotonic wires fabricated on a silicon-oninsulator material system, has grown at an increasing rate [1-5]. Since one of the main applications envisioned for silicon nanophotonic wires is that of chip-to-chip or intrachip ultrafast optical interconnects, significant efforts have been devoted to the understanding of the properties of picosecond [6-8] and subpicosecond [9, 10] pulse dynamics in these guiding structures.

The tight optical-field confinement achieved in silicon nanophotonic wires leads to a strong dependence of the mode profile on both the wire geometry and the material parameters and thus to a large frequency dispersion of their linear optical properties [7, 11, 12]. It is thus expected that the nonlinear properties of silicon nanophotonic wires will also show large frequency dispersion, which would play a significant role in the dynamics of ultrashort or ultrabroad optical pulses [13]. A strong frequency dependence of the optical nonlinearity leads to significant pulse reshaping, through pulse self-steepening or optical shock formation [14], and thus dramatically affects both the temporal and the spectral pulse evolution. In this chapter these nonlinear optical phenomena in silicon nanophotonic wires are investigated.

3.2 Dispersion and shock time in silicon nanophotonic wires

A silicon nanophotonic wire considered in this chapter consists of a silicon strip with width *w* and height *h*, placed on top of a SiO_2 substrate. As discussed in Section 2.1 of Chapter 2, the linear optical properties of such devices are primarily determined by the waveguide modes and the propagation constant, β. In addition, the frequency-dependent $\beta(\omega)$ defines the group velocity $v_g = d\omega / d\beta$ and n^{th}-order dispersion terms $\beta_n = d^n\beta / d\omega^n$. These quantities are determined using the method describe in Section 2.1 of Chapter 2 for two waveguides with $w \times h$ = 360 nm × 220 nm and $w \times h$ = 600 nm × 300 nm. Simulations show that these waveguides support only the fundamental quasi-TE mode. Thus, the silicon nanophotonic wire with $w \times h$ = 360 nm × 220 nm ($w \times h$ = 600 nm × 300 nm) has a zero-dispersion point at λ_z = 1550 nm (1325 and 2409 nm) and anomalous group-velocity dispersion (GVD) for $\lambda < \lambda_z$ ($\lambda_{z1} < \lambda < \lambda_{z2}$).

The shock time τ_s is fully determined by $\tau_s = \partial \ln(\gamma) / \partial\omega = \tau_0 + \tau_{wm}$, where $\gamma = 3\omega\Gamma / 4\varepsilon_0 A_0 v_g^2$ is the frequency-dependent waveguide nonlinearity parameter, $\tau_0 = 1/\omega$ is related to the non-instantaneous response of the nonlinearity in a bulk material, and $\tau_{wm} = \partial \ln(\Gamma / v_g^2) / \partial\omega$ gives the waveguide contribution (see Section 2.2.1 of Chapter 2 for details). Thus, to characterize this nonlinear effect, γ was first determined by using the waveguide modes and the propagation constant β and then calculated numerically by taking the derivative of its natural logarithm with respect to ω. The coefficient γ depends on $\chi^{(3)}$ so that the frequency dispersion of the material optical nonlinearity is incorporated in this procedure by using the experimentally measured frequency-dependent $\chi^{(3)}$ [15].

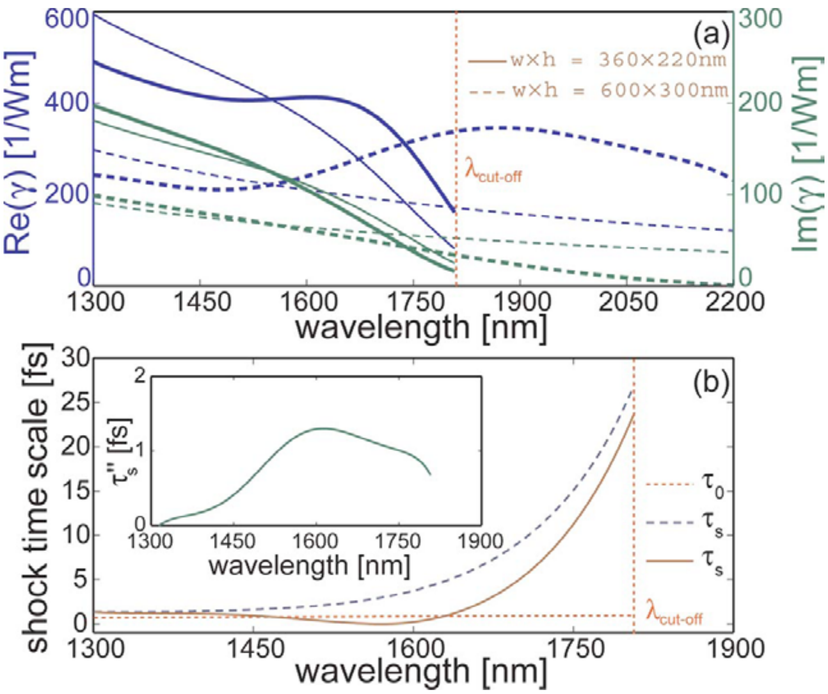

Figure 3-1 (a) Real and imaginary parts of γ versus λ, determined in the case when only the waveguide dispersion is considered (thin curves) and when both the material and the waveguide dispersion are included (thick curves). (b) Real part of τ_s when the frequency dependence of $\chi^{(3)}$ is neglected (dashed curves) and when it is included (solid curve). The inset shows the imaginary part of τ_s versus λ.

Figure 3-1(a) shows the dependence effective nonlinearity parameter $\gamma(\lambda)$, determined both for the case in which only the waveguide dispersion is considered ($\chi^{(3)}$ is set to be constant) and for the more general case when both the material and the waveguide dispersion are included. Figure 3-1(a) shows that γ depends strongly on wavelength for both silicon nanophotonic wires. For the one with $w \times h$ = 360 nm × 220 nm (solid curve), both the real and the imaginary parts of γ decreasing more than three times within a spectral domain of 600 nm. This large decrease of γ at long wavelengths is due to the fact that as the wavelength approaches the cutoff wavelength the mode becomes less confined in the silicon core, and thus a smaller amount of power is guided within the region with optical nonlinearity. This is consistent with the observation that the larger silicon waveguide with $w \times h$ = 600 nm × 300 nm shows less reduction in γ with the increasing λ. In addition, before cut-off the magnitude of γ for the waveguide with $w \times h$ = 360 nm × 220 nm is larger than that of the waveguide with $w \times h$ = 600 nm × 300 nm. This is a direct consequence of reduced optical model area. Furthermore, such large frequency dispersion of γ leads to a large "optical shock" time.

These conclusions are confirmed by the frequency dependence of τ_s, calculated for the waveguide with $w \times h$ = 360 nm × 220 nm; the results are summarized in Figure 3-1(b). The most notable conclusion illustrated in Figure 3-1(b) is that for silicon nanophotonic wire the shock time can be as large as 25 fs, i.e., more than an order of magnitude larger than that in photonic crystal fibers (PCFs) [16]. As just discussed, it is especially large in the vicinity of the cutoff wavelength. In addition, unlike the case of optical fibers or PCFs, τ_s has a significant imaginary part, τ_s'', which stems from the frequency dispersion of $\chi''^{(3)}$ of silicon. As the following sections will show, this is responsible for a shift of the pulse spectra toward longer wavelengths.

3.3 Ultrafast pulse dynamics in silicon nanophotonic wires

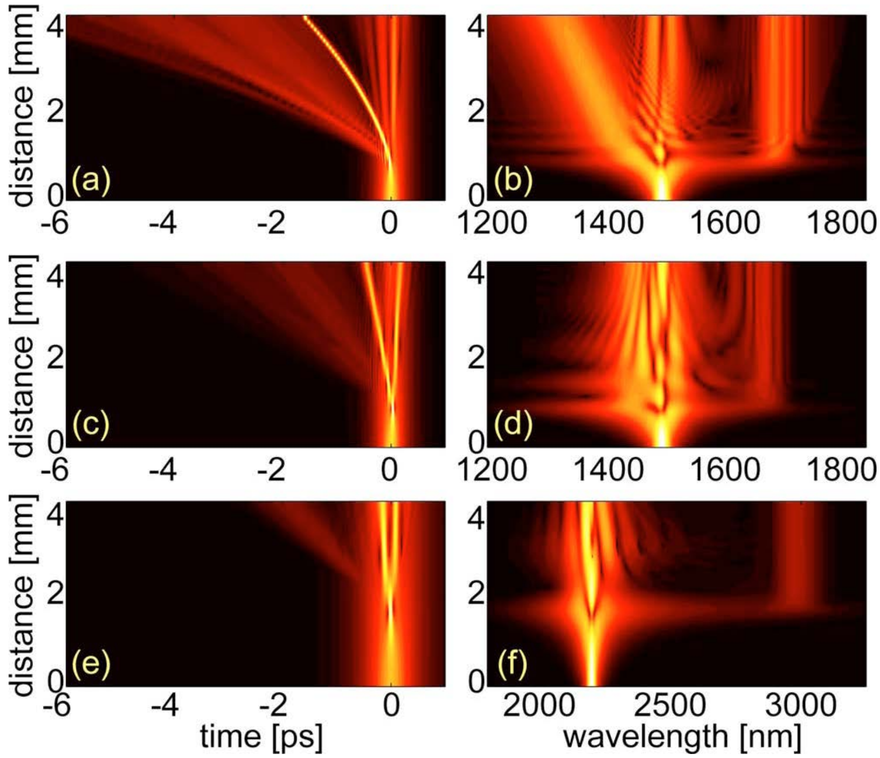

Figure 3-2 Pulse propagation in a L = 4 mm long silicon nanophotonic wire. Left column shows the pulse evolution in time domain while right column in frequency domain. (a) and (b) $\tau_s = \tau_0 = 0.8$ fs ($\tau_{wm} = 0$), (c) and (d) $\tau_0 = 0.8$ fs and $\tau_{wm} = 7.5 + i0.77$ fs, (e) and (f) $\tau_s = \tau_0 = 1.17$ fs.

The evolution of a sech-shaped pulse with λ_0 = 1500 nm, T_0 = 100 fs, and peak power P = 9 W in the silicon nanophotonic wire with $w \times h$ = 360 nm × 220 nm is considered in this chapter to study the influence of self-steepening effects on the propagation of ultrashort optical pulses in silicon nanophotonic wires. Then, the dispersion length $L_D = T_0^2 / |\beta_2|$ = 2.5 mm, γ' = 446.5 $W^{-1}m^{-1}$, and thus the nonlinear length $L_{NL} = 1/\gamma' P$ = 0.25 mm and the soliton number is $N_s = \sqrt{L_D / L_{NL}}$ = 3.18. To begin with, the TPA is neglected; however, the FC effects are included in our analysis. The theoretical model used here to account for the dynamics of an ultrafast pulse propagating in silicon nanophotonic wire is explained in great details in Section 2.2.1 of Chapter 2. Essentially the pulse dynamics is determined by a perturbed nonlinear Schrödinger equation (NLSE),

$$\begin{aligned} i\frac{\partial u}{\partial z}+\sum_{n\geq 1}\frac{i^n\beta_n}{n!}\frac{\partial^n u}{\partial t^n} &= -\frac{ic\kappa}{2n_{si}v_g}\left(\alpha_{\ln}+\alpha_{FC}\right)u-\frac{\omega\kappa}{n_{si}v_g}\delta n_{FC}u \\ &-\frac{3\omega P\Gamma}{4\varepsilon_0 A_0 v_g^2}\left(1+i\tau_s\frac{\partial}{\partial t}\right)|u|^2 u, \end{aligned} \tag{3.2.1}$$

and by an equation governing the carrier dynamics,

$$\frac{\partial N}{\partial t}=-\frac{N}{t_c}+\frac{3P^2\Gamma''}{4\varepsilon_0\hbar A_0^2 v_g^2}|u|^4. \tag{3.2.2}$$

The results obtained by integrating Eqs. (3.2.1) and (3.2.2) are shown in Figure 3-2. Thus, as shown in Figure 3-2(a) and (b), when the waveguide contribution to τ_s is neglected, τ_{wm} = 0, the pulse splits into three solitons that subsequently emit radiation at a frequency shifted by $\delta\omega=3|\beta_2|/\beta_3$ from the soliton frequency [17], i.e., λ_{rad} ~ 1740 nm. Moreover, in the temporal domain, the soliton with the largest peak power is accelerated and its temporal position is shifted toward the front of the pulse, whereas in the spectral domain, this same soliton is shifted toward the blue side of the spectrum. These features of the pulse evolution are explained by the nonlinear losses induced by FCs. Thus, Eq. (3.2.1) shows that these optical losses are proportional to $\int_{-\infty}^{t}\left|u\left(z,t'\right)\right|^4 dt'$, which means that the optical loss at the front of the pulse is smaller than the loss in its tail. As the soliton propagates in the anomalous GVD region, the redshifted frequency components move more slowly than the blueshifted ones, and thus the redshifted components are absorbed more strongly. Hence the soliton is slowly shifted toward the blue side of the spectrum. In contrast, the solitons with a smaller peak power induce a much smaller nonlinear loss, and thus this shifting is less pronounced. Now consider the very different evolution of the input pulse when the contribution of the waveguide to τ_s is included. As shown in Figure 3-2(c) and (d), the shift of the pulse now, both in time and frequency, almost vanishes. The decrease in the soliton frequency shift can be attributed to τ_s''. Thus, if $\tau_{wm}'' \neq 0$, Eq. (3.2.1) contains a term proportional to $\tau_{wm}'' u \partial |u|^2 / \partial t$, a term which in optical fibers describes the intrapulse Raman scattering. As it is known, it leads to a shift of the soliton spectrum toward longer wavelengths, and thus it cancels the blueshift induced by the FCs. Note that such dynamics are unique to silicon nanophotonic wires, as for optical fibers $\tau_{wm}'' = 0$, and no FCs are generated.

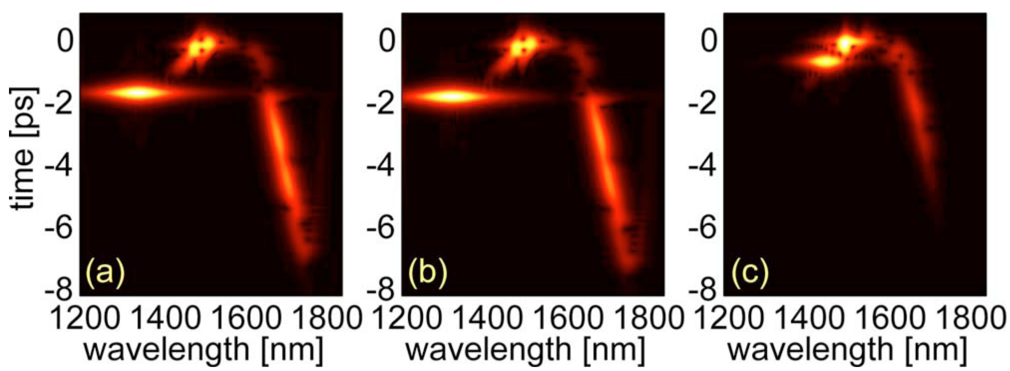

Figure 3-3 Pulse spectrograms calculated for (a) $\tau_s = 0$, (b) $\tau_0 = 0.8$ fs, $\tau_{wm} = 0$, and (c) $\tau_0 = 0.8$ fs, $\tau_{wm} = 7.5 + i0.77$ fs. In all cases the propagation distance is L = 4 mm.

It is expected that the TPA would affect the pulse dynamics that we just described; however, TPA losses are negligible if $\lambda \geq$ 2200 nm, and thus their effects can be reduced by a proper choice of the pulse wavelength. Thus, it is shown in Figure 3-2(e) and (f) the propagation of a pulse with λ_0 = 2200 nm and power P = 9 W in the silicon nanophotonic wire with $w \times h$ = 600 nm × 300 nm. To keep N_s unchanged, the pulse width is modified to T_0 = 180 fs. Figures 3-2(e) and (f) show that the soliton shift almost vanishes which is because the reduced TPA leads to the generation of fewer FCs.

These predictions are also corroborated by the pulse spectrograms shown in Figure 3-3, which are defined as $S(\omega,\tau) = \left|\int_{-\infty}^{\infty} u(z,t) u_{ref}(t-\tau) \exp(i\omega t) dt\right|$, where u_{ref} is a reference pulse; in calculations presented here the input pulse was used for u_{ref}. Thus, it can be seen that the pulse spectrograms for $\tau_s = 0$ and $\tau_s = \tau_0$ are very similar, which shows that the influence of the dispersion of the bulk nonlinearity on the pulse dynamics is rather small. However, these pulse dynamics are strongly modified when we add the contribution of the waveguide. Since in this case, too, three solitons are generated, this spectrogram is topologically similar to the other two; however, as we discussed, the additional term proportional to τ''_{wm} significantly reduces the temporal soliton shift.

3.4 Conclusion

This chapter characterizes the frequency dispersion of the optical nonlinearity of silicon nanophotonic wires and its effects on ultrashort optical pulses propagating in such nanophotonic wires. It is shown that the shock time in silicon nanophotonic wires can be as large as a few tens of femtoseconds. Remarkably, since the Raman effects for ultrashort pulses propagating in silicon nanophotonic wires are negligible, this chapter shows that, unlike the case of optical fibers or PCFs, the self-steepening is the dominant higher-order nonlinear effect.

Reference

1. R. L. Espinola, R. U. Ahmad, F. Pizzuto, M. J. Steel, and R. M. Osgood, "A study of high-index-contrast 90 degrees waveguide bend structures," Optics Express **8**, 517-528 (2001).
2. Y. A. Vlasov and S. J. McNab, "Losses in single-mode silicon-on-insulator strip waveguides and bends," Optics Express **12**, 1622-1631 (2004).
3. V. R. Almeida, C. A. Barrios, R. R. Panepucci, M. Lipson, M. A. Foster, D. G. Ouzounov, and A. L. Gaeta, "All-optical switching on a silicon chip," Optics Letters **29**, 2867-2869 (2004).
4. R. Claps, V. Raghunathan, D. Dimitropoulos, and B. Jalali, "Anti-Stokes Raman conversion in silicon waveguides," Optics Express **11**, 2862-2872 (2003).
5. H. S. Rong, R. Jones, A. S. Liu, O. Cohen, D. Hak, A. Fang, and M. Paniccia, "A continuous-wave Raman silicon laser," Nature **433**, 725-728 (2005).
6. O. Boyraz, T. Indukuri, and B. Jalali, "Self-phase-modulation induced spectral broadening in silicon waveguides," Optics Express **12**, 829-834 (2004).
7. X. G. Chen, N. C. Panoiu, and R. M. Osgood, "Theory of Raman-mediated pulsed amplification in silicon-wire waveguides," IEEE Journal of Quantum Electronics **42**, 160-170 (2006).

8. E. Dulkeith, Y. A. Vlasov, X. G. Chen, N. C. Panoiu, and R. M. Osgood, "Self-phase-modulation in submicron silicon-on-insulator photonic wires," Optics Express **14**, 5524-5534 (2006).

9. G. W. Rieger, K. S. Virk, and J. F. Young, "Nonlinear propagation of ultrafast 1.5 mu m pulses in high-index-contrast silicon-on-insulator waveguides," Applied Physics Letters **84**, 900-902 (2004).

10. I. W. Hsieh, X. G. Chen, J. I. Dadap, N. C. Panoiu, R. M. Osgood, S. J. McNab, and Y. A. Vlasov, "Ultrafast-pulse self-phase modulation and third-order dispersion in Si photonic wire-waveguides," Optics Express **14**, 12380-12387 (2006).

11. A. C. Turner, C. Manolatou, B. S. Schmidt, M. Lipson, M. A. Foster, J. E. Sharping, and A. L. Gaeta, "Tailored anomalous group-velocity dispersion in silicon channel waveguides," Optics Express **14**, 4357-4362 (2006).

12. X. P. Liu, W. M. J. Green, X. G. Chen, I. W. Hsieh, J. I. Dadap, Y. A. Vlasov, and R. M. Osgood, "Conformal dielectric overlayers for engineering dispersion and effective nonlinearity of silicon nanophotonic wires," Optics Letters **33**, 2889-2891 (2008).

13. I. W. Hsieh, X. G. Chen, X. P. Liu, J. I. Dadap, N. C. Panoiu, C. Y. Chou, F. N. Xia, W. M. Green, Y. A. Vlasov, and R. M. Osgood, "Supercontinuum generation in silicon photonic wires," Optics Express **15**, 15242-15249 (2007).

14. G. P. Agrawal, *Nonlinear Fiber Optics* (Academic, San Diego, 2001).

15. A. D. Bristow, N. Rotenberg, and H. M. van Driel, "Two-photon absorption and Kerr coefficients of silicon for 850-2200 nm," Applied Physics Letters **90**, 191104-191106 (2007).

16. M. A. Foster, J. M. Dudley, B. Kibler, Q. Cao, D. Lee, R. Trebino, and A. L. Gaeta, "Nonlinear pulse propagation and supercontinuum generation in photonic nanowires: experiment and simulation," Applied Physics B-Lasers and Optics **81**, 363-367 (2005).

17. P. K. A. Wai, C. R. Menyuk, Y. C. Lee, and H. H. Chen, "Nonlinear pulse-propagaion in the neighborhood of the zero-dispersion wavelength of monomode optical fibers," Optics Letters **11**, 464-466 (1986).

Chapter 4

Cross-phase modulation based wavelength-conversion of telecommunication RZ-OOK date

4.1 Introduction

Wavelength conversion has been carried out in nonlinear devices using a pump-probe configuration, where the mechanism was typically either four-wave mixing (FWM) or cross-phase modulation (XPM). Wavelength conversion by FWM (FWM-WC) and by XPM (XPM-WC) are possible in either active devices such as semiconductor optical amplifiers (SOAs) [1], or in passive devices such as chalcogenide waveguides [2], optical fiber [3], or silicon nanophotonic wires [4-10].

In its simplest configuration, XPM-WC utilizing an SOA generates an XPM-broadened probe which is subsequently isolated and processed through convolution with a bandpass filter [11-16]. However, since the technique requires detuning the filter relative to the probe carrier to affect the conversion, the optical signal-to-noise ratio (OSNR) of the converted probe will be significantly lower than that of the input continuous wave (CW) probe [17]. While an SOA has been widely used in such experiments due to the potential of signal gain, the device is relatively sophisticated to fabricate, requiring multiple lithographic and etch steps. In addition, an SOA is an active device that requires current-injection circuitry and heat-sink control.

An alternative to the SOA is the passive nonlinear waveguide, potentially a compact device that requires no control electronics. In one demonstration, 40-Gb/s XPM-WC was successfully carried out in a 22.5-cm-long, passive As_2S_3 waveguide [18]. Another possible candidate is the Si nanophotonic wire [19, 20], since the waveguide's sub-micrometer dimensions and its large index-of-refraction contrast result in a very high modal confinement that enhances the nonlinear effect of crystalline Si, allowing compact device lengths < 1 cm. In the silicon nanophotonic wire, the Kerr effect is linked to two-photon absorption (TPA) through the complex third-order nonlinear susceptibility ($\chi^{(3)}$) of Si [21]. TPA in Si can be prominent at telecommunication wavelengths, leading to cross-absorption modulation (XAM), free-carrier absorption (FCA) and free-carrier dispersion (FCD). TPA-induced FCA leads to pump depletion and self-limiting, while the resultant FCD can counteract the nonlinear phase shift due to the Kerr effect [22, 23]. Fortunately, the effective free-carrier lifetime is mitigated to < 1 ns due to enhanced carrier surface recombination at the boundaries of the waveguide, for waveguides of small cross-sections such as Si nanophotonic wire [22, 24-26]. XPM wavelength conversion in Si nanowires has been carried out using either Kerr-effect XPM [22, 27], or FCD-induced XPM [25]. The first demonstration of Kerr-effect XPM in a Si waveguide was by Boyraz *et al.* [22], where the pump was a ~ 1 ps, 20 MHZ pulse train generated by a mode-locked fiber parametric oscillator. Wavelength conversion based on FCD-induced XPM has also been achieved [25], where a 3.5 ps, 76.8 MHz pump generated by an optical parametric oscillator co-propagated with a CW probe. The probe was subsequently filtered by a grating offset by nm relative to the probe carrier. Using more realistic, 10 Gb/s data that modulated a 2.7-ps pulsed source, wavelength conversion via XPM in a Si nanophotonic wire was demonstrated by Driscoll *et al.* [27]. In that experiment, a fixed-wavelength, composite filter was offset relative to the probe by +0.6

nm, generating a wavelength-converted signal that demonstrated a receiver-sensitivity penalty of 0.7 dB; however that filter prevented an exploration of the tunability of XPM-WC within the C-band (1530–1565 nm). The wavelength of the resultant signal was also incompatible with the ITU-T grid. Moreover, and as in all past demonstrations [22, 25, 27], only one probe XPM side-band was investigated for the conversion. However, as the XPM pedestal generated at the probe is in general due to both Kerr-effect and FCD induced XPM, the XPM pedestal is asymmetric, so that processing the blue and the red side-bands may lead to different performances in XPM-WC.

This chapter investigates the effect of pump-probe detuning (PPD) on the efficacy of the XPM-WC technique in a Si nanophotonic wire both experimentally and numerically. Experimentally, a free-space tunable grating (FSTG) was configured to emulate the spectral pass-band of a commercial, standard 50-GHz DWDM AWG, and was utilized to filter either the red or the blue side-band of the XPM-broadened probe output by a Si nanophotonic wire, while the carrier wavelength of the probe was variably tuned. The wavelength of the converted signal was always compatible with the 50-GHz ITU-T grid. It was found that there was little difference in the BER performance of the two filtered side-bands. It was possible to achieve tunable wavelength conversion over a bandwidth of 20 nm while keeping the 10^{-9} BER receiver sensitivity penalty within approximately 0.5 dB relative to the case of the 5-nm-PPD (which exhibited penalty-free conversion).We also numerically investigate the effect of PPD on XPM-WC within the C-band through a comprehensive model. Results indicate little sensitivity to dispersion induced walk-off effects.

4.2 Experiments

4.2.1 Silicon nanophotonic wire properties

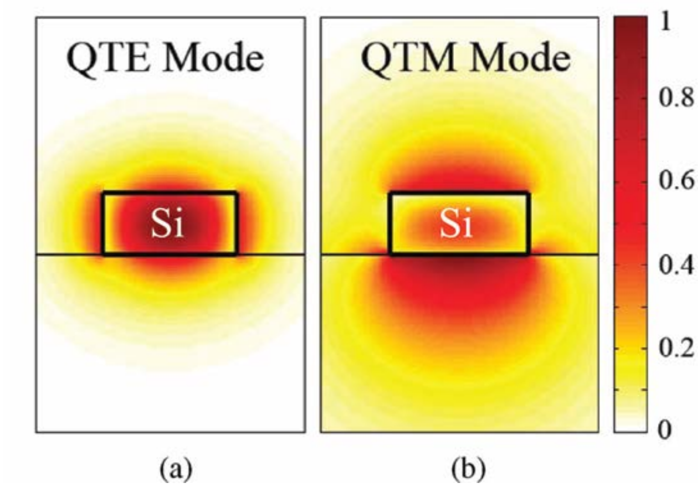

Figure 4-1 Major electric field distributions for optical modes supported by a 220 nm × 500 nm Si nanophotonic wire at λ = 1550 nm: (a) fundamental QTE (E_x component), (b) fundamental QTE (E_y component).

The silicon nanophotonic wire used in the experiment was fabricated in the Microelectronics Research Laboratory, at the IBM T. J. Watson Research Center, on a silicon-on-insulator (SOI) Unibond 200 mm wafer. It has a cross section of 220 nm × 500 nm ($h \times w$), and is ~ 4.8 mm in length (L). The top and bottom cladding layers for this wire are air and a 2μm-thick buried oxide (BOX) layer respectively. The optical access into/out-of the silicon nanophotonic wire is via lensed tapered fibers and SU8 polymer mode-converters. The silicon nanophotonic wire supports a fundamental quasi-TE (QTE) mode and a fundamental quasi-TM (QTM) mode in the C-band. Figure 4-1 shows the major electric field distribution of fundamental QTE and QTM at $\lambda = 1550$ nm calculated using a finite-element solver as explained in Section 2.1 of Chapter 2. The fundamental

QTM is weakly confined in the silicon core where the optical nonlinearity is originated. Thus this fundamental QTM does not possess an adequate effective nonlinearity. The experiment was carried out using only the fundamental quasi-TE mode due to its strong optical confinement and therefore a large nonlinearity. Consequently, the ensuing discussion will focus solely on the fundamental QTE mode. Linear propagation loss in the silicon wire was measured to be approximately α = 3.5 dB/cm in the C-band [20]. The dispersion coefficient of the wire is D_λ = 2300 ps/nm/km at λ = 1550 nm, yielding a total dispersion of 0.012 ps/nm for the device used, which is negligible for most practical, nearly transform-limited (TL) pulse-widths (> 1 ps). The effective nonlinear coefficient is γ = 320 $W^{-1}m^{-1}$.

4.2.2 Measurement setup

A transmission experiment was carried out on the pump to determine the onset of degenerate TPA (D-TPA) in the silicon wire, which causes optical limiting of the output power [28]. The pump was a 1555.5-nm, 4.8%-duty-cycle, 10-Gb/s pseudo-random bit sequence (PRBS) RZ-OOK, where the pulsed-source was a commercially available mode-locked laser diode (MLLD). It was found that the output pump power deviated from an initial linear trend due to D-TPA and FCA at an input average pump power of ~ 40 mW, and thus the wavelength conversion experiment was carried out at ~ 40 mW average pump power, which resulted in ~ 790 mW instantaneous peak power, assuming a TL-secant approximation for the pump pulse. The CW probe showed no sign of optical limiting due to insufficient peak power. The total linear loss of the device was thus estimated by finding the total insertion loss using the CW probe, and found to be 9 dB. Since the measured propagation loss was 3.5 dB/cm [20], the estimated coupling loss/facet was 3.7 dB. The respective coupled average and instantaneous peak pump powers at the input plane of the silicon nanophotonic wire were therefore 17 mW (12.3 dBm), and 337 mW (25.3 dBm).

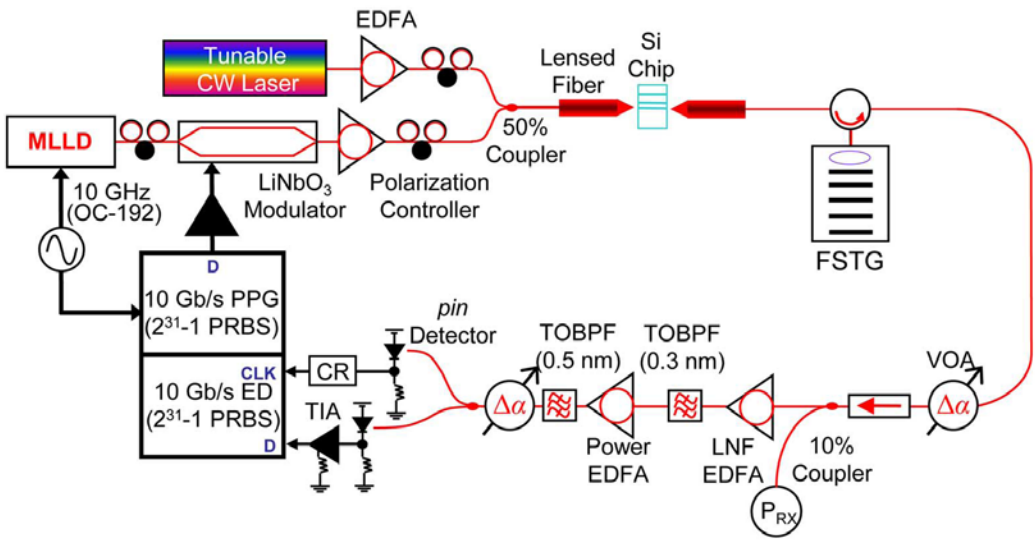

Figure 4-2 Experimental setup: MLLD = mode-locked laser diode, PPG = pulsed-pattern generator, ED = error detector, PRBS = Pseudo-random bit sequence, D = Data, CLK = Clock, EDFA = Er-doped fiber amplifier, TOBPF = tunable optical bandpass filter, FSTG = free-space tunable grating, VOA = variable optical attenuator ($\Delta\alpha$ = differential attenuation), P_{RX} = receiver power, LNF = low-noise figure, CR = clock recovery, TIA = transimpedance amplifier.

Figure 4-2 shows the setup for the wavelength conversion experiment. The average coupled probe power was 32 mW (15 dBm), measured at the waveguide’s input facet, and was sufficiently high to help overcome the waveguide coupling losses, and the intrinsic losses (~ 10 dB) of the components between the Si nanophotonic wire chip and the low-noise-figure Erbium-doped fiber amplifier (LNF-EDFA) that were required to carry out the receiver sensitivity measurements. An AWG could be used to selectively filter the probe output by the silicon wire. In the experiment however, a commercially available free-space tunable grating (FSTG)was used instead, and was configured to approximate the pass-band of a 50-GHz DWDM AWG, resulting in a full-width-at-half-maximum (FWHM) bandwidth of 35 GHz, and an insertion loss of ~ 3.5 dB. This approach ensured that the converted probe wavelength was consistent with the ITU-T 50-GHz grid. The pre-amplified receiver consisted of a 980-nm-pumped, dual-stage, linear high-gain LNF-EDFA, a tunable optical bandpass filter (TOBPF) to eliminate amplified spontaneous emission (ASE), a power amplifier, and another TOBPF. The optical signal was then split between a high-Q clock recovery (CR) module, and a *pin*-receiver. A variable optical attenuator (VOA) was installed before the pre-amplified receiver to vary the receiver power (measured using a calibrated 10% coupler installed before the LNF-EDFA), and to vary the OSNR, thus emulating ASE-limited transmission. Another VOA was used before the *pin*-receiver to maintain the average detected power constant throughout a receiver sensitivity measurement. The *pin*-detector input average power was approximately +5 dBm to ensure OSNR-limited measurements.

4.2.3 Wavelength conversion via XPM

Figure 4-3 shows the WDM spectrum output through the silicon wire compared to its input, at a resolution bandwidth (RB) of 0.1 Å. The spectral broadening observed in the pump is attributed to self-phase modulation (SPM) due to the degenerate Kerr-effect, and to FCD, due to D-TPA. The XPM-induced spectral broadening (or pedestal) of the probe is attributed to the non-degenerate Kerr-effect, as well as to FCD due to both D-TPA and non-degenerate TPA (ND-TPA). The CW probe also experienced XAM due to ND-TPA. The pump-probe detuning was restricted to > 4 nm to minimize cross-talk in the probe

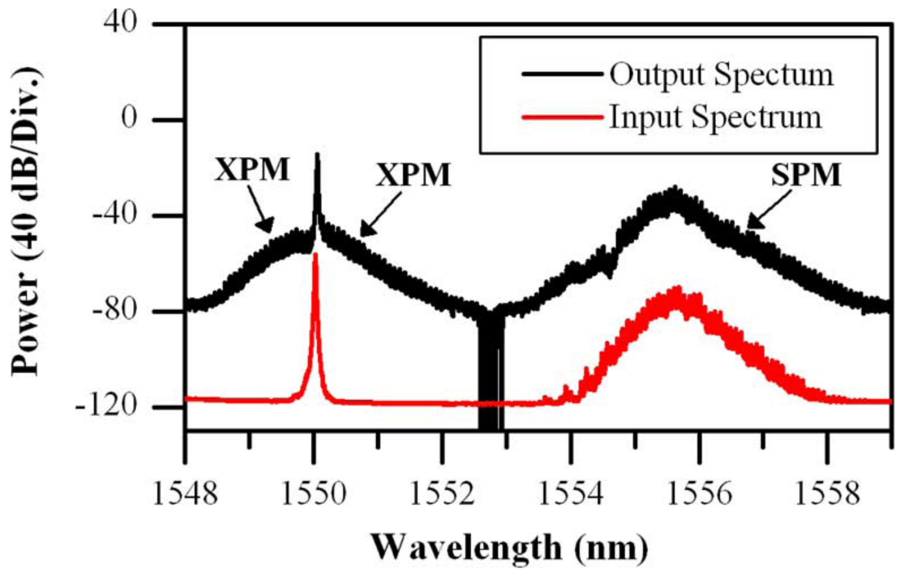

Figure 4-3 Signal spectra (resolution bandwidth (RB) = 0.1 Å). The spectra have been offset for clarity (SPM = self-phase modulation). The lower trace represents the input WDM spectrum, while the upper trace is the output WDM spectrum. The spectral notch at ~ 1553 nm was due to a resonance of a microring filter integrated with the silicon nanophotonic wire (only the through-port of the microring filter was used in the experiment).

that could have occurred due to SPM-broadening of the pump. Conversion of the XPM-induced phase-modulation to amplitude-modulation (PM-AM) could be achieved by processing either the blue or the red side-band of the spectrally broadened probe, as illustrated in Figure 4-4. The PM-AM conversion was made possible by the steep edges of the FSTG transfer function, which simultaneously enabled the suppression of the cross-modulated carrier by more than 25 dB (measured at a 0.1-Å RB, relative to the apex of the filtered probe spectrum). Suppression of the carrier was important as it would have resulted in coherent cross-talk of the XAM signal with the filtered probe in the *pin*-receiver. The spectral operation on the probe emulates the action of a commercial 50-GHz-DWDM, flat-top AWG, which might simultaneously filter both side-bands of the XPM pedestal, ensuring that the resultant signals are compatible with the ITU-T DWDM 50-GHz grid. Although the probe carrier OSNR/0.1 nm was > 45 dB at the output of the silicon nanophotonic wire, this was not the case for the filtered side-bands of the XPM pedestal: The estimated OSNR/0.1 nm was ~ 33 dB for each of the two ±50-GHz side-bands (measured prior to filtering, relative to background ASE level at an offset of ±3-nm).

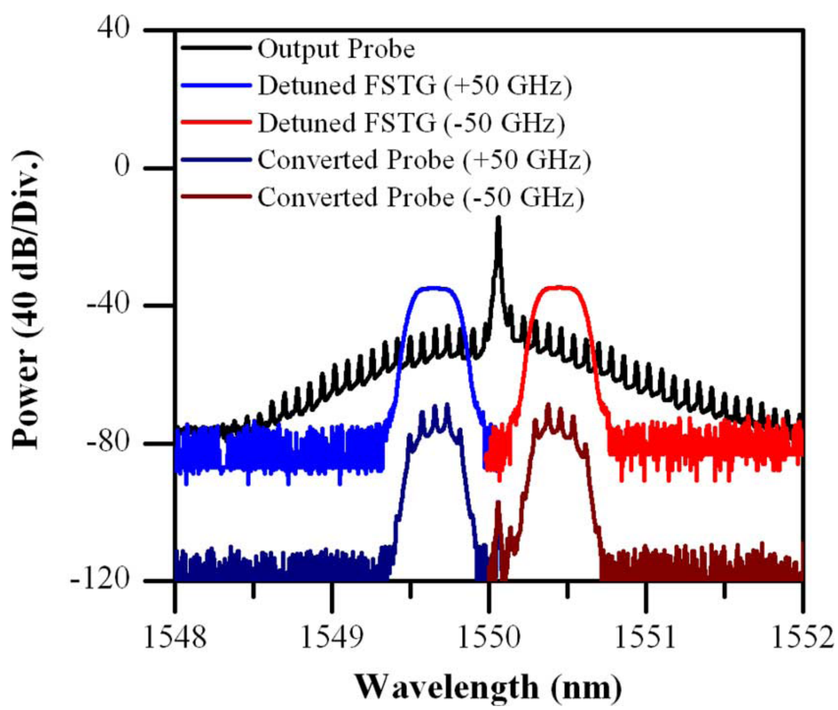

Figure 4-4 Location (±50 GHz) of the free-space tunable grating (FSTG) pass-band with respect to the XPM-induced pedestal at the probe carrier (RB = 0.1 Å).

4.2.4 Eye diagrams and BER test results

Figure 4-5 shows the resultant eye-diagrams for the ±50-GHz filtering operations. The eye-diagrams were captured after amplification with EDFA and subsequent filtering using the 0.5-nm filter (in Figure 4-2) because direct detection of the probe at the output of the FSTG was difficult due to its low power of ~ −23 dBm. Although there are differences in the ONE- and ZERO-rails of the baseline pump (a) and the converted probe (b, c), it should be emphasized that Figure 4-5 shows a very qualitative comparison, as the actual signal quality in all cases was obscured due to multiple convolutions, with the pre-amplified receiver (without which the observation of the probe was not possible), and the RF response of the OC-192 sampling module. The pulse-widths of the ±50-GHz side-bands were ~ 23-ps-FWHM, measured by autocorrelation (Figure 4-6) before the *pin*-receiver, assuming a TL-Gaussian shape.

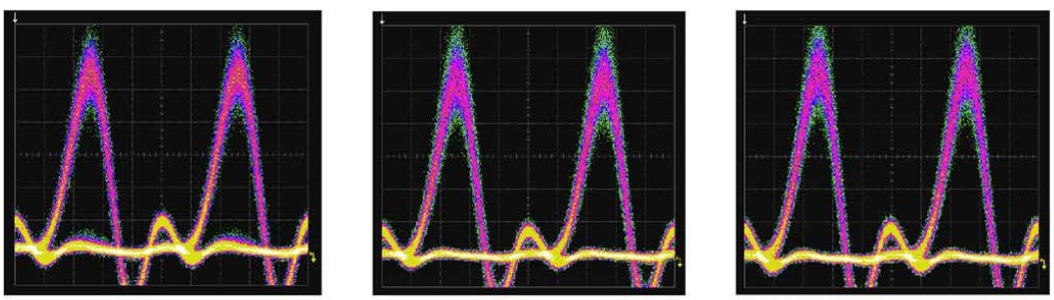

(a) (b) (c)

Figure 4-5 OC-192 opto-electronic sampling module traces (20 ps/division): (a) Baseline RZ-OOK pump, (b) Converted probe (+50 GHz), (c) Converted Probe (−50 GHz). The receiver power was ~ −30 dBm for all three cases. The ringing in the ZERO-rails was due to the radio-frequency (RF) response of the sampling module.

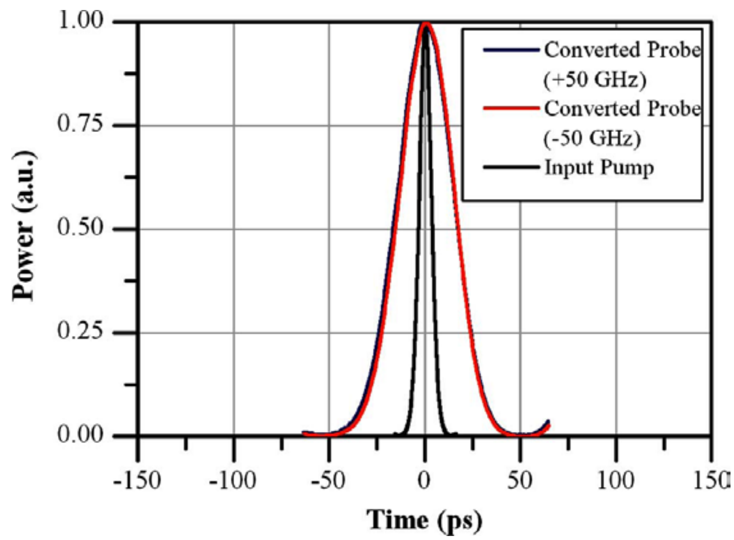

Figure 4-6 Autocorrelation measurement results. The Converted Probe cases were measured prior to detection (after the 0.5-nm TOBPF in Figure 4-2). The Input Pump was characterized prior to coupling to the Si nanophotonic wire. No shape factor was applied to any of the traces.

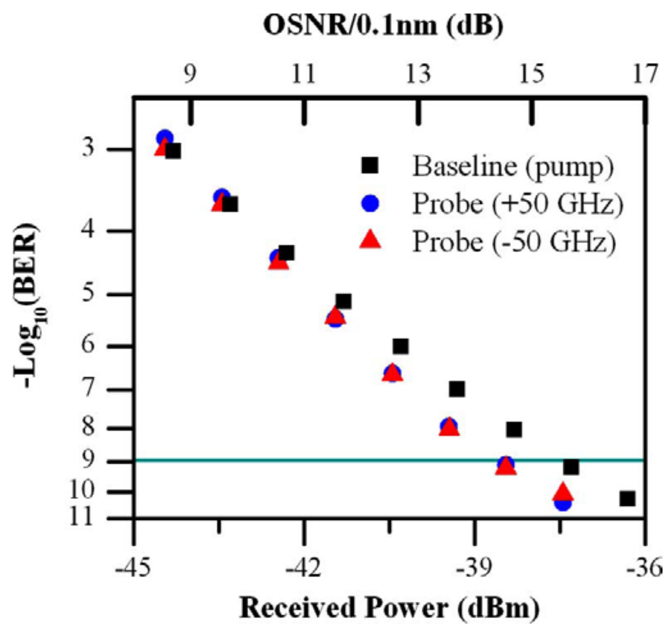

Figure 4-7 Logarithmic plot of the negative-logarithm of the measured BER versus the Received Power (P_{RX} in Figure 4-2). The plot also shows the BER performance versus OSNR (top axis).

A receiver sensitivity measurement was carried out on the ±50 GHz side-bands, and compared to that of the baseline pump (for which the Si nanophotonic wire was bypassed, and found by tuning the FSTG and both receiver filters to the carrier wavelength of the pump). Prior to detection of the probe, it was found that the probe carrier was suppressed by > 35 dB (measured at a RB = 0.1 Å, relative to the probe's apex). The results are shown in Figure 4-7: A 10^{-9}-BER receiver sensitivity enhancement of 1 dB was observed for a filtered probe side-band, compared to the pump. The BER-performance disparity is an unintended consequence of the use of a short duty-cycle pump pulse which resulted in a larger −3-dB-bandwidth of 0.62 nm, and also due to MLLD-transmitter chirp. Assuming a secant^2-fit, the estimated time-bandwidth-product of the input pump was 0.367, which is significantly higher than that (0.315) of a TL-secant pulse. It is also observed (in Figure 4-3) that the input pump spectrum demonstrates significant asymmetry. Since the effective −3-dB-bandwidth of the receiver's aggregate filter was only 25 GHz (while that of the pump was 77 GHz), the interaction of the spectrally broader chirped pump with the filter (as shown in Figure 4-8) would be expected to lead to a relative receiver sensitivity penalty, as explained by Winzer *et al.* [29]: A chirped signal requires a larger filter bandwidth to establish a balance between filter-induced signal energy rejection and detection noise. The BER-performance difference was also reflected in the respective BER decision threshold voltages, which were −2 mV for the baseline pump, and −10 mV for the ±50-GHz probe. A short pump pulse was required, to ensure a significant XPM pedestal in the probe, and therefore sufficient power, to overcome the output coupling losses, and the losses due to the components intermediate to the FSTG and the LNF-EDFA, that were required in the receiver sensitivity experiment (Figure 4-2).

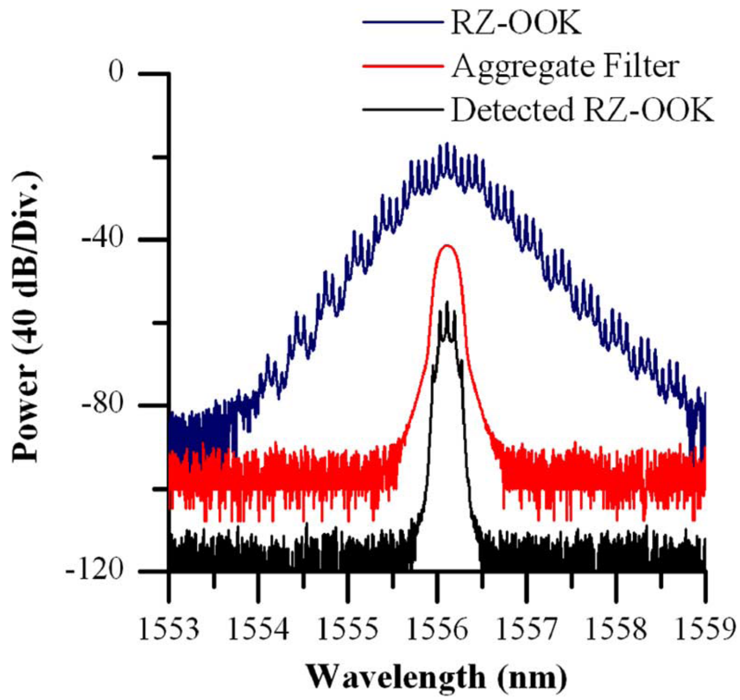

Figure 4-8 Summary of receiver filter operation on the pump (RB = 0.1 Å). The Aggregate Filter effectively includes all of the filters used in the receiver, and includes the FSTG.

The receiver sensitivity measurements definitively show that the converted probe was power-limited, and not OSNR-limited. This could be established from Figure 4-7, which demonstrates that the converted probe required only ~ 14.5 dB/0.1 nm OSNR to attain a 10^{-9}-BER, while the filtered probe's OSNR at the output of the silicon wire was ~ 33 dB/0.1 nm. Although such a high OSNR was clearly more than adequate for the receiver sensitivity measurement, the corresponding probe power was still required to overcome the output LF-silicon-wire coupling loss, and the total losses of the components intermediate to the Si chip and the receiver (LNF-EDFA) pre-amplifier.

It was also possible to verify the consistency of the receiver sensitivity measurement, with the NF of the LNF-EDFA preamplifier. The NF of the pre-amplifier may be gauged using the optical method of NF estimation, which is reliable for linear EDFAs, and under the assumption of a shot-noise-limited input signal. At 10^{-9}-BER, the signal power was in the range of −37 dBm to −39 dBm, for which the pre-amplifier gain was > 30 dB, which simplifies the computation of its NF to

$$\mathrm{NF}_{\mathrm{dB}} = P_{\mathrm{dBm}} - 30 - 10\log(h\upsilon B_0) - \mathrm{OSNR}_{\mathrm{dB}}. \qquad (4.2.1)$$

Substitution of probe received power (P_{dBm}) of −38.5 dBm, frequency (υ) of 193.35 THz, resolution bandwidth (B_0) of 12.5 GHz, and OSNR/0.1 nm (corrected for ASE within the signal bandwidth, and included in the measurement) of 14.6 dB, yields a NF of 4.8 dB. This value is close to that (4.5 dB) measured by the manufacturer of the EDFA.

4.2.5 Study of pump-probe detuning

The sensitivity of the technique to pump-probe detuning (PPD), and therefore temporal walk-off, was gauged by detuning the probe and the filters relative to the pump (which was not tunable beyond ±50 GHz). The BER decision threshold voltage was kept at −10 mV over the entire wavelength range considered. The PPD was limited to between 1535 nm (due to the range of the TOBPFs) and 1560 nm (due to the aggregate gain response of the EDFAs used). The 10^{-9}-BER receiver sensitivity penalty at a given probe wavelength was measured relative to that at 1550 nm (PPD = −5 nm), which required the lowest receiver power. Figure 4-9 shows that the penalty can be kept to about 0.5 dB over a PPD of 20 nm, demonstrating that dispersion-induced walk-off in the silicon nanophotonic wire was not significant. Some of the scatter in the data is also attributed to some drift in the LF-silicon-wire coupling, and in the polarization states of the pump and the probe.

The variation of pulse-width with PPD was also characterized, and is shown in Figure 4-10. The probe pulse-width was measured by autocorrelation (as previously described for Figure 4-6), before detection in the receiver. Both ±50-GHz side-bands demonstrated a similar overall trend, with deviations once again attributed mainly to some drift in the polarization states of the pump and the probe, and some experimental error. The maximum deviation over a PPD of 20 nm was about 5%, but had no effect on the receiver sensitivity measurements since the pulse-width was always under 33 ps [30]. ASE noise was not modeled due to the fact that the input and output OSNRs of the pump and the probe were high (> 30 dB/0.1 nm) in the experiments.

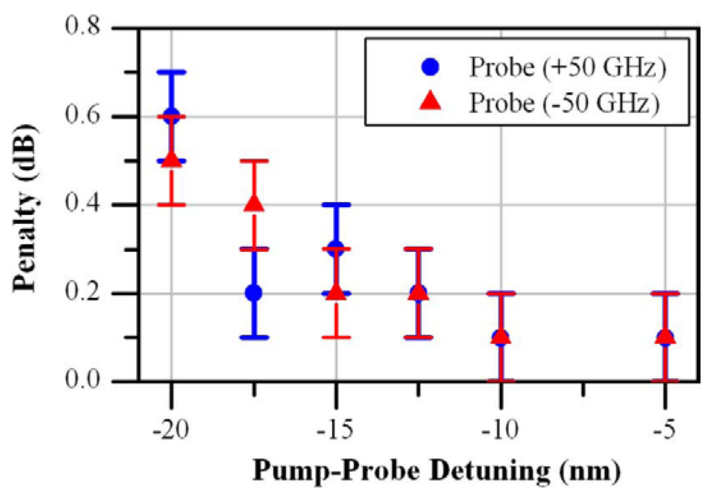

Figure 4-9 Probe 10^{-9}-BER receiver sensitivity penalty as a function of pump-probe detuning (PPD), relative to that at the PPD of –5 nm. The penalty at +5-nm-PPD (not shown above) was also close to that at PPD = –5 nm. Error-bars of ±0.1 dB indicated the uncertainty in the P_{RX} measured.

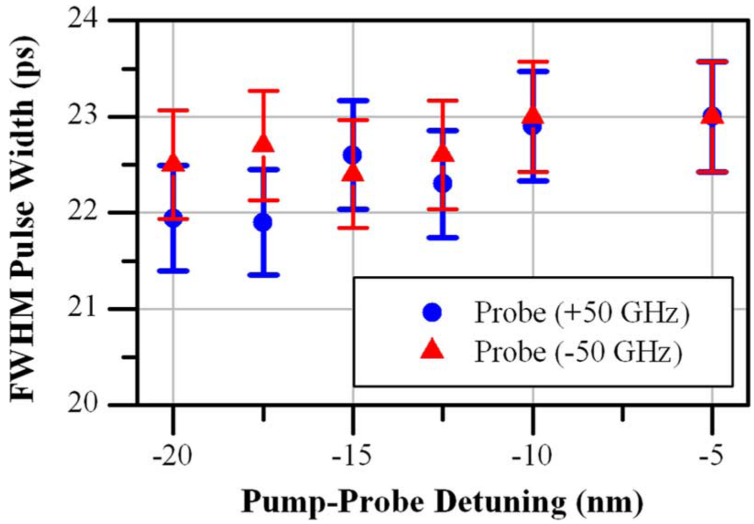

Figure 4-10 Variation of pulse-width with PPD. The pulse-width at +5-nm-PPD (not shown above) was ~ 23 ps. Error-bars of approximately ±0.5 ps indicate the uncertainty in the measurement.

4.3 Theoretical investigation

The dynamic interaction between the pump and probe in the Si nanophotonic wire was modeled using the method described in Section 2 of Chapter 2. The RZ-OOK data-bearing pump was modeled as a series of 4.8-ps-FWHM, TL-pulses centered at λ = 1555.5 nm, and modulated with a 2^5–1 PSRB periodically repeating ten times within the computational window. The CW probe was modeled as a single 10 MHz pulse, centered at λ = 1550.5 nm. The average power of the pump and the probe were set to 17 mW and 32 mW respectively, in accord with the experimentally estimated coupled values. Both the pump and the probe were assumed to propagate in the QTE mode (Figure 4-1), and a linear waveguide propagation loss of 3.5 dB/cm and free-carrier lifetime of 0.5 ns were assumed [20]. The modeled Si nanophotonic wire structure was as described in Section 4.2.1.

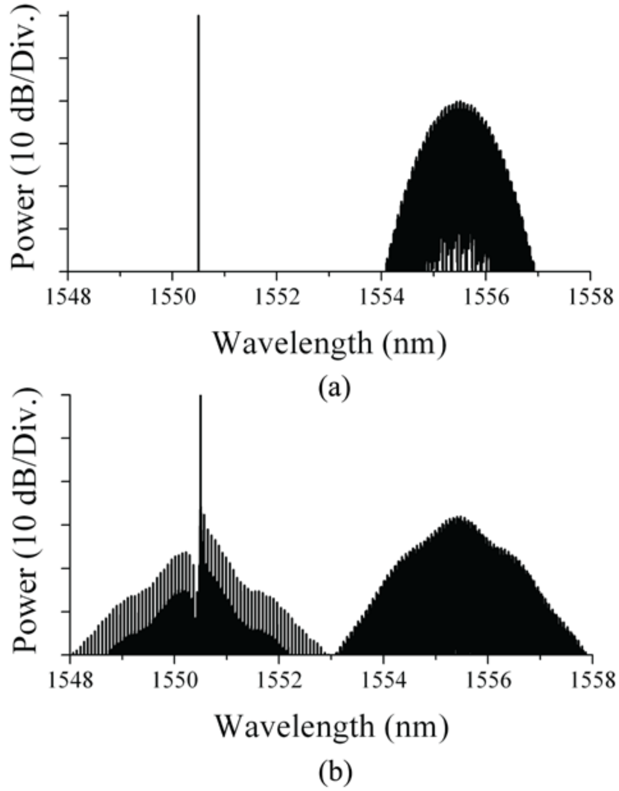

Figure 4-11 Spectra generated through numerical modeling, showing good agreement with the experimental spectra [Figure 4-3]. Both (a) input spectra and (b) output spectra are shown. Clear XPM-induced spectral broadening can be observed in the probe, which is asymmetric due to FCD.

Figure 4-11 shows the resultant simulated spectrum output by the 4.8-mm-long Si nanophotonic wire. The probe spectrum exhibits significant spectral broadening due to pump-induced XPM effects, which includes Kerr-effect XPM, D-TPA and ND-TPA-induced FCD, and XAM. The blue- and red-shoulders of the broadened probe show spectral asymmetry as a result of FCD [20]. Modulation sidebands are also present on the output probe, which is evidence of probe interaction with the data-bearing RZ-OOK pump.

The process of XPM-WC was also numerically modeled, where a filter was applied to the output probe spectrum (Figure 4-11(b)) to emulate the detuned filter used in the experiment. The filter power transfer function was modeled as a super-Gaussian

$$G(\upsilon) = \exp\left[-\left(\frac{\upsilon-\upsilon_0}{\Delta\upsilon}\right)^{2m}\right] \tag{4.3.1}$$

where *G* represents the frequency dependent power transmission spectrum, υ_0 the central frequency, $\Delta\upsilon$ the spectral bandwidth of the filter, and *m* a parameter defining the super-Gaussian order. Values for $\Delta\upsilon$ and *m* were chosen to be 19.17 GHz and 2 respectively, to produce a super-Gaussian with a −1-dB-FWHM of ~ 25 GHz, and −3-dB-FWHM of ~ 35 GHz, so as to emulate the channel pass-band of a commercial flat-top 50-GHz AWG, and the FSTG used in the experiment. The phase response $\left[\varphi(\upsilon)\right]$ of the filter was estimated by taking the Hilbert-transform (HT) of the filter amplitude response $\left[H(\upsilon) = G(\upsilon)^{1/2}\right]$

$$\varphi(\upsilon) = -\mathrm{HT}\left\{\ln\left|H(\upsilon)\right|\right\}. \tag{4.3.2}$$

The filter was detuned from the probe carrier by ±50 GHz to explore the effectiveness of filtering the blue- and red-edges of the XPM-broadened probe, as shown in Figure 4-12 (which agrees well with the experimental results of Figure 4-4). The optical components of the receiver were further modeled as 37.5-GHz and 62.5-GHz FWHM Gaussian filters in series [the phase response of each optical filter was also found via the HT according to Eq. (4.3.2)] and the sampling head was assumed to have an impulse response of 20 ps. The resulting detected signals were used to construct eye-diagrams, which indicate successful transfer of the data to a new wavelength (Figure 4-13). For the minimum pump-probe detuning of –5 nm, and for the pump power used in the simulation, there was no noticeable difference in converted signal quality between filtering on the blue- or the red-edge of the probe, since both resulted in clear eye-diagrams.

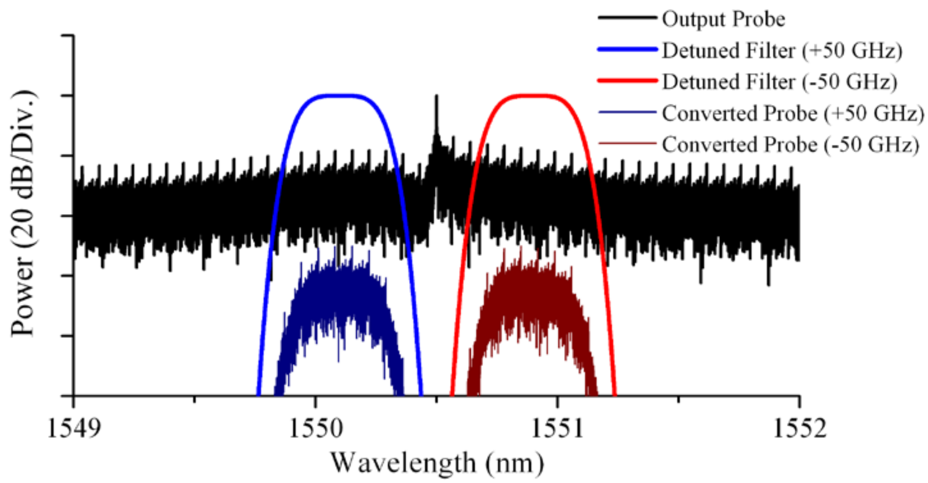

Figure 4-12 Numerically modeled result of filtering the XPM-broadened probe with the super-Gaussian filter, detuned by ±50 GHz. Spectra have been offset for clarity.

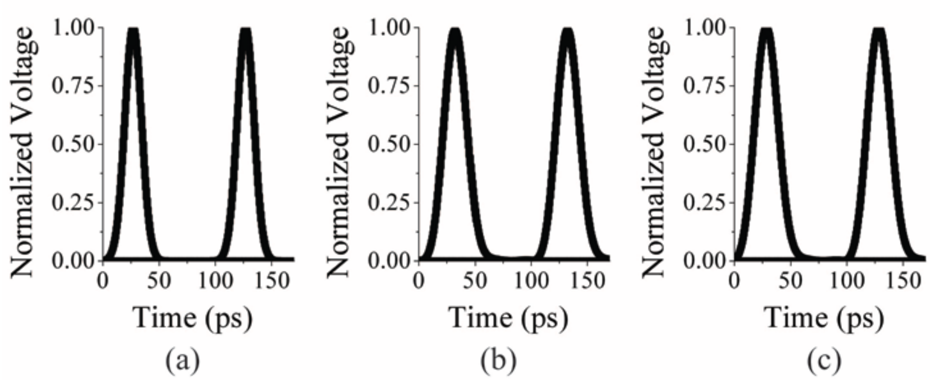

Figure 4-13 Numerically modeled eye-diagrams for (a) the input RZ-OOK pump, (b) converted probe (filter-probe detuning of +50 GHz), and (c) converted probe (filter-probe detuning of –50 GHz). Clear eye diagrams indicate successful transfer of the pump data to new wavelengths.

The tunability of XPM-WC can be limited by temporal walk-off between the pump and probe. The temporal walk-off time can be defined through co-propagating modes which temporally drift apart during propagation, based on differing group velocities

$$\tau_W = d\left|\beta_1^p - \beta_1^s\right|, \qquad (4.3.3)$$

where d is the propagation distance, and β_1^p (β_1^s) is the first-order dispersion parameter of the pump (probe). In analysis of XPM-WC tunability, we first set the pump to λ = 1555.5 nm, as in the experiment, and calculate the net temporal walk-off between the pump and the probe after propagation through a 4.8-mm Si nanophotonic wire (Figure 4-14). The result indicates that even for 25-nm PPD, the net temporal walk-off is only 0.28 ps, or < 6% of the pump FWHM. In fact, for the most extreme case where the pump is located at one edge of the C-band (λ = 1565 nm) and the probe at the other (λ = 1530 nm), the temporal walk-off is still only ~ 0.43 ps, which is < 9% the pump FWHM. Similarly, examination of the walk-off length

$$L_W = \frac{T_0}{\left|\beta_1^p - \beta_1^s\right|} \qquad (4.3.4)$$

defined as the propagation length required for the pump and probe to drift apart by at least the exponential-half-width (T_0) of the pump (~ 1.95 ps for a 4.8-ps-FWHM Gaussian pulse), indicates that the smallest in L_W the C-band is ~ 3.4 cm (Figure 4-14), much longer than the (L =) 4.8-mm device used in the experiment. It is important to compare this to the nonlinear length $L_{\mathrm{NL}} = \left(\gamma P_0\right)^{-1}$, where P_0 is the pulse peak power of the pump and γ is the effect nonlinear parameter. γ is ~ 330 $W^{-1}m^{-1}$ at λ = 1550.5 nm, and the peak power of the pump is ~ 0.66 W, leading to a L_{NL} of ~ 4.7 mm, which is much smaller than the walk-off length. The device physical length is thus ~ L_{NL} , and much shorter than L_W , allowing significant nonlinear effects to be realized.

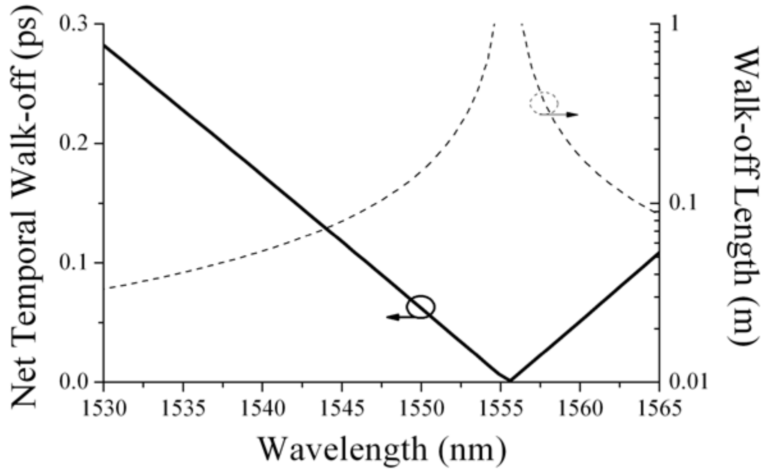

Figure 4-14 Net temporal walk-off after propagating through the Si nanophotonic wire ($d = L = 4.8$ mm), and walk-off length (plotted on a logarithmic scale) for a pump fixed at $\lambda = 1555.5$ nm and a probe tuned within the C-band. The pump and probe temporally walk-off by < 9% of the pump temporal FWHM, and the walk-off length is minimum at ~ 30 mm.

4.4 Conclusion

Tunable wavelength conversion by XPM in a Si nanowire has been investigated for the first time. It has also been demonstrated for the first time, that it is possible to use either the blue (+50 GHz) or the red (–50 GHz) side-band of the XPM broadened probe. The 10^{-9}-BER receiver sensitivity performance of the converted probe suffered ~ 0.5 dB maximum over a PPD range of 20 nm (relative to the case of the 5-nm PPD which showed penalty-free wavelength conversion), where the useful PPD was limited by the bandwidth of the filters and EDFAs used in the experiment.

A short 4.8-ps-pulsed pump was used in the proof-of-principle experiment. However, the experiment may be carried out with a more standard pulse (i.e., 33%-duty-cycle). The combined losses due to waveguide-fiber coupling (approximately 7.5 dB), and those due to the sub-optimal components used in the receiver sensitivity experiment (approximately 10 dB) precluded the use of standard duty-cycle pulses for the same average pump power. Such pulses would have required a prohibitively large average pump power of ~ 1 W to achieve the same received power required to attain 10^{-9} BER in the reported experiment, and would have also risked damage to the input polymer mode adapter; however a reduction of these two loss mechanisms, and/or the integration of some of the optical components on chip may allow the use of standard RZ-OOK pulses.

A thorough numerical model also demonstrated good agreement between theory and experiment by the construction of clear eye diagrams. In addition, numerical analysis shows that for pump and probe within C-band the temporal walk-off between is much smaller than the pulse FWHM and walk-off length is much larger than the device length as well as nonlinear length. This XPM-WC based technique thus is not limited by the walk-off.

Reference

1. G. Grosskopf, R. Ludwig, R. Schnabel, and H. G. Weber, "Frequency conversion with semiconductor laser amplifiers for coherent optical frequency division switching," in *Proc. IOOC'89*, Kobe, Japan, 1989, Paper 19C14-14.

2. F. Luan, M. D. Pelusi, M. R. E. Lamont, D. Y. Choi, S. Madden, B. Luther-Davies, and B. J. Eggleton, "Dispersion engineered As2S3 planar waveguides for broadband four-wave mixing based wavelength conversion of 40 Gb/s signals," Optics Express **17**, 3514-3520 (2009).

3. K. Inoue and H. Toba, "Wavelength conversion experiment using fiber 4-wave-mixing," IEEE Photonics Technology Letters **4**, 69-72 (1992).

4. R. L. Espinola, J. I. Dadap, R. M. Osgood, S. J. McNab, and Y. A. Vlasov, "C-band wavelength conversion in silicon photonic wire waveguides," Optics Express **13**, 4341-4349 (2005).

5. Q. Lin, J. D. Zhang, P. M. Fauchet, and G. P. Agrawal, "Ultrabroadband parametric generation and wavelength conversion in silicon waveguides," Optics Express **14**, 4786-4799 (2006).

6. K. Yamada, H. Fukuda, T. Tsuchizawa, T. Watanabe, T. Shoji, and S. Itabashi, "All-optical efficient wavelength conversion using silicon photonic wire waveguide," IEEE Photonics Technology Letters **18**, 1046-1048 (2006).

7. H. S. Rong, Y. H. Kuo, A. S. Liu, M. Paniccia, and O. Cohen, "High efficiency wavelength conversion of 10Gb/s data in silicon waveguides," Optics Express **14**, 1182-1188 (2006).

8. M. A. Foster, A. C. Turner, R. Salem, M. Lipson, and A. L. Gaeta, "Broad-band continuous-wave parametric wavelength conversion in silicon nanowaveguides," Optics Express **15**, 12949-12958 (2007).

9. J. I. Dadap, N. C. Panoiu, X. G. Chen, I. W. Hsieh, X. P. Liu, C. Y. Chou, E. Dulkeith, S. J. McNab, F. N. Xia, W. M. J. Green, L. Sekaric, Y. A. Vlasov, and R.

M. Osgood, "Nonlinear-optical phase modification in dispersion-engineered Si photonic wires," Optics Express **16**, 1280-1299 (2008).

10. B. G. Lee, A. Biberman, A. C. Turner-Foster, M. A. Foster, M. Lipson, A. L. Gaeta, and K. Bergman, "Demonstration of Broadband Wavelength Conversion at 40 Gb/s in Silicon Waveguides," IEEE Photonics Technology Letters **21**, 182-184 (2009).
11. J. Leuthold, D. M. Marom, S. Cabot, J. J. Jaques, R. Ryf, and C. R. Giles, "All-opticalwavelength converter based on a pulse re-formatting optical filter," in *Tech. Dig. OFC'03*, Atlanta, GA, USA, 2003, Paper PD41.
12. J. Leuthold, D. M. Marom, S. Cabot, J. J. Jaques, R. Ryf, and C. R. Giles, "All-optical wavelength conversion using a pulse reformatting optical filter," Journal of Lightwave Technology **22**, 186-192 (2004).
13. M. L. Nielsen, B. Lavigne, and B. Dagens, "Polarity-preserving SOA-based wavelength conversion at 40 Gbit/s using bandpass filtering," Electronics Letters **39**, 1334-1335 (2003).
14. Y. Liu, E. Tangdiongga, Z. Li, S. X. Zhang, H. de Waardt, G. D. Khoe, and H. J. S. Dorren, "Error-free all-optical wavelength conversion at 160 Gb/s using a semiconductor optical amplifier and an optical bandpass filter," Journal of Lightwave Technology **24**, 230-236 (2006).
15. Y. Liu, E. Tangdiongga, Z. Li, H. de Waardt, A. M. J. Koonen, G. D. Khoe, X. W. Shu, I. Bennion, and H. J. S. Dorren, "Errior-free 320-Gb/s all-omtical wavelength conversion using a single semiconductor optical amplifier," Journal of Lightwave Technology **25**, 103-108 (2007).

16. S. N. Fu, J. J. Dong, P. Shum, L. R. Zhang, X. L. Zhang, and D. X. Huang, "Experimental demonstration of both inverted and non-inverted wavelength conversion based on transient cross phase modulation of SOA," Optics Express **14**, 7587-7593 (2006).
17. M. L. Nielsen and J. Mork, "Increasing the modulation bandwidth of semiconductor-optical-amplifier-based switches by using optical filtering," Journal of the Optical Society of America B-Optical Physics **21**, 1606-1619 (2004).
18. V. G. Ta'eed, M. D. Pelusi, B. J. Eggleton, D. Y. Choi, S. Madden, D. Bulla, and B. Luther-Davies, "Broadband wavelength conversion at 40 Gb/s using long serpentine As2S3 planar waveguides," Optics Express **15**, 15047-15052 (2007).
19. M. Lipson, "Silicon photonics: the optical spice rack," Electronics Letters, 8-10 (2009).
20. R. M. Osgood, N. C. Panoiu, J. I. Dadap, X. Liu, X. Chen, I. W. Hsieh, E. Dulkeith, W. M. J. Green, and Y. A. Vlasov, "Engineering nonlinearities in nanoscale optical systems: physics and applications in dispersion-engineered silicon nanophotonic wires," Advances in Optics and Photonics **1**, 162-235 (2009).
21. A. D. Bristow, N. Rotenberg, and H. M. van Driel, "Two-photon absorption and Kerr coefficients of silicon for 850-2200 nm," Applied Physics Letters **90**, 191104-191106 (2007).
22. O. Boyraz, P. Koonath, V. Raghunathan, and B. Jalali, "All optical switching and continuum generation in silicon waveguides," Optics Express **12**, 4094-4102 (2004).

23. X. G. Chen, N. C. Panoiu, and R. M. Osgood, "Theory of Raman-mediated pulsed amplification in silicon-wire waveguides," IEEE Journal of Quantum Electronics **42**, 160-170 (2006).

24. J. van Campenhout, W. M. J. Green, X. P. Liu, S. Assefa, R. M. Osgood, and Y. A. Vlasov, "Silicon-nitride surface passivation of submicrometer silicon waveguides for low-power optical switches," Optics Letters **34**, 1534-1536 (2009).

25. Q. F. Xu, V. R. Almeida, and M. Lipson, "Time-resolved study of Raman gain in highly confined silicon-on-insulator waveguides," Optics Express **12**, 4437-4442 (2004).

26. M. A. Foster, A. C. Turner, M. Lipson, and A. L. Gaeta, "Nonlinear optics in photonic nanowires," Optics Express **16**, 1300-1320 (2008).

27. J. B. Driscoll, W. Astar, X. Liu, J. I. Dadap, W. M. J. Green, Y. A. Vlasov, G. M. Carter, and R. M. Osgood, "All-Optical Wavelength Conversion of 10 Gb/s RZ-OOK Data in a Silicon Nanowire via Cross-Phase Modulation: Experiment and Theoretical Investigation," IEEE Journal of Selected Topics in Quantum Electronics **16**, 1448-1459 (2010).

28. E. Dulkeith, Y. A. Vlasov, X. G. Chen, N. C. Panoiu, and R. M. Osgood, "Self-phase-modulation in submicron silicon-on-insulator photonic wires," Optics Express **14**, 5524-5534 (2006).

29. P. J. Winzer, M. Pfennigbauer, M. M. Strasser, and W. R. Leeb, "Optimum filter bandwidths for optically preamplified NRZ receivers," Journal of Lightwave Technology **19**, 1263-1273 (2001).

30. P. J. Winzer and A. Kalmar, "Sensitivity enhancement of optical receivers by impulsive coding," Journal of Lightwave Technology **17**, 171-177 (1999).

Chapter 5

Conformal dielectric overlayers for engineering dispersion and effective nonlinearity

5.1 Introduction

Recently, nonlinear parametric optical processes in high-confinement SOI nanophotonic wire waveguides have attracted much interest due to the large third-order susceptibility $\chi^{(3)}$ of silicon as well as compatibility with CMOS integration. These advantages make possible a variety of chip-based nonlinear optical applications, with examples including parametric amplification by four-wave mixing (FWM) [1], wavelength conversion [2-4], all-optical regeneration [5, 6], supercontinuum generation [7, 8], and cross-phase modulation (XPM) [9]. In FWM, two pump photons are converted into a signal and idler photons such that $2\omega_p = \omega_s + \omega_i$. Achieving phase matching for efficient FWM requires that the power-dependent Kerr nonlinear phase shift be compensated by the linear phase mismatch between the pump, signal and idler waves, $\Delta k = 2\gamma P_p - \Delta k_l = 0$, where γ is the effective nonlinearity parameter, P_p is the pump power, and $\Delta k_l = 2\beta_p - \beta_s - \beta_i$ is the phase mismatch between pump, signal and idler waves as discussed in Section 2.2.2 of Chapter 2. The latter requirement demands that the nanophotonic wires exhibit anomalous group velocity dispersion (GVD), with a GVD parameter D_λ > 0 [1, 10]. While the material dispersion of silicon is normal for wavelengths near 1.55 μm [11], significant anomalous geometrical dispersion arises from strong optical confinement in nanophotonic wires, and produces large net anomalous

GVD (D_λ ~ 4000 ps/nm-km for air clad wires with cross-section 525 nm × 226 nm [12]). However, such a large GVD (~ 200× larger than that of single-mode fiber) dramatically reduces the bandwidth for the parametric conversion or amplification [2]. Previous studies have shown that near-zero anomalous GVD can be engineered via control of the geometrical dispersion, through 1) oxidation of cylindrical silicon core waveguide [13] or 2) by modifying the dimensions and/or aspect ratio of the rectangular silicon waveguide core [12, 14, 15]. However the first approach introduces major constraints for a CMOS-compatible process, while the second approach requires increasing the waveguide's cross-sectional area, which consequently results in a penalty to the effective nonlinearity. In this chapter, an alternative approach to engineering silicon nanophotonic wire dispersion using thin silicon nitride (Si_3N_4) overlayers is reported. This technique offers the advantages of increased optical confinement and improved effective nonlinearity.

5.2 Overlayer dispersion engineering approach

The inset of Figure 5-1 illustrates the nanophotonic wire geometry under consideration, having a Si core of width *w* and height *h*, lying on a buried oxide (BOX) layer. The silicon core is covered with a conformal Si_3N_4 overlayer of thickness *t* and then capped with a thick oxide layer. Our method is conceptually similar to that used in the design of dispersion shifted fiber (DSF) [16], where the thickness and refractive index of thin cladding layers surrounding the fiber core are manipulated to control the balance of geometrical and material dispersion, producing the desired net dispersion characteristics.

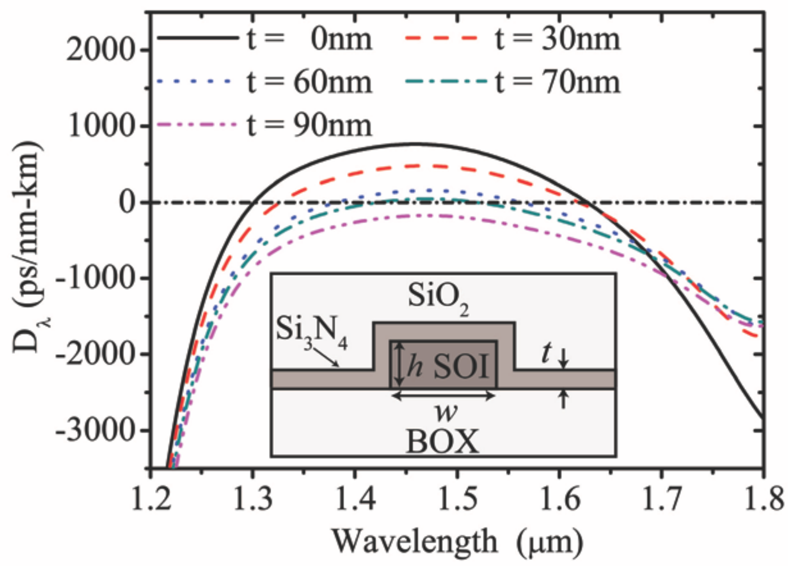

Figure 5-1 GVD for the fundamental quasi-TE mode of a silicon nanophotonic wire having dimensions *w* = 450 nm, *h* = 220 nm, for different Si_3N_4 overlayer thicknesses. Inset: Si nanophotonic wire cross section.

The waveguide dispersion is computed following the method described in Section 2.1 of Chapter 2. This work focuses on the dispersion characteristics of fundamental quasi-TE mode. Figure 5-1 plots the calculated GVD vs. wavelength for a 450 nm × 220 nm wire, for several Si_3N_4 overlayer thicknesses. With oxide cladding only (t = 0 nm, no Si_3N_4 coating), the GVD at λ = 1.55 μm has a value of 532 ps/nm-km. However, using a conformal Si_3N_4 overlayer of 60 nm, this dispersion is significantly reduced to 38 ps/nm-km, a value sufficiently low to achieve efficient phase-matched wavelength conversion or FWM parametric gain at low pump power [1, 2, 17]. For a Si_3N_4 overlayer of 70 nm or thicker, normal dispersion prevails for wavelengths near 1.55 μm. Furthermore, Figure 5-1 illustrates that the use of thin Si_3N_4 overlayers can also reduce fourth-order dispersion, producing wide spectral regions with small GVD curvature, and facilitating broadband phase matching [2, 17]. Finally, for an overlayer thickness $\leq$ 70 nm, two wavelengths with zero-GVD (ZGVD) coexist within the spectrum. The spectral separation between these two points decreases nearly monotonically with Si_3N_4 overlayer thickness, potentially offering an approach to control the dispersion at two widely separated wavelengths in a nonlinear process. For example, in the case of stimulated Raman scattering (SRS) [18] or cascaded SRS [19] using ultra-short pulses, undesired pulse broadening for both pump and Raman signals can be minimized by positioning each at a ZGVD point.

By altering the nanophotonic wire width and/or Si_3N_4 overlayer thickness, the ZGVD points can be shifted. Figure 5-2 illustrates this with a contour plot of the short-wavelength ZGVD point versus the wire width and Si_3N_4 thickness, for a wire height of h = 220 nm. The ZGVD point shifts to longer wavelengths as the width becomes larger and/or the Si_3N_4 overlayer becomes thicker, indicating that these two parameters may be used as independent degrees of freedom in tailoring the spectral dispersion of a silicon nanophotonic wire. It is worthwhile to note that Si_3N_4 overlayers are equally effective for engineering dispersion even when the thick upper oxide is replaced by air cladding. The possible residual stress in Si_3N_4 conformal films and fabrication dimension errors of SOI cores merely cause the required thickness of Si_3N_4 to deviate slightly from the value as designed. However, these issues can be addressed by the fact that this configuration permits tuning of the dispersion characteristics in a step-wise fashion by sequential deposition of one or more conformal layers. Furthermore, the overlayer approach can be generalized to other high-index dielectric materials such as chalcogenide glasses [20], where the nonlinear optical characteristics of the overlayer may be chosen to enhance the nonlinearity of the Si core. Finally, the conformal overlayer can also serve as a graded-index cladding, which will reduce propagation losses in comparison to the cases of air or oxide claddings [21].

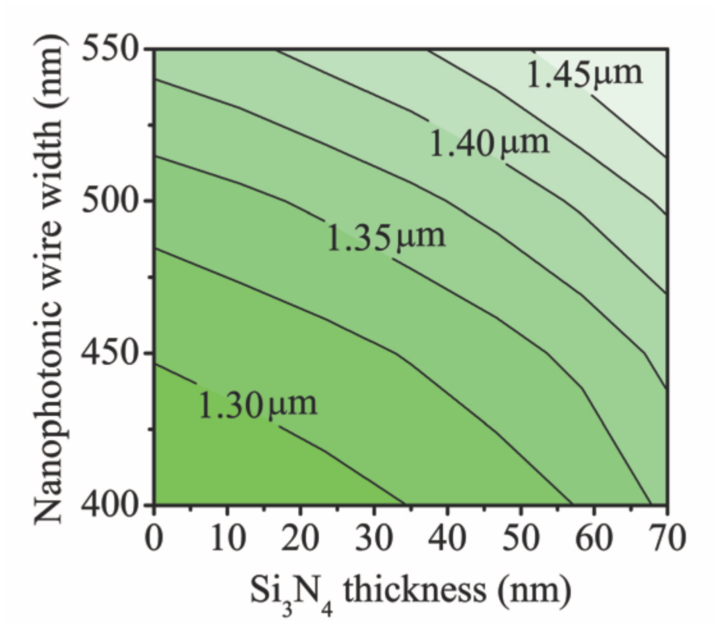

Figure 5-2 Short-wavelength ZGVD contours for the fundamental quasi-TE mode versus Si_3N_4 overlayer thickness and nanophotonic wire width. The wire height is 220 nm.

5.3 Waveguide effective nonlinearity

In addition to phase matching, another factor contributing to the waveguide parametric efficiency is the effective nonlinearity parameter γ. The parameter γ is derived using the expression $\gamma = 3\omega \,\mathrm{Re}(\Gamma)/(4\varepsilon_0 A_0 v_g^2)$, as described in Section 2.2 of Chapter 2. The nonlinear susceptibility of silicon dominates any contributions from the Si_3N_4 overlayer or surrounding oxide cladding. Using the calculated modal profiles for the fundamental quasi-TE mode, the spectral dependence of γ for various Si_3N_4 overlayer thicknesses is obtained and plotted in Figure 5-3(a).

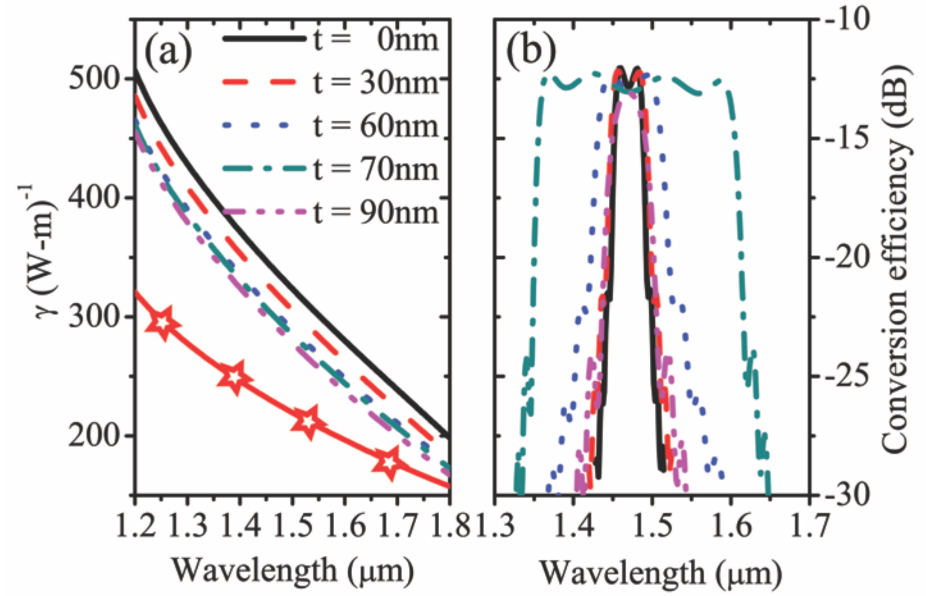

Figure 5-3 (a) Effective nonlinearity for the fundamental quasi-TE mode of a nanophotonic wire with w = 450 nm, h = 220 nm, for different Si_3N_4 overlayer thicknesses. The curve marked with stars is for a large-core oxide-clad waveguide with w = 600 nm, h = 300 nm. (b) Simulated overlayer thickness-dependent parametric wavelength conversion efficiency for 2 cm-long nanophotonic wire pumped at λ = 1.47 μm with power 0.4 W.

The effective nonlinearity has a value of ~ 10^2 $W^{-1}m^{-1}$, which is ~ 10^5 larger than the typical value in standard single-mode fiber. For a given Si_3N_4 thickness, γ decreases monotonically at longer wavelengths due to decreasing modal confinement within the Si core. Furthermore, for a given wavelength, increasing the Si_3N_4 thickness results in a small reduction of γ which saturates for t ~ 90 nm. As the thickness of the Si_3N_4 overlayer increases, the total cross-sectional area of the “effective” waveguide core (i.e. Si wire plus Si_3N_4 film) becomes larger, permitting the guided mode to spread out of the Si core where the optical nonlinearity originates. However, since the refractive index contrast between Si and Si_3N_4 is still very large, the quasi-TE mode nevertheless remains strongly concentrated within the Si nanophotonic wire. In fact, for the 60 nm Si_3N_4 overlayer required to engineer near-zero anomalous GVD at λ = 1.55 μm, the effective nonlinearity (γ ~ 270 $W^{-1}m^{-1}$) is reduced by less than 15% in comparison to that for no Si_3N_4 overlayer (t = 0 nm). Note it is possible to achieve higher nonlinearites via geometrical cross section change by using the second dispersion point; however, this approach necessitates a much smaller cross section resulting in higher losses and a smaller near zero-GVD bandwidth. Figure 5-3(a) also shows the effective nonlinearity of a large-Si-core oxide-clad nanophotonic wire (w = 600 nm, h = 300 nm, no Si_3N_4 overlayer) which has been used in several recent demonstrations of Si-based nonlinear devices [1, 5, 6].

While this geometry achieves similar near-zero anomalous GVD by increasing the Si core area [14], the trade-off is a clear penalty on the effective nonlinearity, being ~ 25% lower in comparison with that of the waveguides having a smaller Si core in conjunction with Si_3N_4 overlayers. The ability to maintain a higher effective nonlinearity while simultaneously allowing sensitive control of GVD indicates that the overlayer dispersion engineering method is well-suited to enabling comparable on-chip nonlinear devices using shorter, more compact waveguides and lower pump power levels.

The effectiveness of using thin film overlayers for dispersion engineering can be further illustrated by considering the example of parametric wavelength conversion by

FWM. The cw conversion efficiency is calculated using the Si_3N_4 overlayer-thickness-dependent dispersion and effective nonlinearity characteristics shown in Figure 5-1 and Figure 5-3(a), respectively. The calculation follows the model described in Section 2.2.2 of Chapter 2 where all the terms containing time derivative are set to zero in this cw case. The calculation includes a propagation loss of 1.5 dB/cm, two-photon absorption (TPA) via a waveguide effective TPA coefficient $\beta_{TPA} = 3\omega\,\mathrm{Im}(\Gamma)/(2\varepsilon_0 v_g^2)$, and TPA-induced free carrier absorption (FCA) with a carrier lifetime of 1 ns [22, 23]. The pump wavelength is positioned near the zero third-order dispersion point at λ ~ 1.47 μm, where it is found numerically that the conversion bandwidth is maximized. The results are shown in Figure 5-3(b) for a 2 cm long waveguide and a pump power of 0.4 W. The peak conversion efficiency drops monotonically with increasing overlayer thickness, owing to the corresponding reduction in γ. Despite this decrease, the conversion bandwidth increases with overlayer thickness as long as the GVD at the pump wavelength remains anomalous, i.e. for a Si_3N_4 thickness ≤ 70 nm. For a strictly oxide cladding (t = 0 nm), the bandwidth of conversion efficiency > -15 dB is restricted to ~ 40 nm, while using a 70 nm thick Si_3N_4 overlayer to achieve near-zero anomalous GVD significantly broadens the bandwidth to approximately 250 nm. However, once the overlayer thickness becomes > 70 nm, the bandwidth narrows due to the onset of normal GVD, as illustrated in Figure 5-1.

5.4 Conclusion

To summarize, a versatile new approach using a dielectric overlayer surrounding the Si core for controlling Si nanophotonic wire dispersion is analyzed in this chapter. In comparison with the previously studied method of increasing the cross-sectional area of the Si core, the overlayer-engineered wires possess a substantially higher effective nonlinearity. Engineering broadband phase matching while simultaneously maintaining high nonlinearity makes this approach ideal for the design of highly compact, low-power Si nonlinear devices.

Reference

1. M. A. Foster, A. C. Turner, J. E. Sharping, B. S. Schmidt, M. Lipson, and A. L. Gaeta, "Broad-band optical parametric gain on a silicon photonic chip," Nature **441**, 960-963 (2006).
2. M. A. Foster, A. C. Turner, R. Salem, M. Lipson, and A. L. Gaeta, "Broad-band continuous-wave parametric wavelength conversion in silicon nanowaveguides," Optics Express **15**, 12949-12958 (2007).
3. Y. H. Kuo, H. S. Rong, V. Sih, S. B. Xu, M. Paniccia, and O. Cohen, "Demonstration of wavelength conversion at 40 Gb/s data rate in silicon waveguides," Optics Express **14**, 11721-11726 (2006).
4. H. S. Rong, Y. H. Kuo, A. S. Liu, M. Paniccia, and O. Cohen, "High efficiency wavelength conversion of 10Gb/s data in silicon waveguides," Optics Express **14**, 1182-1188 (2006).
5. R. Salem, M. A. Foster, A. C. Turner, D. F. Geraghty, M. Lipson, and A. L. Gaeta, "All-optical regeneration on a silicon chip," Optics Express **15**, 7802-7809 (2007).

6. R. Salem, M. A. Foster, A. C. Turner, D. F. Geraghty, M. Lipson, and A. L. Gaeta, "Signal regeneration using low-power four-wave mixing on silicon chip," Nature Photonics **2**, 35-38 (2008).

7. I. W. Hsieh, X. G. Chen, X. P. Liu, J. I. Dadap, N. C. Panoiu, C. Y. Chou, F. N. Xia, W. M. Green, Y. A. Vlasov, and R. M. Osgood, "Supercontinuum generation in silicon photonic wires," Optics Express **15**, 15242-15249 (2007).

8. L. H. Yin, Q. Lin, and G. P. Agrawal, "Soliton fission and supercontinuum generation in silicon waveguides," Optics Letters **32**, 391-393 (2007).

9. I. W. Hsieh, X. G. Chen, J. I. Dadap, N. C. Panoiu, R. M. Osgood, S. J. McNab, and Y. A. Vlasov, "Cross-phase modulation-induced spectral and temporal effects on co-propagating femtosecond pulses in silicon photonic wires," Optics Express **15**, 1135-1146 (2007).

10. G. P. Agrawal, *Nonlinear Fiber Optics* (Academic, San Diego, 2001).

11. E. D. Palik, *Handbook of Optical Constants of Solid* (Academic, San Diego, 1998).

12. E. Dulkeith, F. N. Xia, L. Schares, W. M. J. Green, and Y. A. Vlasov, "Group index and group velocity dispersion in silicon-on-insulator photonic wires," Optics Express **14**, 3853-3863 (2006).

13. J. Y. Lou, L. M. Tong, and Z. Z. Ye, "Dispersion shifts in optical nanowires with thin dielectric coatings," Optics Express **14**, 6993-6998 (2006).

14. A. C. Turner, C. Manolatou, B. S. Schmidt, M. Lipson, M. A. Foster, J. E. Sharping, and A. L. Gaeta, "Tailored anomalous group-velocity dispersion in silicon channel waveguides," Optics Express **14**, 4357-4362 (2006).

15. L. H. Yin, Q. Lin, and G. P. Agrawal, "Dispersion tailoring and soliton propagation in silicon waveguides," Optics Letters **31**, 1295-1297 (2006).

16. I. P. Kaminow and T. L. Koch, *Optical Fiber Telecommunications IIIA* (Academic, San Diego, 1997).

17. Q. Lin, J. D. Zhang, P. M. Fauchet, and G. P. Agrawal, "Ultrabroadband parametric generation and wavelength conversion in silicon waveguides," Optics Express **14**, 4786-4799 (2006).

18. O. Boyraz and B. Jalali, "Demonstration of a silicon Raman laser," Optics Express **12**, 5269-5273 (2004).

19. H. S. Rong, S. B. Xu, O. Cohen, O. Raday, M. Lee, V. Sih, and M. Paniccia, "A cascaded silicon Raman laser," Nature Photonics **2**, 170-174 (2008).

20. M. R. E. Lamont, C. M. de Sterke, and B. J. Eggleton, "Dispersion engineering of highly nonlinear As2S3 waveguides for parametric gain and wavelength conversion," Optics Express **15**, 9458-9463 (2007).

21. J. J. Hu, N. N. Feng, N. Carlie, L. Petit, J. F. Wang, A. Agarwal, K. Richardson, and L. Kimerling, "Low-loss high-index-contrast planar waveguides with graded-index cladding layers," Optics Express **15**, 14566-14572 (2007).

22. Q. F. Xu, B. Schmidt, S. Pradhan, and M. Lipson, "Micrometre-scale silicon electro-optic modulator," Nature **435**, 325-327 (2005).

23. J. van Campenhout, W. M. J. Green, X. P. Liu, S. Assefa, R. M. Osgood, and Y. A. Vlasov, "Silicon-nitride surface passivation of submicrometer silicon waveguides for low-power optical switches," Optics Letters **34**, 1534-1536 (2009).

Chapter 6

Mid-infrared optical parametric amplifier using silicon nanophotonic wire

6.1 Introduction

All-optical signal processing is envisioned as an approach to dramatically decrease power consumption and speed up performance of next-generation optical telecommunications networks [1-3]. Nonlinear optical effects, such as four-wave mixing (FWM) and parametric gain, have long been explored to realize all-optical functions in glass fibers [4]. An alternative approach is to employ nanoscale engineering of silicon waveguides to enhance the optical nonlinearities by up to five orders of magnitude [5], enabling integrated chip-scale all-optical signal processing. FWM within silicon nanophotonic waveguides has recently been used to demonstrate several telecom-band (λ ~1550 nm) all-optical functions, including wavelength conversion [6-9], signal regeneration [10], and tunable optical delay [11]. Despite these important advances, strong two-photon absorption [12] (TPA) of the telecom-band pump has been a fundamental and unavoidable obstacle, limiting parametric gain to values on the order of a few dB [13].

This chapter describes a demonstration of a silicon nanophotonic optical parametric amplifier exhibiting gain as large as 25.4 dB, by operating the pump in the mid-IR near one-half the band-gap energy (E ~ 0.55 eV, λ ~ 2200 nm), at which parasitic TPA-related absorption vanishes [12, 14]. This gain is high enough to compensate all insertion losses, resulting in 13 dB net off-chip amplification. Furthermore, dispersion engineering [15] dramatically increases the gain bandwidth to more than 220 nm, all realized using an ultra-compact 4 mm silicon chip. Beyond its significant relevance to all-optical signal processing, the broadband parametric gain also facilitates the simultaneous generation of multiple on-chip mid-IR sources through cascaded FWM, covering a 500 nm spectral range. Together, these results provide a foundation for the construction of silicon-based room-temperature mid-IR light sources including tunable chip-scale parametric oscillators [16-18], optical frequency combs [19], and supercontinuum generators [20]. In this manner, silicon nanophotonic technology may be extended to an entirely new class of mid-IR applications [21, 22] including biochemical detection, environmental monitoring, and free-space communication, in which an integrated on-chip platform can be of great benefit.

6.2 Waveguide properties

In order to achieve large, broadband nonlinear parametric gain in silicon, the FWM process [23] relies upon precise phase matching between the co-propagating pump, signal, and idler waves, as well as the presence of a strong nonlinear interaction, described by the effective nonlinearity parameter γ. In addition, the intrinsic nonlinear figure of merit of silicon FOM = $n_2/(\beta_{TPA}\cdot\lambda)$, where n_2 is the intensity-dependent refractive index and β_{TPA} is the TPA coefficient, should be as large as possible. While a large TPA coefficient restricts FOM to values less than 0.4 near $\lambda = 1550$ nm, at mid-IR wavelengths approaching silicon's TPA threshold at $\lambda \sim 2200$ nm, FOM can increase as much as ten-fold to FOM > 4. Therefore, the mid-IR is a highly promising spectrum for realizing chip-scale silicon nanophotonic all-optical devices whose performance is no longer restricted by parasitic nonlinear absorption.

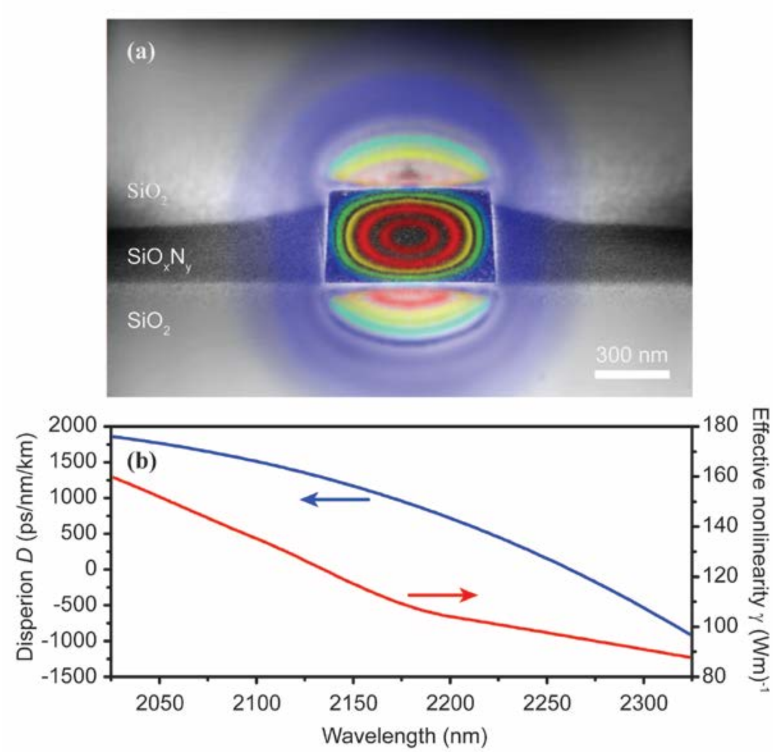

Figure 6-1 Engineered silicon nanophotonic waveguide characteristics. (a) SEM cross-section of the 700 nm × 425 nm silicon waveguide. The colour-map illustrates the E_y component of the fundamental quasi-TM mode at λ = 2200 nm. (b) Simulated dispersion coefficient D (blue curve) and effective nonlinearity parameter γ (red curve).

The essential dispersion and nonlinearity characteristics for a silicon nanophotonic waveguide operating in the mid-IR were engineered through a comprehensive multi-parameter design space study, encompassing the nanoscale dimensions of the silicon core, the refractive index of the cladding, and the waveguide mode polarization as discussed in Chapter 5. The resulting geometry ultimately selected for fabrication is shown in the

SEM cross-section image in Figure 6-1(a). The silicon waveguide core has dimensions of 700 nm × 425 nm, and is designed to operate in the fundamental quasi-TM mode near λ = 2200 nm, as illustrated by the overlaid mode field profile. The nanoscale-engineered optical structure is precisely controlled using a combination of silicon epitaxy, deep-UV lithography, reactive ion etching, and dielectric deposition, within an advanced CMOS fabrication facility (see Section 2.1 in Chapter 2).

The calculated dispersion coefficient D and effective nonlinearity parameter γ for this specific silicon nanophotonic waveguide configuration are plotted in Figure 6-1(b), illustrating the mid-IR spectral dependence near silicon's TPA threshold. The dispersion is designed to be zero at a wavelength of λ = 2260 nm. The pump wavelength is chosen at λ = 2170 nm such that the nanophotonic waveguide possesses anomalous dispersion conditions with D = 1000 ps/nm/km, as required for broadband phase matching [23]. Strong optical confinement of the quasi-TM mode to the ~ 0.3 um^2 silicon core results in a large effective nonlinearity of $\gamma = 110\ (\mathrm{W \cdot m})^{-1}$ at λ = 2170 nm, a value more than ten times larger than that of planar chalcogenide glass waveguides [24], and four orders of magnitude larger than that of highly nonlinear optical fiber [4, 25].

Silicon nanophotonic waveguide propagation losses near λ = 2200 nm were measured using the cutback method, by measuring transmission of broadband amplified spontaneous emission (ASE) from the tunable mid-IR cw laser (Photonics Innovations SFTL). The propagation loss varied from approximately 4 dB/cm at 2030 nm, to 10 dB/cm at 2500 nm. Subtracting the linear propagation loss from the total measured fiber-to-fiber insertion loss, a coupling loss from lensed fiber into the silicon nanophotonic waveguide of approximately 6.5 +/- 1 dB/facet was estimated.

6.3 Experiment setup and parametric gain profile

As illustrated in Figure 6-2 by the schematic of experiment setup, the mid-IR nonlinear characteristics of a 4 mm-long silicon nanophotonic waveguide are studied by simultaneously injecting picosecond pump pulses centered at λ = 2170 nm along with a

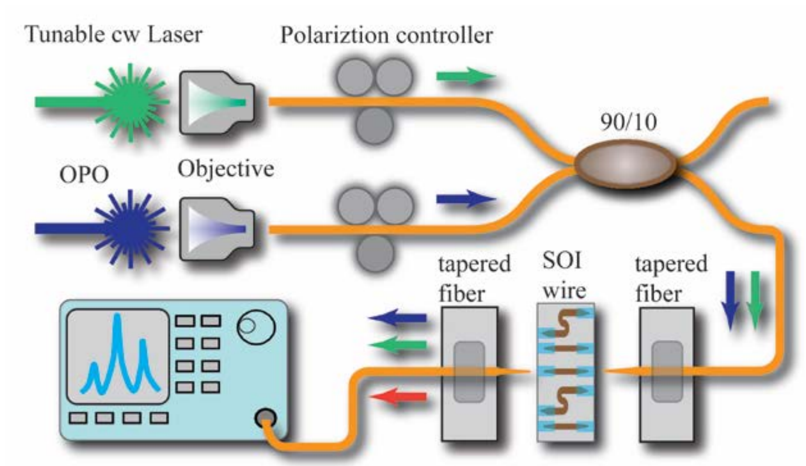

Figure 6-2 Schematic of measurement setup for FWM parametric wavelength conversion and parametric amplification. Pump pulses are coupled from Coherent Mira-OPO with FWHM ~ 2 ps and repetition rate = 76 MHz. Signal is coupled from Photonics Innovations SFTL mid-IR tunable cw laser. They are aligned to excite quasi-TM mode, multiplexed with a fused fiber coupler and coupled into/out-of 4-mm long silicon nanophotonic wire via edge coupling with lensed tapered fibers.

cw tunable mid-IR laser signal, and observing the resulting FWM at the waveguide output. The peak coupled pump power at the waveguide input is P_p ~ 27.9 W, while the input signal power P_{sig} is kept below 0.45 mW. For each spectrum shown in Figure 6-3(a), two photons from the high-intensity pulsed pump mix with a single photon from the tunable cw signal to generate a wavelength-converted idler photon, at a wavelength dictated by energy conservation [23]. The FWM process also produces an additional photon at the signal wavelength, which can ultimately contribute to signal amplification. Due to the pulsed nature of the pump, the generated idler and amplified signal also occur as short pulses.

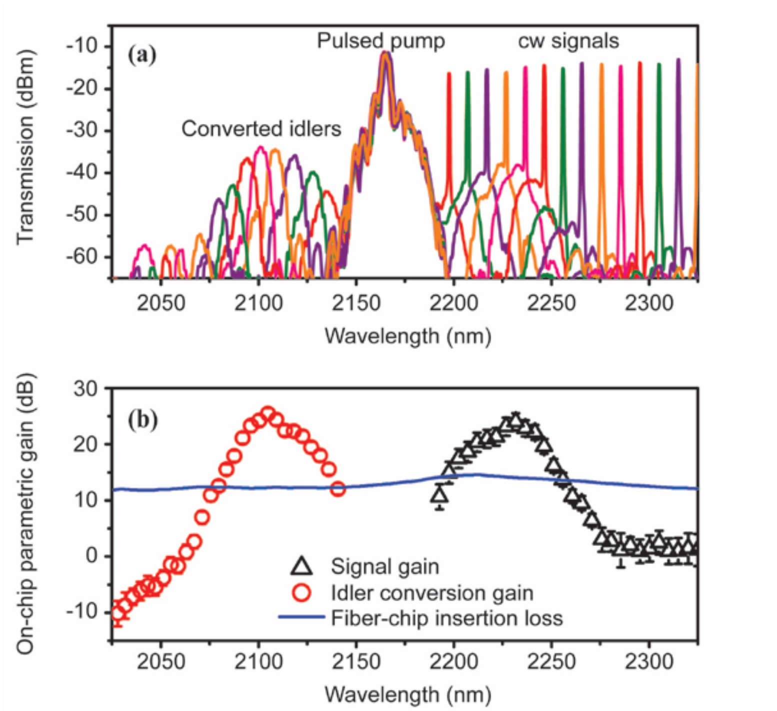

Figure 6-3 Mid-infrared FWM experiments and broadband on-chip optical parametric amplification**.** (a) Series of FWM spectra taken at the output of the 4-mm-long waveguide. (b) On-chip parametric signal gain (black triangles) and idler conversion gain (red circles), with bandwidth of ~ 220 nm and peak values > 25 dB. Net off-chip gain results where amplification exceeds fiber-chip insertion losses (blue line), with a maximum value of ~ 13 dB.

The FWM spectra in Figure 6-3(a) are analyzed to extract the on-chip parametric signal gain and idler conversion gain values plotted in Figure 6-3(b) using the numerical approach as followings. The peak power of the converted idler pulse at the output of the silicon waveguide, P_{idler_out}, was derived from the measured FWM spectra shown in Figure 6-3(a), according to $P_{idler\_out} = F\left(\int P_{idler\_avg}(\lambda)d\lambda\right)$. In order to convert the time-averaged idler power P_{idler_avg} measured by the OSA into peak power, the spectrally integrated power was weighted by the duty cycle factor F = 1/(76 MHz·2 ps), due to the pulsed nature of the experiment. A similar procedure was applied to find the pulsed signal output power P_{signal_out}. A 2 nm wide band-stop filter was first numerically applied to the time-averaged signal spectrum, in order to exclude the power remaining in the narrowband cw tone. The peak signal power was then computed according to $P_{signal\_out} = F\left(\int P_{signal\_filtered\_avg}(\lambda)d\lambda\right)$. Finally, to find the cw signal power at the waveguide input P_{signal_in}, the output cw signal power was measured (with the pump off) and corrected to account for total propagation losses of α dB incurred through the 4 mm long device, $P_{signal\_in} = 10^{\alpha/10}\left(\int P_{signal\_out\_pump\_off}(\lambda)d\lambda\right)$. Using the above quantities, the on-chip idler conversion gain η was then defined as the ratio of peak idler power and input cw signal power, $\eta = P_{idler\_out} / P_{signal\_in}$. Accordingly, on-chip signal gain was given by $G = P_{signal\_out} / P_{signal\_in}$. The error bars in the on-chip parametric gain data were calculated according to uncertainty in the measured facet coupling losses, as well as to account for the contribution of the OSA noise floor accumulated when integrating the signal/idler power at the waveguide output.

The experimental data reveals that the engineered silicon nanophotonic waveguide successfully functions as a mid-IR optical parametric amplifier (OPA), with very large maximum signal and idler gain values of 24 dB and 25.4 dB, respectively. Moreover, the on-chip parametric gain is significant enough to overcome substantial fiber-chip coupling losses (blue curve), demonstrating net off-chip gain as large as 10 dB for the signal and 13 dB for the idler. The overall on-chip gain bandwidth spans the range from 2060 nm to 2280 nm, with the two prominent gain peaks coinciding with the envelopes of the pulsed signal and idler spectra in Figure 6-3(a). The maximum parametric gain obtained using our ultra-compact 4 mm device is more than 100 times larger than previously observed in a 17 mm-long silicon waveguide pumped near λ = 1550 nm, where gain has been limited to ~3 dB owing to strong TPA-induced saturation effects [13]. By operating the pump at longer wavelengths in the mid-IR, we have realized a chip-scale silicon nanophotonic OPA which breaks the limits set by TPA nonlinear absorption.

6.4 Parametric amplifier performance characteristics

Additional experiments were carried out with the input signal tuned to the gain peak at λ = 2238 nm, in order to thoroughly characterize the OPA's input-output and gain saturation characteristics. Figure 6-4(a) plots the output peak signal and idler power vs. input signal power, with pump power P_p ~ 27.9 W. The dashed fit lines highlight linear amplification over a dynamic range significantly larger than 30 dB, with signal/idler gain of 23.4 dB/24.7 dB. Figure 6-4(b) plots on-chip signal/idler gain vs. input pump power, with signal power P_{sig} ~ 0.39 mW. The intersection with the dotted line illustrates that on-chip transparency is reached with a pump power near P_p ~ 7.5 W. These pump requirements may be reduced by increasing the waveguide length, or by suitable nanoscale engineering of the waveguide cross-section to increase the effective nonlinearity. Figure 6-4(b) also shows that saturation does not begin until P_p ~ 19 W, at which point signal/idler gain both exceed 20 dB. The measurements reveal that this gain saturation is strongly correlated with self-limiting of the transmitted pump power, as shown by the black squares in Figure 6-4(c). Numerical models described in Section 2.2 of Chapter 2 were used to assess the origin of this self-limiting. It is revealed that a residual TPA coefficient [12] of β_{TPA} = 0.106 cm/GW cannot alone account for the observed saturation at high input pump power (blue dash-dot curve). The significantly reduced value of β_{TPA} at λ = 2170 nm, approximately seven times smaller than at λ = 1550 nm, suggests that higher-order nonlinear absorption dominates under these OPA operating conditions. The red dashed curve in Figure 6-4(c) shows that when a three-photon absorption (3PA) coefficient [26] of γ_{3PA} = 0.025 cm^3/GW^2 is included in the simulation along with TPA, the model accurately predicts the experimental trend. However, even though 3PA is expected to play a role up to λ ~ 3300 nm, the characteristics of the OPA demonstrated here clearly illustrate that nonlinear absorption no longer presents a significant obstacle to obtaining parametric gain large enough for practical applications in all-optical signal processing [1-3].

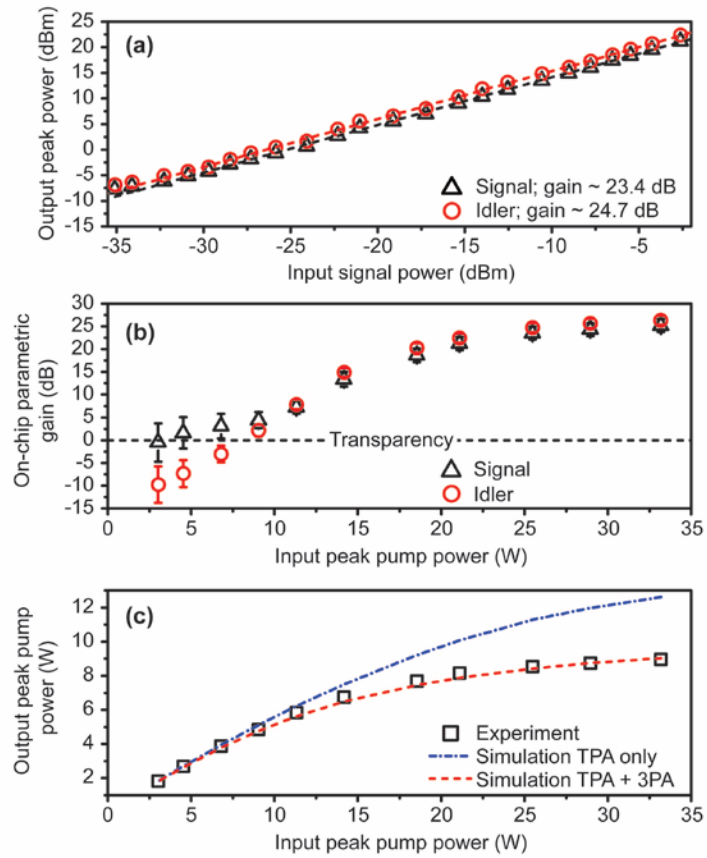

Figure 6-4 Mid-infrared optical parametric amplifier performance characteristics. (a) Output peak signal/idler power versus input signal power at λ = 2238 nm and peak pump power P_p ~ 27.9W. Measurements show a linear amplifier response over a dynamic range > 30 dB. (b) On-chip signal/idler gain versus input peak pump power, input signal power P_{sig} ~ 0.39 mW at λ = 2238 nm. Transparency was reached at P_p ~ 7.5W. (c) Output peak pump power versus input peak pump power. Experimentally measured data points are shown by black squares. The blue dash-dotted and red dashed curves illustrate simulated transmission models accounting for nonlinear loss from TPA only and TPA-plus-3PA, respectively.

6.5 Cascaded four-wave mixing

The large on-chip parametric gain produces amplified picosecond signal and idler pulses having peak power of several hundred milliwatts within the silicon nanophotonic OPA, which can themselves mix with the pump to efficiently generate new wavelengths through cascaded FWM. As shown by the spectrum in Figure 6-5, four orders of cascaded mixing products (numbered peaks 3-9) spanning a spectral bandwidth of 500 nm are observed when the pump is operated at λ = 2180 nm (P_p ~ 21.8 W), and the signal

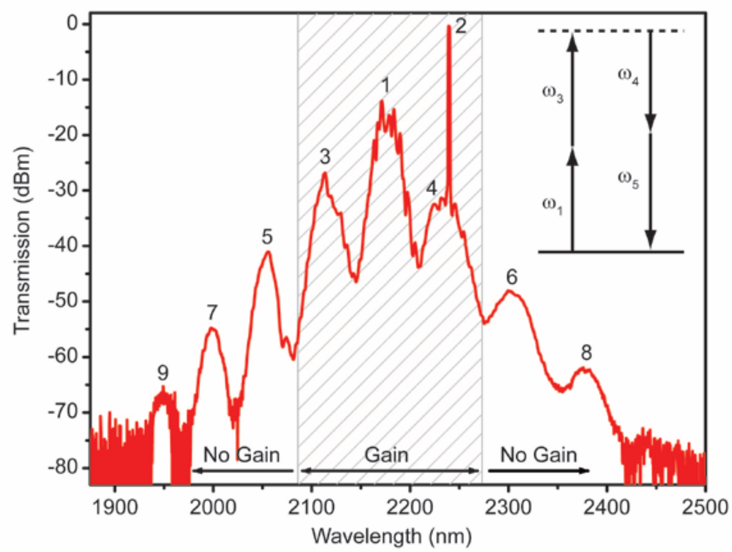

Figure 6-5 Broadband mid-infrared light generation by efficient cascaded FWM. Transmission spectrum illustrating four orders of cascaded mixing products at the silicon nanophotonic OPA output, covering a total bandwidth of 500 nm. The hatched spectral region 2086 nm < λ < 2273 nm experiences on-chip parametric gain, and net on-chip loss is observed outside this region. The inset energy diagram illustrates the dominant FWM process contributing to peak 5.

Table 6-1 Terms contributing to peak 5 of cascaded FWM spectrum shown in Figure 6-5.

Mixing combination (idler: pump 1, pump 2, signal)	Effective pump power (dBm)	Signal power (dBm)	Idler power (dBm)	Conversion efficiency (dB)
5:3,1,4	32.1	23.7	11.2	-12.5
5:3,3,1	25.6	38.5	11.2	-27.3
5:3,1,2	32.1	3.7	11.2	7.5
5:1,1,6	38.5	7.2	11.2	4.0
5:1,4,8	31.1	-6.2	11.2	17.4

All possible degenerate and non-degenerate FWM combinations giving rise to peak 5 in Figure 6-5 are listed in the first column. These combinations are labeled according to the role of each numbered peak (idler: pump 1, pump 2, signal) in the given FWM process. The power associated with each peak in the cascaded FWM spectrum is evaluated in Section 6.3. The effective pump power is given by the geometric average of the power in each pump, $\sqrt{P_{pump1}P_{pump2}}$. The conversion efficiency is defined as the ratio of the idler power and the signal power, P_{idler}/P_{signal}. Mixing terms which appear to suggest a conversion efficiency greater than zero, i.e. idler conversion gain, are ruled out on account of the fact that peak 5 lies well outside the experimentally determined parametric gain bandwidth. Of the remaining mixing combinations, the dominant source for peak 5 is likely to originate from the combination with the largest effective pump power, i.e. combination 5:3,1,4.

is tuned to λ = 2240 nm with an increased input power of P_{sig} ~ 4.4 mW. While on-chip parametric gain under these conditions is restricted to the spectral range 2086 nm < λ < 2273 nm (hatched region), an analysis of the wavelength conversion efficiency at each cascaded mixing peak can assist in further quantifying the OPA characteristics within the regions which experience no gain. For example, the various FWM combinations which can give rise to peak 5 are listed in Table 6-1. As depicted by the inset energy diagram in Figure 6-5, the most sensible dominant term originates from non-degenerate FWM of peaks 1 and 3 as pumps, leading to wavelength conversion of a signal at peak 4 into an idler at peak 5. The conversion efficiency for this mixing term is approximately -12 dB. Applying a similar approach, the conversion efficiencies for peaks 6-9 range from -4 dB to -9 dB, values approximately 8-10 dB larger than those observed in recent silicon mid-IR wavelength conversion experiments [27, 28]. These results illustrate that even far outside the parametric gain bandwidth the present silicon nanophotonic OPA design can be used as a power-efficient generator of broadband mid-IR white light and/or multi-line sources.

6.6 Conclusion

Taken together, the results above provide strong encouragement for a broad extension of the capabilities of the integrated silicon nanophotonic platform into the mid-IR spectrum. Making use of the ultra-compact high-gain OPA demonstrated in this chapter, a direction of immediate interest is the introduction of resonant feedback to develop a silicon-based, low-threshold, highly portable optical parametric oscillator (OPO) [16].

Novel broadband room-temperature light sources such as these would have wide-ranging applications in mid-IR spectroscopy, sensing, and free-space communication [21, 22].

Reference

1. R. S. Tucker, "The role of optics and electronics in high-capacity routers," Journal of Lightwave Technology **24**, 4655-4673 (2006).
2. D. J. Blumenthal, P. R. Prucnal, and J. R. Sauer, "Photonic packet switches - architectures and experimental implementations," Proceedings of the IEEE **82**, 1650-1667 (1994).
3. D. Cotter, R. J. Manning, K. J. Blow, A. D. Ellis, A. E. Kelly, D. Nesset, I. D. Phillips, A. J. Poustie, and D. C. Rogers, "Nonlinear optics for high-speed digital information processing," Science **286**, 1523-1528 (1999).
4. S. Radic and C. J. McKinstrie, "Optical amplification and signal processing in highly nonlinear optical fiber," IEICE Transactions on Electronics **E88C**, 859-869 (2005).
5. J. I. Dadap, N. C. Panoiu, X. G. Chen, I. W. Hsieh, X. P. Liu, C. Y. Chou, E. Dulkeith, S. J. McNab, F. N. Xia, W. M. J. Green, L. Sekaric, Y. A. Vlasov, and R. M. Osgood, "Nonlinear-optical phase modification in dispersion-engineered Si photonic wires," Optics Express **16**, 1280-1299 (2008).
6. R. Claps, V. Raghunathan, D. Dimitropoulos, and B. Jalali, "Anti-Stokes Raman conversion in silicon waveguides," Optics Express **11**, 2862-2872 (2003).
7. R. L. Espinola, J. I. Dadap, J. Osgood, R. M., S. McNab, and Y. A. Vlasov, "C-band wavelength conversion in silicon photonic wire waveguides," Optics Express **13**, 4341-4349 (2005).

8. H. Fukuda, K. Yamada, T. Shoji, M. Takahashi, T. Tsuchizawa, T. Watanabe, J. Takahashi, and S. Itabashi, "Four-wave mixing in silicon wire waveguides," Optics Express **13**, 4629-4637 (2005).

9. H. S. Rong, Y. H. Kuo, A. S. Liu, M. Paniccia, and O. Cohen, "High efficiency wavelength conversion of 10Gb/s data in silicon waveguides," Optics Express **14**, 1182-1188 (2006).

10. R. Salem, M. A. Foster, A. C. Turner, D. F. Geraghty, M. Lipson, and A. L. Gaeta, "Signal regeneration using low-power four-wave mixing on silicon chip," Nature Photonics **2**, 35-38 (2008).

11. Y. T. Dai, X. P. Chen, Y. Okawachi, A. C. Turner-Foster, M. A. Foster, M. Lipson, A. L. Gaeta, and C. Xu, "1 mu s tunable delay using parametric mixing and optical phase conjugation in Si waveguides," Optics Express **17**, 7004-7010 (2009).

12. A. D. Bristow, N. Rotenberg, and H. M. van Driel, "Two-photon absorption and Kerr coefficients of silicon for 850-2200 nm," Applied Physics Letters **90**, 191104-191106 (2007).

13. M. A. Foster, A. C. Turner, J. E. Sharping, B. S. Schmidt, M. Lipson, and A. L. Gaeta, "Broad-band optical parametric gain on a silicon photonic chip," Nature **441**, 960-963 (2006).

14. B. Jalali, V. Raghtmathan, R. Shori, S. Fathpour, D. Dimitropoulos, and O. Stafsudd, "Prospects for silicon mid-IR Raman lasers," IEEE Journal of Selected Topics in Quantum Electronics **12**, 1618-1627 (2006).

15. E. Dulkeith, F. N. Xia, L. Schares, W. M. J. Green, and Y. A. Vlasov, "Group index and group velocity dispersion in silicon-on-insulator photonic wires," Optics Express **14**, 3853-3863 (2006).

16. Q. Lin, T. J. Johnson, R. Perahia, C. P. Michael, and O. J. Painter, "A proposal for highly tunable optical parametric oscillation in silicon micro-resonators," Optics Express **16**, 10596-10610 (2008).

17. J. S. Levy, A. Gondarenko, M. A. Foster, A. C. Turner-Foster, A. L. Gaeta, and M. Lipson, "CMOS-compatible multiple-wavelength oscillator for on-chip optical interconnects," Nature Photonics **4**, 37-40 (2010).

18. L. Razzari, D. Duchesne, M. Ferrera, R. Morandotti, S. Chu, B. E. Little, and D. J. Moss, "CMOS-compatible integrated optical hyper-parametric oscillator," Nature Photonics **4**, 41-45 (2010).

19. P. Del'Haye, A. Schliesser, O. Arcizet, T. Wilken, R. Holzwarth, and T. J. Kippenberg, "Optical frequency comb generation from a monolithic microresonator," Nature **450**, 1214-1217 (2007).

20. I. W. Hsieh, X. G. Chen, X. P. Liu, J. I. Dadap, N. C. Panoiu, C. Y. Chou, F. N. Xia, W. M. Green, Y. A. Vlasov, and R. M. Osgood, "Supercontinuum generation in silicon photonic wires," Optics Express **15**, 15242-15249 (2007).

21. M. Ebrahim-Zadeh and I. T. Sorokina, *Mid-Infrared Coherent Sources and Applications* (Springer, Dordreht, 2007).

22. R. A. Soref, S. J. Emelett, and A. R. Buchwald, "Silicon waveguided components for the long-wave infrared region," Journal of Optics a-Pure and Applied Optics **8**, 840-848 (2006).

23. G. P. Agrawal, *Nonlinear Fiber Optics* (Academic, San Diego, 2001).

24. M. R. E. Lamont, C. M. de Sterke, and B. J. Eggleton, "Dispersion engineering of highly nonlinear As2S3 waveguides for parametric gain and wavelength conversion," Optics Express **15**, 9458-9463 (2007).

25. J. M. C. Boggio, J. R. Windmiller, M. Knutzen, R. Jiang, C. Bres, N. Alic, B. Stossel, K. Rottwitt, and S. Radic, "730-nm optical parametric conversion from near- to short-wave infrared band," Optics Express **16**, 5435-5443 (2008).

26. S. Pearl, N. Rotenberg, and H. M. van Driel, "Three photon absorption in silicon for 2300-3300 nm," Applied Physics Letters **93**, 131102-131104 (2008).

27. A. C. Turner-Foster, M. A. Foster, R. Salem, A. L. Gaeta, and M. Lipson, "Frequency conversion over two-thirds of an octave in silicon nanowaveguides," Optics Express **18**, 1904-1908 (2010).

28. S. Zlatanovic, J. S. Park, S. Moro, J. M. C. Boggio, I. B. Divliansky, N. Alic, S. Mookherjea, and S. Radic, "Mid-infrared wavelength conversion in silicon waveguides using ultracompact telecom-band-derived pump source," Nature Photonics **4**, 561-564 (2010).

Chapter 7

Self-phase modulation and nonlinear loss near silicon's two-photon absorption edge

7.1 Introduction

Research into nonlinear optical propagation within silicon nanophotonic wires has recently attracted much interest due to their strong optical confinement and large third-order nonlinear susceptibility $\chi^{(3)}$ [1-11]. Particularly striking is the size of the effective nonlinearity parameter γ, as it can be up to five orders of magnitude larger than that of conventional silica glass fibers [12, 13]. This large nonlinearity facilitates the observation of many nonlinear processes and enables the realization of a wide variety of advanced chip-scale components for performing ultra-fast all-optical signal processing functions, e.g. wavelength conversion [4, 5, 14], signal regeneration [15, 16], switching [17, 18], and format conversion [19, 20].

Research efforts have recently considered nonlinear optical propagation in wavelength regions outside of the commercial telecommunication bands in order to mitigate the parasitic effects of nonlinear absorption. Within the telecommunication bands, the large $\chi^{(3)}$ of silicon is accompanied by large nonlinear loss, via two-photon absorption (TPA) and the related effects of TPA-induced free-carrier absorption (TPA-FCA). This loss can limit certain all-optical applications requiring a strong pump beam, such as parametric amplification through four-wave mixing (FWM) [4]. However, recent studies have shown that large nonlinear optical gain [21] and broadband wavelength conversion [22, 23] can be obtained with FWM by operating in the mid-infrared (mid-IR) near 2200 nm, corresponding to the wavelength spectrum beyond the onset of TPA.

These recent mid-IR demonstrations make it clear that an important direction for further research is to develop a full understanding of the behavior of the nonlinear refractive index n_2 and the two-photon absorption coefficient β_{TPA}, specifically within the spectral region near and across the TPA edge. Previously, measurements of these quantities have been reported on bulk silicon crystals [24-26] (telecom-band and mid-IR), and Si nanophotonic wires [1, 8, 11] (telecom-band). However, only limited studies have been made of mid-IR pulse propagation in SOI waveguides [21, 22, 27]. In this chapter, characteristics of mid-IR picosecond pulse propagation through silicon nanophotonic wires are studied, and the observed self-phase modulation (SPM) and nonlinear transmission are specially analyzed. In so doing, valuable insights into the variation of the nonlinear coefficients n_2 and β_{TPA} across the mid-IR TPA threshold near 2200 nm are obtained. In addition and in contrast to prior studies of mid-IR four-wave mixing effects in Si nanophotonic wires [21-23], I seek to avoid additional contributions from nonlinear Kerr-effect phenomena such as soliton generation [28, 29], self-steepening [30], and modulation instability [31], and thus use Si wires designed to have normal dispersion over the spectrum of interest

7.2 Waveguide dispersion and effective nonlinearity

This experiment employs a strip Si nanophotonic wire (Figure 7-1(c) inset) with height h = 220 nm, width w = 600 nm and length L = 4 mm, patterned on a 2 μm-thick buried-oxide (BOX) layer. The waveguide is planarized with SiO_2, and then clad with a

60 nm-thick silicon nitride (Si_3N_4) film and a thick SiO_2 top layer. Optical coupling into and out-of the Si nanophotonic wire is via a SiO_xN_y mode-converter [32, 33]. All optical structures are fabricated on a standard CMOS line at the IBM T. J. Watson Research Center. Si nanophotonic wires with similar dimensions have been used extensively for nonlinear optical-signal-processing applications in the telecommunication band due to their large effective nonlinearity and strong modal confinement [4, 5, 9, 10, 14-20].

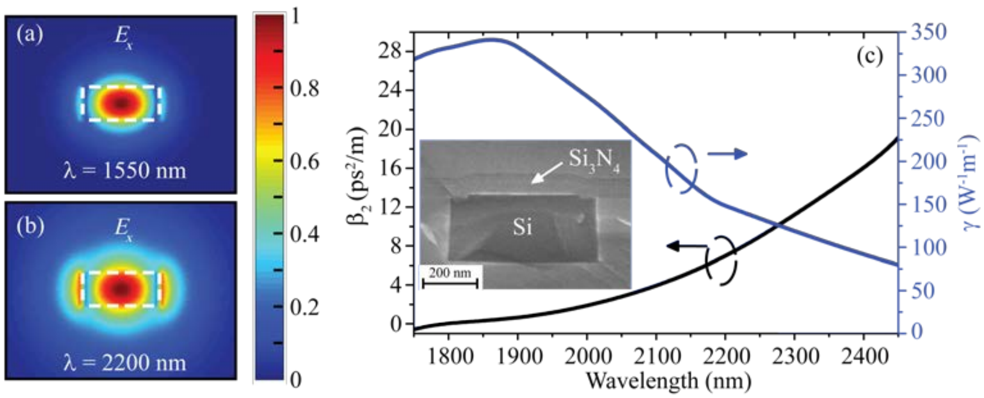

Figure 7-1 Optical properties of Si nanophotonic wire with $h \times w$ = 220 nm × 600 nm. Mode profile of the fundamental quasi-TE mode (a) at 1550 nm, (b) at 2200 nm. The dotted lines illustrate the boundary of the Si wire. The colormap/colorbar defines the normalized amplitude of the E_x field component. (c) Wavelength-dependent second-order dispersion (black curve) and effective nonlinearity parameter (blue curve). Inset: SEM cross-section of the Si nanophotonic wire.

Figure 7-1(a) and (b) show the calculated electric field E_x profiles of the fundamental quasi-TE mode at wavelengths of 1550 nm and 2200 nm respectively using the approach described in Section 2.1 of Chapter 2. This silicon nanophotonic wire has a power confinement κ of 92% at 1550 nm, and, since the mode expands at longer wavelengths, the power confinement drops to 75% at 2200 nm. The wavelength-dependent second-order dispersion β_2 and effective nonlinearity parameter γ for the fundamental quasi-TE mode are shown in Figure 7-1(c). The effective nonlinearity γ is calculated using the method described in Section 2.2.1 of Chapter 2. The effective nonlinearity of the Si nanophotonic wire (blue curve) decreases substantially as the wavelength increases, i.e. from ~ 300 $W^{-1}m^{-1}$ at 1750 nm to ~ 75 $W^{-1}m^{-1}$ at 2450 nm. This is largely due to decreasing mode confinement within the Si wire core, as seen in Figure 7-1(a) and (b). The reduced effective nonlinearity could be mitigated by choosing slightly larger Si core dimensions for improved optical confinement, when optimizing Si nanophotonic wires for operation in the mid-IR near ~ 2200 nm. The waveguide dispersion information, calculated using the method described in Section 2.1 of Chapter 2, is shown in the black curve of Figure 7-1(c). Normal dispersion prevails over the wavelength range from 1775 nm to 2450 nm due to the reduced contribution of waveguide dispersion, again due to weaker optical confinement within the Si core. The worst-case dispersion ($|\beta_2| < 20$ ps^2/m) yields a dispersion length of $L_D = T_0^2/\beta_2 > 200$ mm, where T_0 (~2 ps) is the FWHM of the picosecond pulses used in this work. This dispersion length is much larger than the length of the Si nanophotonic wire (~ 4 mm), and therefore dispersion is expected to have minimal impact upon pulse propagation.

7.3 Experiments

7.3.1 Measurement configuration

The experimental setup for the measurement of both the linear and nonlinear mid-IR propagation characteristics of the nanophotonic wires is shown in Figure 7-2(a). A pulse train of ~2 ps FWHM pulses is generated by a Ti:sapphire-pumped tunable optical parametric oscillator (OPO) system (Coherent Mira-OPO), and then fiber coupled using an objective lens. The pulse repetition rate is 76 MHz. The pump power coupled into the fiber is controlled using a neutral density (ND) filter. The center wavelength of the pump is tuned over the spectral range 1700-2300 nm by changing the cavity length of the OPO system, and is monitored along with its time-average power by a mid-IR optical spectrum analyzer (OSA; Yokogawa AQ6375). The pulse train is coupled into and out-of the Si nanophotonic wire chip via tapered lensed fibers, while the polarization of the pulses is aligned to excite the fundamental quasi-TE mode using an in-line fiber polarization controller. The transmitted pulse at the nanophotonic wire output is then directed to the OSA for analysis.

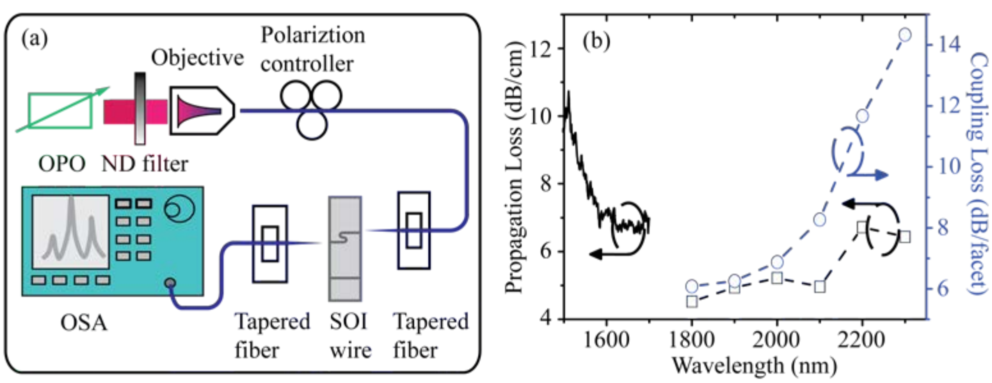

Figure 7-2 (a) Schematic of the experimental setup. (b) Si nanophotonic wire propagation loss across the telecommunication bands and the mid-IR region, and coupling loss between lensed fiber and SiO_xN_y mode converter in the mid-IR region.

The peak pump power P_P at the nanophotonic wire input is calculated using the expression $P_P = P_{avg}/(F\tau)$. Here, P_{avg} is the time-average input power integrated over the input pump spectrum, scaled by the wavelength-dependent fiber coupling loss (Figure 7-2(b), explained further in Section 7.3.2), F is the repetition rate of the OPO, and τ is the pulse duration.

7.3.2 Linear propagation loss

The propagation loss of the fundamental quasi-TE mode for the Si nanophotonic wire is measured using the cut-back method (comparing relative transmission through 4 mm-long and 20 mm-long wires) at several discrete input wavelengths across the TPA edge of Si. To avoid nonlinear loss, measurements are performed with the input peak power attenuated to less than 0.25 mW. The measured loss is shown as a black dashed line through square black data points in Figure 7-2(b), and ranges from 4.5 dB/cm to 7 dB/cm. For comparison, the propagation loss across the telecommunication bands is also shown in Figure 7-2(b) (solid black curve, measured with 1500-1700 nm broadband LED source). This data shows that within the mid-IR wavelength region < 2100 nm the linear propagation loss of this wire is significantly less than that in the telecommunication bands. The propagation loss decreases with increasing wavelength, approximately following the expected behavior for Rayleigh scattering in such a waveguide [34]. However, this loss also shows a perceptible increase when the wavelength approaches 2200 nm, most likely due to a) absorption loss from the outer cladding of the nanophotonic wire, i.e., SiO_2 [35], or b) mode leakage into the Si substrate. Such losses could be mitigated by using low-loss conformal spacer layers, e.g. air [36], Al_2O_3 [27], Si_3N_4 [35, 37], etc., and/or by increasing the BOX layer thickness [21, 35]

Also shown in Figure 7-1(b) is the wavelength-dependent facet coupling loss between lensed tapered fiber and the SiO_xN_y mode-converter, as illustrated by the blue dashed line through blue circle data points. While the loss is measured to be ~ 5 dB/facet at 1800 nm, the loss becomes larger than 12 dB for wavelengths ≥ 2200 nm. Facet coupling loss is larger at long wavelengths because the SiO_xN_y mode-converter used here was of a design previously optimized for operation at 1550 nm [32, 33].

7.3.3 Self-phase modulation versus input wavelength

It is important to characterize the optical parameters describing nonlinear wave propagation in Si nanophotonic wires. Here a series of SPM experiments are utilized to assess both the nonlinear refractive index n_2 and the two-photon absorption coefficient β_{TPA} as a function of wavelength. The behavior of SPM is characterized at four different pump wavelengths. The measured power-dependent transmission spectra at the center wavelengths 1775 nm, 1988 nm, 2200 nm, and 2250 nm are shown in Figure 7-3(a)-(d), respectively. For each input wavelength, output transmission spectra are recorded at several values of input peak power; these wavelengths are designated by the color-coding shown in the upper-right corner of each panel.

Figure 7-3 illustrates the development of an increasing number of sharp spectral fringes as the peak pump power increases for all input wavelengths, both above and below the TPA edge near 2200 nm. The observed spectra exhibit clear indications of self-phase modulation (SPM) of the input picosecond pulse, via the strong Kerr nonlinearity of the Si nanophotonic wires. The increasing coupling loss between the lensed tapered fibers and the SiO_xN_y mode-converters (Figure 7-2(b)) limits the maximum peak power level achievable at the waveguide input, and accordingly the total number of fringes observed across the pump spectrum decreases with increasing wavelength. Moreover, the number of fringes and their related total nonlinear phase shift vary sub-linearly with peak power due to the nonlinear loss in the waveguide [1], particularly at wavelengths less than 2200 nm where the effects of TPA are most pronounced.

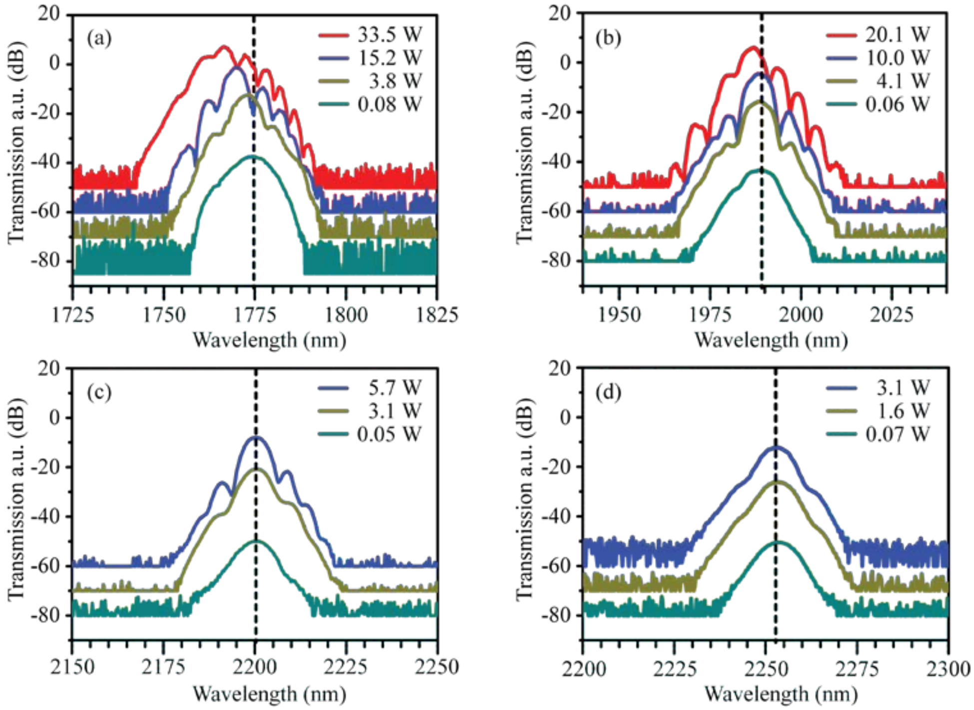

Figure 7-3 Experimental power-dependent transmission spectra as a function of pump center wavelength: (a) 1775 nm, (b) 1988 nm, (c) 2200 nm, (d) 2250 nm. Center wavelengths of the input pulse are indicated by the dashed line. The power levels indicated by the labels within each panel refer to the peak power at the input of the Si nanophotonic wire. Spectra have been vertically offset relative to each other by 10 dB for clarity.

Note that except for when the pump is centered at 1775 nm with a peak power of 33.5 W, the mid-IR experimental spectra here do not exhibit the significant spectral broadening observed in previous telecom-band SPM experiments with Si nanophotonic wires [1, 8, 9]. This general lack of broadening is a consequence of the fact that the input pump pulse is not transform-limited, but has a time-bandwidth product of ~ 1.5 for all four input wavelengths, as suggested by separate autocorrelation and pump spectrum measurements. Note that a similar effect has previously been observed in optical fibers [38], and attributed to the fact that the input pump pulse was negatively chirped. The effective “positive” chirp introduced by SPM [39] is largest at the highest experimental peak power ~ 33.5 W, which is obtained only at a wavelength of 1775 nm due to small on-chip coupling loss (Figure 7-2(b)). In this case alone, the positive chirp induced via SPM is sufficient to overcome the pump’s initial negative chirp, and thus substantial spectral broadening is observed. The negative chirp of the input pulse also explains why the SPM-induced spectral fringes consistently emerge from the red and blue “shoulders” of the pulse spectrum for all input wavelengths, rather than from the spectral peak, as typically occurs for an un-chirped pulse [38, 39].

To ensure that any observed nonlinearity originates solely from transmission through the Si nanophotonic wire, reference measurements with the Si wire removed from the optical path are performed, by directly coupling the tips of the tapered input/output fibers. Even at the highest input power levels used across all wavelengths in the above measurements, there is no observable SPM or nonlinear absorption. Therefore, the nonlinear contribution from all fiber components in the setup is found to be negligible.

7.4 Discussion

7.4.1 Self-limiting of transmission and mid-IR nonlinear loss

The power-dependent transmission spectra in Figure 7-3 are analyzed in greater detail to characterize the Si nanophotonic wire’s nonlinear loss as a function of input wavelength. For each set of input conditions, the output peak power is calculated as described in Section 7.3.1 above, using the integrated time-averaged power within the Si nanophotonic wire output spectrum. Figure 7-4(a) shows the nonlinear transmission response of the Si nanophotonic wire for wavelengths between 1775-2250 nm, obtained by plotting the output peak power versus the input peak power. The error bars in the figure reflect the power fluctuations (~ 1 dB) measured at the waveguide output. Note that the effects of inter-pulse free-carrier accumulation are negligible, since the 13.1 ns period between pump pulses is much larger than the free-carrier recombination lifetime (approximately 0.5-1 ns) in our sub-micrometer Si nanophotonic wires [40, 41].

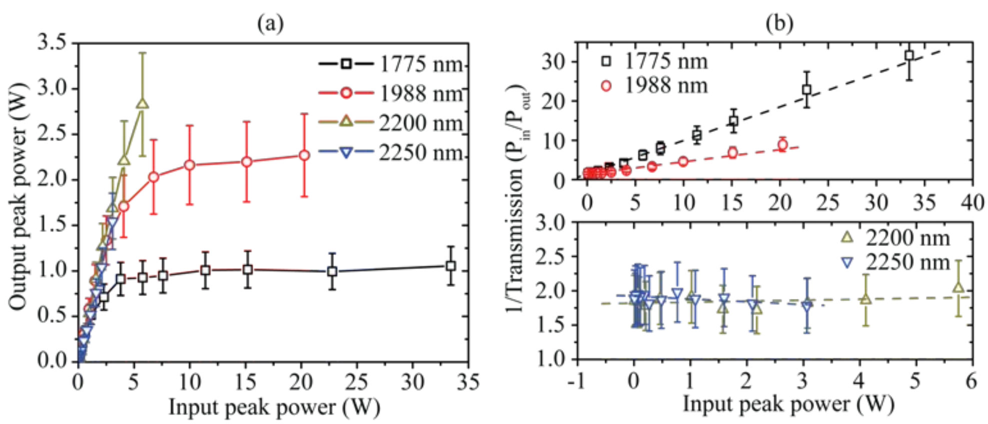

Figure 7-4 Characteristics of the nonlinear power transmission through the Si nanophotonic wire at four different input wavelengths. (a) Output peak power versus input peak power. (b) Reciprocal transmission coefficient versus input peak power.

At low input peak power (< 2 W), the output power shows a linear dependence upon input power for all four wavelengths. However, in the case of the two shortest wavelengths of 1775 nm and 1988 nm, the output power begins to saturate at input peak powers of ~ 2 W and ~ 2.5 W, respectively. In addition, the data in Figure 7-4(a) clearly demonstrate an increase in the saturated output power level as the wavelength shifts toward the mid-IR TPA threshold. For example, the saturated output peak power increases from ~ 1 W at 1775 nm to ~ 2.3 W at 1988 nm. Despite significant coupling loss at the two longer wavelengths, high peak-power levels can still be obtained at both 2200 nm (~ 6 W) and 2250 nm (~ 3 W). At these power levels, the transmission behavior is still within the linear regime for 2200 nm and 2250 nm, in contrast to the strongly saturating transmission observed for 1775 nm and 1988 nm at comparable input power. These results are anticipated due to the reduced TPA coefficient for wavelengths ≥ 2200 nm, and are in fact consistent with previously published experimental measurements on bulk silicon [24-26, 42].

Table 7-1 Values of β_{TPA} extracted from experimental data in Figure 7-4.

Wavelength (nm)	1775	1988	2200	2250
β_{TPA} (cm/GW)	1.4 ± 0.2	0.6 ± 0.1	0.03 ± 0.1	-0.06 ± 0.2

The value of the TPA coefficient β_{TPA} can be estimated from the slope of the reciprocal transmission ($1/T$ or P_{in}/P_{out}) versus input peak power [11, 43], as shown in Figure 7-4(b). Following the numerical approach described in [43] and using the slopes obtained from linear fits (dashed lines in Figure 7-4(b)), the β_{TPA} values extracted from the experimental data are listed in Table 7-1. The β_{TPA} values are estimated to be 1.4±0.2 cm/GW and 0.6±0.1 cm/GW for wavelengths of 1775 nm and 1988 nm, respectively. For the wavelength of 2200 nm, the estimated β_{TPA} value is significantly lower at 0.03±0.1 cm/GW. Note that this non-zero value of β_{TPA} occurs because the picosecond input pulse train has a significant spectral bandwidth centered at 2200 nm, and therefore samples an average of β_{TPA} coefficients from both above and below the theoretical TPA threshold at 2200 nm. This low value of the TPA coefficient facilitates efficient nonlinear processes, as has been illustrated by a recent report of greater than 25 dB on-chip parametric gain in a Si nanophotonic wire pumped at a wavelength of ~ 2200 nm [21]. At 2250 nm, the β_{TPA} value is estimated to be negative, at -0.06±0.2 cm/GW. However, the restricted range of accessible input power levels in our 2250 nm experiments produces a relatively large error bar as well as uncertainly in the mean value of β_{TPA}. Additional measurements with longer Si nanophotonic wires having lower facet coupling losses would be required in order to yield more accurate values of β_{TPA}, particularly at wavelengths near and immediately beyond silicon's TPA threshold.

In general, the β_{TPA} values reported in Table 7-1 are in reasonable agreement with those measured previously in bulk Si crystals using the z-scan technique [25, 26]. Quantitatively, these β_{TPA} values are approximately a factor of 1.5x larger than those reported in [25], and about a factor of 5x larger than reported in [26]. One potential source of discrepancies with comparison to bulk Si may originate from the fact that the fabrication processes used to define the Si nanophotonic wires (i.e., reactive ion etching, oxidation, deposition of cladding films by plasma-enhanced chemical vapor deposition, etc.) can create crystal damage at the surfaces and within the bulk of the wire. It is known that surface states [44] and bulk states from vacancies and/or interstitials [45] in silicon are capable of producing linear absorption at wavelengths longer than the bandedge wavelength of silicon. It is therefore possible to envision that such damage-induced bulk and surface states present in our Si nanophotonic wires may also contribute to nonlinear absorption at wavelengths near 2200 nm which would otherwise be free of TPA in bulk silicon crystals. Despite measurement uncertainties, the values of β_{TPA} in Table 7-1 provide useful experimental quantities for the design and modeling of future Si nanophotonic wire-based mid-IR nonlinear optical devices.

It is worthwhile to note that three photon absorption (3PA) has recently been revealed as the leading-order source of nonlinear loss for sufficiently high peak power (tens of Watts) pulse propagation experiments in Si near λ = 2200 nm [21, 46]. However, given the magnitude of the 3PA coefficient (γ_{3PA} ~ 0.025 cm^3/GW^2 at λ = 2170 nm), 3PA is not expected to contribute significantly to nonlinear loss at peak input power levels < 6 W and wavelengths > 2200 nm in the present experiments. An upper limit of nonlinear loss due to 3PA (in dB units) can be estimated by $\alpha = 10 \cdot \log(\exp(\gamma_{3PA}(\kappa P_P/A_0)^2 L))$, where γ_{3PA} is the 3PA coefficient, κ is power confinement factor, P_P is peak power in the Si nanophotonic wire, A_0 is the area of the silicon core, and L is the length of the Si nanophotonic wire. This estimation predicts a maximum nonlinear loss of 0.5 dB from 3PA within the 4 mm-long Si nanophotonic wire.

7.4.2 Free-carrier dispersion-induced spectral asymmetry

The SPM spectra in Figure 7-3 also reveal additional qualitative characteristics of nonlinear pulse transmission through the nanophotonic wire as the input wavelength is scanned across the TPA threshold of silicon. For example, at the lower values of input power shown in Figure 7-3(a)-(d), the spectral fringes appear symmetrically on both sides of the pump spectrum for all input wavelengths. At higher input powers, the total number of fringes increases, as expected due to the increasing nonlinear phase accumulated across the pump spectrum. However, the fringes become distributed asymmetrically, i.e.

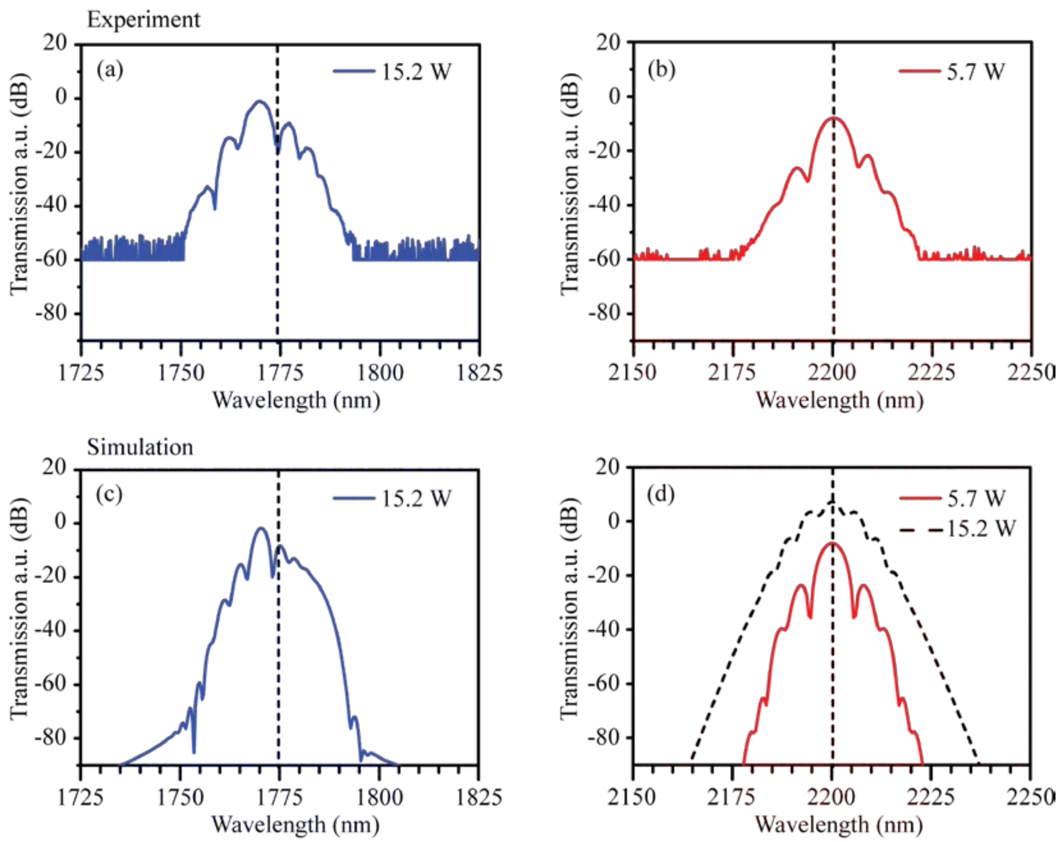

Figure 7-5 Comparison of SPM fringe asymmetry and spectral blue-shift between 1775 nm and 2200 nm input wavelengths, using experimental and simulated data. (a) Experimental spectrum at 1775 nm wavelength with coupled peak power of 15.2 W. (b) Experimental spectrum at 2200 nm wavelength with peak coupled power of 5.7 W. (c) Simulated spectrum corresponding to conditions at 1775 nm. (d) Simulated spectrum corresponding to conditions at 2200 nm. The additional black dashed spectrum is a simulation performed for an input peak power condition of 15.2 W (not accessible in the experiments), in order to contrast the symmetric output at 2200 nm against that at 1775 nm in (c).

the fringes on the red side of the spectrum become spaced more closely together than those on the blue side. This effect is most particularly pronounced for input wavelengths below the TPA edge of silicon, i.e. 1775 nm and 1988 nm. Moreover, these same spectra show a significant spectral blue-shift at high input peak power levels, in contrast to the spectra at 2200 nm and 2250 nm.

These wavelength-dependent SPM fringe asymmetries and spectral blue-shift characteristics are highlighted in Figure 7-5(a)-(b), through a comparison of the experimental output spectra at wavelengths of 1775 nm (P_p = 15.2 W) and 2200 nm (P_p = 5.7 W). The notable difference in SPM spectral evolution correlates with the input wavelength being situated far below or near the TPA threshold of silicon. In fact, the observed fringe asymmetry and spectral blue-shift are consistent with the presence of intra-pulse free-carrier dispersion (FCD) effects [1, 8, 9], originating from TPA-generated free carriers.

In order to further confirm our understanding of the characteristic spectral differences observed across the TPA threshold, we use a perturbed nonlinear Schrödinger equation (NLSE) to numerically simulate picosecond pulse propagation in the Si nanophotonic wires as described in Section 2.2 of Chapter 2. The numerical model captures the negative linear chirp of the input pump pulses, the value of which is determined by fitting to the measured input pump spectral width. The wavelength-dependent dispersion and effective nonlinearity parameter in Figure 7-1(c) are incorporated into the model, as well as the values of β_{TPA} determined from the self-limiting measurements (Section 7.4.1 and Table 7-1). Finally, the model also uses the values of n_2 taken from measurements on bulk silicon [25, 26]. The important parameters used in the simulations are all summarized in Table 7-2.

Table 7-2 Parameters used in pulse propagation simulations at wavelengths of 1775 nm and 2200 nm.

Wavelength (nm)	1775	2200
Peak input power (W)	15.2	5.7
Pulse temporal FWHM (ps)	2	2
Pulse linear chirp	-3.6	-2.0
β_2 (ps^2/m)	0.02	7.0
γ (W^{-1}m^{-1})	326	150
β_{TPA} (cm/GW)	1.4	0.03
n_2 (cm^2/W)	11.4e-14	8e-14

In the NLSE solver discussed in Section 2.2 of Chapter 2, the field of input pump pulse is described by the expression $u(t) = P_p^{0.5}\exp[-2\ln 2(1+iC)(t/T_0)^2]$, where P_p is the peak power, C is the linear chirp and T_0 is the pulse FWHM. Converged results are obtained with a temporal step size ~ 7 fs and a spatial step size of $L_N/200$, where L_N is the nonlinear length defined as $L_N = (\gamma P_P)^{-1}$.

Figure 7-5(c)-(d) contain the simulated output transmission spectra calculated using the same values of input peak power as in the experimental data of Figure 7-5(a)-(b) (solid lines). As illustrated by comparison with Figure 7-5(a)-(b), the simulated spectra for both 1775 nm and 2200 nm input wavelengths agree qualitatively well with the spectra obtained from experiment. Moreover, although the maximum experimentally accessible peak pump powers were lower at 2200 nm as compared to 1775 nm, a simulated spectrum for which the pump power is increased to 15.2 W (black dashed curve in Figure 7-5(d)) confirms that spectral symmetry (i.e., symmetric SPM fringes and absence of blue-shift) is preserved at 2200 nm for pump power conditions comparable with those at 1775 nm. This result is consistent with the negligible impact of TPA-induced free-carrier generation and dispersion expected near and above the ~2200 nm TPA threshold. In fact, our model shows that the peak intra-pulse free-carrier density at the beginning of the Si nanophotonic wire is reduced by a factor of 60, from 6×10^{18} cm^{-3} at the wavelength 1775 nm to 1×10^{17} cm^{-3} at the wavelength of 2200 nm, when using the same coupled peak power value of 15.2 W.

The agreement between the experiments and simulations in Figure 7-5 gives confidence that the values of the nonlinear parameters n_2 (based upon bulk Si measurements) and β_{TPA} (extracted from self-limiting transmission experiments above) used as simulation inputs, in fact provide an accurate description of the mid-IR nonlinear characteristics of the Si nanophotonic wires. Moreover, we can also infer that the numerical tools used to compute the spatial mode distribution and waveguide dispersion are appropriate for precise mid-IR modeling.

7.5 Conclusion

This chapter describes an experimental and numerical study of mid-IR linear and nonlinear picosecond pulse propagation through a normally dispersive 4 mm-long Si nanophotonic wire. Using a set of input wavelengths which cross the silicon TPA threshold at ~ 2200 nm, characteristics of SPM and self-limiting transmission having markedly different behavior at longer versus shorter mid-IR wavelengths are demonstrated. Both quantitative and qualitative aspects of these experimental characteristics in the context of fundamental TPA and TPA-induced free-carrier generation/dispersion are interpreted. Through analysis of the experimental data as well as comparison with numerical simulations, it is illustrated that the nonlinear refractive index n_2 and the two-photon absorption coefficient β_{TPA} derived from measurements of bulk silicon can be used to model the mid-IR nonlinear transmission characteristics of Si nanophotonic wires with reasonably good accuracy. This appears to be the case even for deeply scaled waveguide structures in which the (non-ideal, damaged) patterned silicon surfaces are in close interacting proximity with the highly-confined optical mode.

Reference

1. E. Dulkeith, Y. A. Vlasov, X. G. Chen, N. C. Panoiu, and R. M. Osgood, "Self-phase-modulation in submicron silicon-on-insulator photonic wires," Optics Express **14**, 5524-5534 (2006).
2. I. W. Hsieh, X. G. Chen, J. I. Dadap, N. C. Panoiu, R. M. Osgood, S. J. McNab, and Y. A. Vlasov, "Ultrafast-pulse self-phase modulation and third-order dispersion in Si photonic wire-waveguides," Optics Express **14**, 12380-12387 (2006).
3. I. W. Hsieh, X. G. Chen, J. I. Dadap, N. C. Panoiu, R. M. Osgood, S. J. McNab, and Y. A. Vlasov, "Cross-phase modulation-induced spectral and temporal effects on co-propagating femtosecond pulses in silicon photonic wires," Optics Express **15**, 1135-1146 (2007).
4. M. A. Foster, A. C. Turner, J. E. Sharping, B. S. Schmidt, M. Lipson, and A. L. Gaeta, "Broad-band optical parametric gain on a silicon photonic chip," Nature **441**, 960-963 (2006).

5. M. A. Foster, A. C. Turner, R. Salem, M. Lipson, and A. L. Gaeta, "Broad-band continuous-wave parametric wavelength conversion in silicon nanowaveguides," Optics Express **15**, 12949-12958 (2007).

6. H. S. Rong, A. S. Liu, R. Jones, O. Cohen, D. Hak, R. Nicolaescu, A. Fang, and M. Paniccia, "An all-silicon Raman laser," Nature **433**, 292-294 (2005).

7. O. Boyraz and B. Jalali, "Demonstration of a silicon Raman laser," Optics Express **12**, 5269-5273 (2004).

8. Q. Lin, O. J. Painter, and G. P. Agrawal, "Nonlinear optical phenomena in silicon waveguides: Modeling and applications," Optics Express **15**, 16604-16644 (2007).

9. J. I. Dadap, N. C. Panoiu, X. G. Chen, I. W. Hsieh, X. P. Liu, C. Y. Chou, E. Dulkeith, S. J. McNab, F. N. Xia, W. M. J. Green, L. Sekaric, Y. A. Vlasov, and R. M. Osgood, "Nonlinear-optical phase modification in dispersion-engineered Si photonic wires," Optics Express **16**, 1280-1299 (2008).

10. I. W. Hsieh, X. G. Chen, X. P. Liu, J. I. Dadap, N. C. Panoiu, C. Y. Chou, F. N. Xia, W. M. Green, Y. A. Vlasov, and R. M. Osgood, "Supercontinuum generation in silicon photonic wires," Optics Express **15**, 15242-15249 (2007).

11. H. K. Tsang, C. S. Wong, T. K. Liang, I. E. Day, S. W. Roberts, A. Harpin, J. Drake, and M. Asghari, "Optical dispersion, two-photon absorption and self-phase modulation in silicon waveguides at 1.5 mu m wavelength," Applied Physics Letters **80**, 416-418 (2002).

12. C. Koos, L. Jacome, C. Poulton, J. Leuthold, and W. Freude, "Nonlinear silicon-on-insulator waveguides for all-optical signal processing," Optics Express **15**, 5976-5990 (2007).

13. R. M. Osgood, N. C. Panoiu, J. I. Dadap, X. Liu, X. Chen, I. W. Hsieh, E. Dulkeith, W. M. J. Green, and Y. A. Vlasov, "Engineering nonlinearities in nanoscale optical systems: physics and applications in dispersion-engineered silicon nanophotonic wires," Advances in Optics and Photonics **1**, 162-235 (2009).

14. H. S. Rong, Y. H. Kuo, A. S. Liu, M. Paniccia, and O. Cohen, "High efficiency wavelength conversion of 10Gb/s data in silicon waveguides," Optics Express **14**, 1182-1188 (2006).

15. R. Salem, M. A. Foster, A. C. Turner, D. F. Geraghty, M. Lipson, and A. L. Gaeta, "Signal regeneration using low-power four-wave mixing on silicon chip," Nature Photonics **2**, 35-38 (2008).

16. R. Salem, M. A. Foster, A. C. Turner, D. F. Geraghty, M. Lipson, and A. L. Gaeta, "All-optical regeneration on a silicon chip," Optics Express **15**, 7802-7809 (2007).

17. T. K. Liang, L. R. Nunes, T. Sakamoto, K. Sasagawa, T. Kawanishi, M. Tsuchiya, G. R. A. Priem, D. Van Thourhout, P. Dumon, R. Baets, and H. K. Tsang, "Ultrafast all-optical switching by cross-absorption modulation in silicon wire waveguides," Optics Express **13**, 7298-7303 (2005).

18. R. Dekker, A. Driessen, T. Wahlbrink, C. Moormann, J. Niehusmann, and M. Forst, "Ultrafast Kerr-induced all-optical wavelength conversion in silicon waveguides using 1.55 mu m femtosecond pulses," Optics Express **14**, 8336-8346 (2006).

19. W. Astar, J. B. Driscoll, X. P. Liu, J. I. Dadap, W. M. J. Green, Y. A. Vlasov, G. M. Carter, and R. M. Osgood, "Conversion of 10 Gb/s NRZ-OOK to RZ-OOK utilizing XPM in a Si nanowire," Optics Express **17**, 12987-12999 (2009).

20. W. Astar, J. B. Driscoll, X. P. Liu, J. I. Dadap, W. M. J. Green, Y. A. Vlasov, G. M. Carter, and R. M. Osgood, "All-Optical Format Conversion of NRZ-OOK to RZ-OOK in a Silicon Nanowire Utilizing Either XPM or FWM and Resulting in a Receiver Sensitivity Gain of similar to 2.5 dB," IEEE Journal of Selected Topics in Quantum Electronics **16**, 234-249 (2010).

21. X. P. Liu, R. M. Osgood, Y. A. Vlasov, and W. M. J. Green, "Mid-infrared optical parametric amplifier using silicon nanophotonic waveguides," Nature Photonics **4**, 557-560 (2010).

22. S. Zlatanovic, J. S. Park, S. Moro, J. M. C. Boggio, I. B. Divliansky, N. Alic, S. Mookherjea, and S. Radic, "Mid-infrared wavelength conversion in silicon waveguides using ultracompact telecom-band-derived pump source," Nature Photonics **4**, 561-564 (2010).

23. A. C. Turner-Foster, M. A. Foster, R. Salem, A. L. Gaeta, and M. Lipson, "Frequency conversion over two-thirds of an octave in silicon nanowaveguides," Optics Express **18**, 1904-1908 (2010).

24. M. Dinu, F. Quochi, and H. Garcia, "Third-order nonlinearities in silicon at telecom wavelengths," Applied Physics Letters **82**, 2954-2956 (2003).

25. A. D. Bristow, N. Rotenberg, and H. M. van Driel, "Two-photon absorption and Kerr coefficients of silicon for 850-2200 nm," Applied Physics Letters **90**, 191104-191106 (2007).

26. Q. Lin, J. Zhang, G. Piredda, R. W. Boyd, P. M. Fauchet, and G. P. Agrawal, "Dispersion of silicon nonlinearities in the near infrared region," Applied Physics Letters **91**, 021111-021113 (2007).

27. T. Baehr-Jones, A. Spott, R. Ilic, B. Penkov, W. Asher, and M. Hochberg, "Silicon-on-sapphire integrated waveguides for the mid-infrared," Optics Express **18**, 12127-12135 (2010).

28. L. H. Yin, Q. Lin, and G. P. Agrawal, "Soliton fission and supercontinuum generation in silicon waveguides," Optics Letters **32**, 391-393 (2007).

29. J. D. Zhang, Q. Lin, G. Piredda, R. W. Boyd, G. P. Agrawal, and P. M. Fauchet, "Optical solitons in a silicon waveguide," Optics Express **15**, 7682-7688 (2007).

30. N. C. Panoiu, X. P. Liu, and R. M. Osgood, "Self-steepening of ultrashort pulses in silicon photonic nanowires," Optics Letters **34**, 947-949 (2009).

31. N. C. Panoiu, X. F. Chen, and R. M. Osgood, "Modulation instability in silicon photonic nanowires," Optics Letters **31**, 3609-3611 (2006).

32. J. Van Campenhout, W. M. J. Green, S. Assefa, and Y. A. Vlasov, "Low-power, 2x2 silicon electro-optic switch with 110-nm bandwidth for broadband reconfigurable optical networks," Optics Express **17**, 24020-24029 (2009).

33. S. Assefa, C. Jahnes, and Y. Vlasov, "CMOS compatible integrated dielectric optical waveguide coupler and fabrication," US Patent US7738753B2 (2010).

34. G. T. Reed and A. P. Knights, *Silicon Photonics: An Introduction* (Wiley, West Sussex, 2004).

35. R. A. Soref, S. J. Emelett, and A. R. Buchwald, "Silicon waveguided components for the long-wave infrared region," Journal of Optics a-Pure and Applied Optics **8**, 840-848 (2006).

36. R. Shankar, I. Bulu, R. Leijssen, and M. Loncar, "Silicon-Based Mid-Infrared Photonic Crystal Cavities," PECS-IX (2010).

37. Y. Yue, L. Zhang, R. G. Beausoleil, and A. E. Willner, "Ultrabroadband Low Dispersion Silicon-on-Nitride Waveguide in Mid-Infrared Region," Integrated Photonics Research, IWH4 (2010).

38. B. R. Washburn, J. A. Buck, and S. E. Ralph, "Transform-limited spectral compression due to self-phase modulation in fibers," Optics Letters **25**, 445-447 (2000).

39. G. P. Agrawal, *Nonlinear Fiber Optics* (Academic, San Diego, 2001).

40. Q. F. Xu, B. Schmidt, S. Pradhan, and M. Lipson, "Micrometre-scale silicon electro-optic modulator," Nature **435**, 325-327 (2005).

41. J. van Campenhout, W. M. J. Green, X. P. Liu, S. Assefa, R. M. Osgood, and Y. A. Vlasov, "Silicon-nitride surface passivation of submicrometer silicon waveguides for low-power optical switches," Optics Letters **34**, 1534-1536 (2009).

42. V. Raghunathan, R. Shori, O. M. Stafsudd, and B. Jalali, "Nonlinear absorption in silicon and the prospects of mid-infrared silicon Raman lasers," Physica Status Solidi a-Applications and Materials Science **203**, R38-R40 (2006).

43. H. K. Tsang, R. V. Penty, I. H. White, R. S. Grant, W. Sibbett, J. B. D. Soole, H. P. Leblanc, N. C. Andreadakis, R. Bhat, and M. A. Koza, "two-photon absorption and self-phase modulation in InGaAsP/InP multi-quantum-well wave-guides," Journal of Applied Physics **70**, 3992-3994 (1991).

44. T. Baehr-Jones, M. Hochberg, and A. Scherer, "Photodetection in silicon beyond the band edge with surface states," Optics Express **16**, 1659-1668 (2008).

45. M. W. Geis, S. J. Spector, M. E. Grein, R. T. Schulein, J. U. Yoon, D. M. Lennon, C. M. Wynn, S. T. Palmacci, F. Gan, F. X. Kaertner, and T. M. Lyszczarz, "All silicon

infrared photodiodes: photo response and effects of processing temperature," Optics Express **15**, 16886-16895 (2007).

46. S. Pearl, N. Rotenberg, and H. M. van Driel, "Three photon absorption in silicon for 2300-3300 nm," Applied Physics Letters **93**, 131102-131104 (2008).

Chapter 8

Higher-order phase matching, Raman-assisted parametric gain, and discrete-band parametric gain

8.1 Introduction

Nonlinear optical functions such as wavelength conversion and parametric amplification have been thoroughly investigated in single-mode [1] and photonic crystal fibers [2], as well as in chalcogenide [3] and silicon-on-insulator (SOI) planar integrated waveguide circuits [4-6]. The SOI platform is particularly appealing for four-wave mixing(FWM)-based optical-signal processing, as tight optical confinement in silicon nanophotonic wire waveguides, as well as the high intrinsic optical nonlinearity of crystal Si, give rise to extremely high nonlinear parameters [7, 8], enabling ultra-compact low-power devices to be realized. Moreover, the strong optical confinement permits application of waveguide-dispersion-engineering techniques to facilitate the required phase matching of the interacting signal, idler, and pump waves [9, 10].

While much of the literature on silicon-nanophotonic-wire nonlinear devices has described telecom-band pumps [4-7], recently experiments on wavelength conversion [11] and large on-chip/off-chip parametric amplification [12] have been reported using a mid-infrared (mid-IR) pump beam near the wavelength (λ = 2200 nm) of one-half the band gap. This wavelength choice avoids the parasitic effects of two-photon nonlinear absorption [13]. These demonstrations raise the interesting prospect of developing a SOI-photonics platform for mid-IR optical applications [14, 15] including free-space communication, medical diagnostics, and imaging. For example, one particularly attractive application would be to first, receive weak signals modulated onto a mid-IR optical carrier, followed by parametric wavelength conversion amplification using four-wave mixing, and finally by detection of the amplified signal using high-sensitivity telecom-band optical receivers. These receivers could be based upon established commercially-available III-V semiconductor technologies (i.e. InGaAs), or silicon nanophotonic wire-integrated detectors fabricated via heterogeneous (i.e. III-V) or monolithic (i.e. Ge, SiGe) approaches. Using such receivers to process a wavelength-converted mid-IR signal could potentially offer a large sensitivity enhancement over traditional direct-mid-IR-detection approaches, based upon narrow band-gap semiconductors such as HgCdTe or GaSb, and could also alleviate the need for low-temperature detectors.

In this chapter, higher-order waveguide dispersion terms are exploited to achieve phase matching 1) in a wide spectral band in the vicinity of the mid-IR pump, and 2) in discrete bands widely separated from the pump, which allow for frequency conversion of optical signals from the mid-IR into the telecom-wavelength range. By utilizing a 2-cm-long low-loss dispersion-engineered silicon nanophotonic wire, strong mid-IR parametric fluorescence, or modulation instability (MI) [16, 17], which covers a bandwidth > 580 nm in the vicinity of the pump at λ = 2173 nm, is demonstrated. The visibility of intense MI correlates with very large values of on-chip parametric gain, i.e. > 40 dB. In addition, on-chip gain can exceed 50 dB in some narrow spectral regions that are assisted by stimulated Raman scattering. When the pump wavelength is shifted to 1946 nm to achieve a different phase matching condition, strong frequency conversion of optical signals between the mid-IR and the telecom wavelength is demonstrated on the same waveguide. Conversion gain and parametric amplification of up to 19.5 dB and 18.8 dB are achieved using a pump wavelength of 1946 nm with a peak power of 37.3 W, respectively.

8.2 Higher-order phase matching

In order to determine phase matching, it is first necessary to consider the frequency dependence of the propagation constant, β. This dependence can be expressed using its Taylor series expansion at the pump frequency,

$$\beta(\Delta\omega) = \beta_0^p + \sum_1^{\infty} \frac{1}{n!} \frac{d^n\beta}{d\omega^n}\bigg|_{\beta=\beta_0^p} (\Delta\omega)^n = \beta_0^p + \sum_1^{\infty} \frac{1}{n!} \beta_n^p (\Delta\omega)^n \tag{8.2.1}$$

where β_0^p is the propagation constant at pump frequency, β_n^p is pump's nth-order dispersion coefficient (for details, see Section 2.1 in Chapter 2), and $\Delta\omega$ is the frequency detuning from pump. Thus, the linear part of phase mismatch for a degenerate FWM process ($2\omega_p = \omega_s + \omega_i$) can be fully characterized by using the even waveguide-dispersion term at the pump-wavelength/frequency:

$$\Delta k_l = 2\beta_0^p - \beta_0^s - \beta_0^i = -2\sum_1^{\infty} \frac{\beta_{2n}^p}{(2n)!} (\Delta\omega)^{2n} \tag{8.2.2}$$

where β_0^s and β_0^i are the propagation constant for signal and idler, and $\Delta\omega = |\omega_p - \omega_s| = |\omega_p - \omega_i|$ is the frequency detuning between pump and signal/idler. In case of small, frequency detuning, i.e. when working in a region near the pump, the linear (i.e. non-power dependent) phase matching behavior for a degenerate FWM process can be approximated by using the waveguide dispersion up to the second order such that

$\Delta k_l \approx -\beta_2^p \left(\Delta\omega\right)^2$; in this case anomalous dispersion with negative β_2 can lead to phase matching. Indeed parametric gain can be achieved in a spectral region near the pump by a pumping silicon nanophotonic wire in the anomalous dispersion regime [4, 12].

However in certain cases when parametric-frequency-conversion-gain bandwidth extends to wavelengths far from the pump (i.e. conversion of mid-IR signals to the telecom band), it becomes necessary to take higher-order dispersion terms into account. When dispersion up to the 4th order β_4^p is retained, the equation governing the power-dependent phase matching condition [16] becomes

$$\Delta k = 2\gamma_p P_p - \Delta k_l = 0 \Rightarrow 2\gamma_p P_p \approx -\beta_2^p \left(\Delta\omega\right)^2 - \beta_4^p \left(\Delta\omega\right)^4 / 12 \qquad (8.2.3)$$

where $2\gamma_p P_p$ is the nonlinear phase shift, γ_p is the waveguide effective nonlinearity parameter at the pump wavelength, and P_p is the peak power of the pump in the silicon nanophotonic photonic wire. Figure 8-1(a)-(d) shows the graphic solutions to Eq. (8.2.3) corresponding to four different nontrivial combinations of β_2 and β_4. Solutions exist when the frequency-detuning-dependent $\Delta k_l = -\beta_2^p \left(\Delta\omega\right)^2 - \beta_4^p \left(\Delta\omega\right)^4 / 12$ curve intersects the constant value of $\Delta k_l = 2\gamma_p P_p$. Consider now the four quadrants of dispersion space: First, I) As shown in Figure 8-1(a), when both β_2 and β_4 are positive, there is no solution to Eq. (8.2.3), which indicates no phase-matching point. II) However, there exists one phase-matching point as shown in Figure 8-1(b), when β_2 remains positive but β_4 becomes negative. This region of dispersion space has been used to achieve amplification in fiber optical parametric amplifiers, which are pumped in the normal dispersion regime [2], where the fiber exhibits negative fourth-order dispersion.

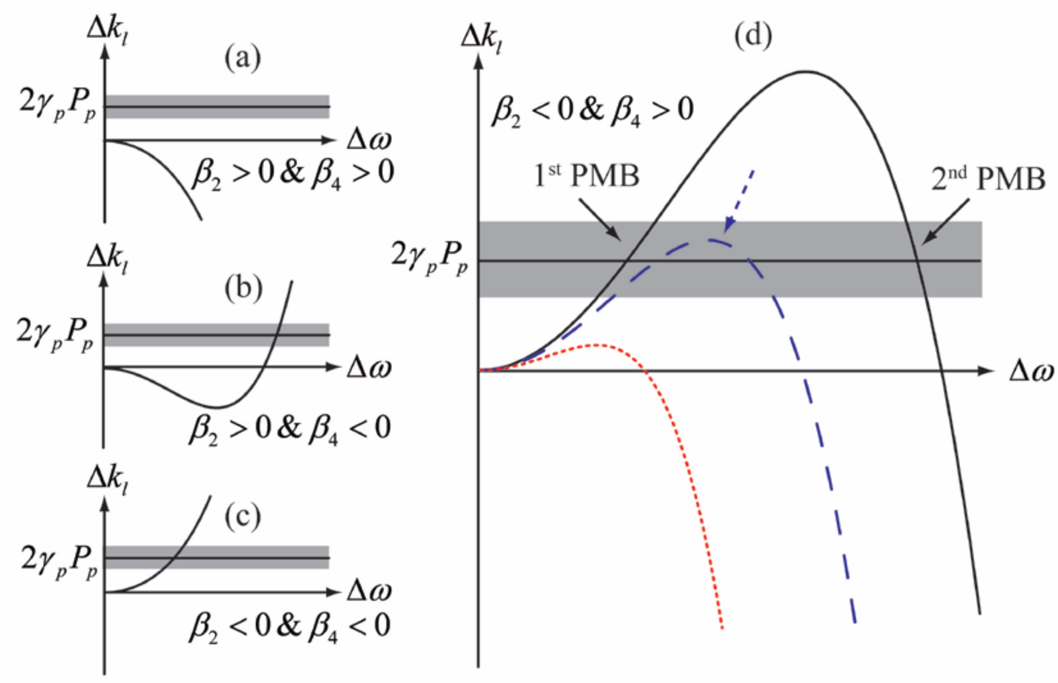

Figure 8-1 Graphic solutions for Eq. (8.2.3) four different nontrivial combinations of β_2 and β_4 : (a) $\beta_2 > 0 \,\&\, \beta_4 > 0$, (b) $\beta_2 > 0 \,\&\, \beta_4 < 0$, (c) $\beta_2 < 0 \,\&\, \beta_4 < 0$, (d) $\beta_2 < 0 \,\&\, \beta_4 > 0$. In (d), dotted-red, dashed-blue and solid-black curves show three representative cases under the condition of $\beta_2 < 0 \,\&\, \beta_4 > 0$; dashed-blue arrow indicates broadband phase matching; solid-black arrows indicate two phase matching bands; PMB: phase matching band. Shadowed areas in (a)-(d) indicate the phase detuning, within which efficient FWM can be achieved.

III) In addition, in case of both β_2 and β_4 exhibiting negative values as shown in Figure 8-1(c), there is only one phase matching point. IV) Finally Figure 8-1(d) shows the most interesting case where β_2 is negative but β_4 is positive. In some cases, as is shown by the example of the red-dotted curve, there is no phase matching point. This is due to the fact that the negative contribution to the linear phase mismatch term from 4th-order dispersion $-\beta_4^p(\Delta\omega)^4/12$ suppresses the positive contribution from 2nd-order dispersion $-\beta_2^p(\Delta\omega)^2$ and prevents the overall linear phase mismatch from reaching a value of $2\gamma_p P_p$. However, if 4th-order dispersion is somewhat smaller, the two dispersion orders can balance each other in the vicinity of $\Delta k_l = 2\gamma_p P_p$, as shown in the dashed-blue curve. In this case, there is a broad frequency-detuning range (indicated by the dashed-blue arrow) where the linear phase mismatching lies within the phase detuning range ($\delta k = 2\gamma_p P_p \pm 2\pi / L$, where L is the length of the waveguide [16]) as indicated in shadow area. This condition can enable very broadband phase matching and therefore broadband parametric amplification/wavelength conversion. Finally, if the positive contribution from β_2^p is even larger , the peak linear phase mismatch will reach its maximum well above $2\gamma_p P_p$, as shown in the solid-black curve, thus giving rise to a second phase-matching point, around which parametric gain becomes possible, albeit over a narrow, almost discrete band as is indicated by an arrow in Figure 8-1(d).

8.3 Waveguide properties

Our silicon nanophotonic wire was fabricated on a 200 mm silicon-on-insulator (SOI) wafer in a CMOS pilot line at *Ghent University-IMEC*. It had cross-sectional dimensions of w = 900 nm by h = 220 nm (inset Figure 8-2), and was 2 cm in length. The cladding consisted of air above and a 2 μm buried oxide (BOX) below the waveguide. The waveguide was designed to operate in the fundamental quasi-TE mode and had low propagation losses < 2.8 dB/cm for wavelengths from 2000 nm to 2500 nm. The waveguide loss here was reduced by more than 2× compared with that from prior work on mid-IR-pumped silicon nanophotonic-wire optical parametric amplifiers [12].

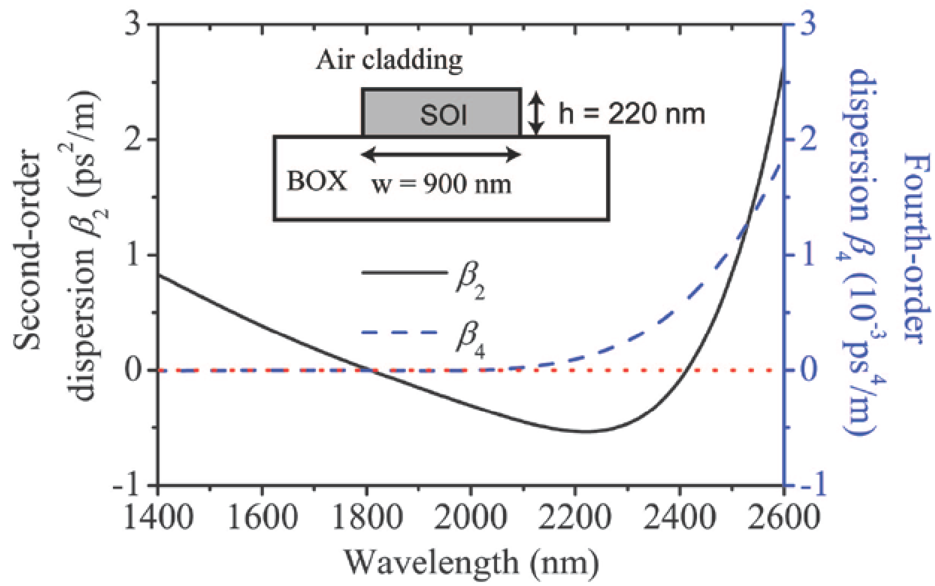

Figure 8-2 2nd-order (solid black curve) and 4th-order (dashed blue curve) dispersion of fundamental quasi-TE mode for the silicon wire: w = 900 nm, h = 220 nm, as shown in inset.

In our work, waveguide dispersion is simulated using the method described in Section 2.1 of Chapter 2. Simulations show that the engineered-waveguide dimensions produce anomalous dispersion conditions (2nd-order dispersion $\beta_2 < 0$) at wavelengths between the two zero-dispersion wavelengths of 1810 nm and 2410 nm as shown in Figure 8-2. Furthermore, this waveguide has small positive 4th-order dispersion ($\beta_4 > 0$) within the same wavelength range due to the positive curvature of the 2nd-order dispersion graph. Therefore, the balanced opposing signs of β_2 and β_4 should permit broad and discrete phase matching when this silicon nanophotonic wire is pumped within the range 1810 nm - 2410 nm.

8.4 Experiment results

In our experiments, the FWM pump is a picosecond pulse train (FWHM ~ 2 ps, repetition rate = 76 MHz) from a tunable optical parametric oscillator (OPO), and the probe is a cw signal from a tunable mid-IR laser. Both pump and probe are coupled into two separate single-mode optical fibers, and then multiplexed with a 90/10 fused fiber directional coupler. Coupling into/out of the 2 cm-long silicon nanophotonic wire is via edge coupling with lensed tapered fibers (coupling losses ~ 10 dB/facet). Polarization controllers are used to excite the quasi-TE mode with both pump and probe. The power and spectral information of transmitted light is analyzed on a mid-IR OSA (Yokogawa AQ6375).

8.4.1 Broadband MI and Raman assisted parametric gain

The input pump pulse has a center wavelength ~ 2175 nm and it shows a clean spectrum with a signal-to-noise ratio > 75 dB as illustrated by the dashed magenta curve in Figure 8-3(a). The peak pump power coupled into the silicon nanophotonic wire input is P_p ~ 13.5 W. Besides the usual self-phase modulation (SPM), see the oscillations on the central peak, and spectral blue-shift due to residual free-carrier dispersion [18, 19] (seen in comparison to the dashed magenta curve), the spectrum of transmitted pump (solid cyan curve of Figure 8-3(a)) exhibits significant modification compared with the input spectrum. The spectrum at the waveguide output is characterized by the emergence of a strong broadband MI spectrum extending from 1911 nm to 2486 nm. In addition, a prominent Raman Stokes peak rides on top of the MI spectrum at a wavelength of 2411 nm, frequency down-shifted from the pump by a Stokes shift of ~ 15.6 THz [20]. Moreover, a frequency up-shifted Raman anti-Stokes [21] peak at a wavelength of 1950 nm is visible. Furthermore, the small interference pattern visible around both narrowband Raman peaks originates from the additional phase shift introduced by the dispersion of the Raman susceptibility. This phase shift is superimposed upon the broadband FWM phase matching condition [3, 22], producing spectral fringes where phase matching for MI is disrupted.

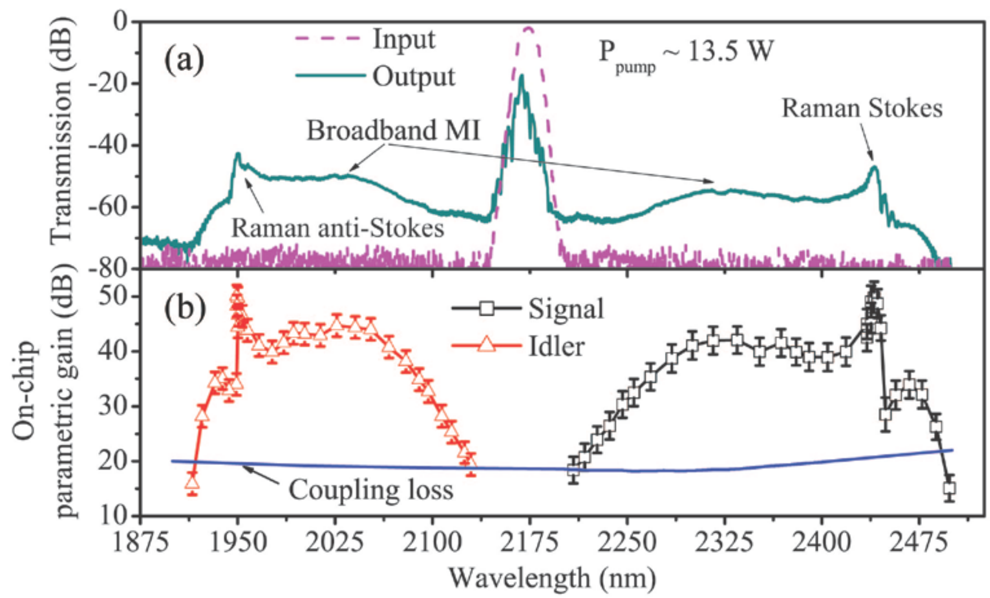

Figure 8-3 (a) Input (dashed magenta curve) and transmitted (solid cyan curve) pump spectra, illustrating broadband MI and Raman Stokes/anti-Stokes peaks. (b) On-chip parametric gain, exhibiting broadband on-chip amplification over a bandwidth > 580 nm, maximum Raman-assisted gain values of ~ 50 dB, unassisted FWM parametric gain of ~ 40 dB, and peak net off-chip gain > 30 dB.

The strong MI background suggests that the on-chip mid-IR parametric gain available is far larger than previously demonstrated [12]; note that in these studies MI was not observed. To probe the gain a cw signal is used with wavelengths varying from 2209 to 2498 nm (8 nm step size), generating the corresponding idler terms from 2129 to 1914 nm. The cw signal power coupled into the waveguide is kept < 0.05 mW to prevent pump depletion. The peak pump power remains the same as in the pump transmission measurement, P_p ~ 13.5 W. Figure 8-3(b) plots the measured on-chip amplification/conversion gain, defined using the method in [12]. The mid-IR-pumped silicon nanophotonic waveguide OPA exhibits on-chip optical parametric amplification over a bandwidth exceeding 580 nm. Near the Raman peaks, the OPA reaches a maximum Raman-assisted parametric signal/idler gain of ~ 50 dB. The gain profile exhibits the residue of an interference pattern at a wavelength ~ 2445 nm on the signal side and ~ 1950 nm on the idler side around the Raman-assisted peaks related to that seen in the MI spectrum of Figure 8-3(a). In particular, the number of interference fringes observed in Figure 8-3(b) is reduced, because the probe’s linewidth is broadened by cross-phase modulation and the 8 nm wavelength tuning steps are too coarse to resolve fine features. The OPA shows a net off-chip gain bandwidth of ~ 550 nm, with ~ 30 dB Raman-assisted off-chip gain for both signal and idler after compensating for all fiber-chip coupling losses from both facets (~ 20 dB, solid blue curve in Figure 8-3(b)). However, the OPA can be shown to have a maximum net off-chip optical gain of larger than 20 dB resulting solely from the parametric FWM process. In addition in comparison with the earlier results reported in Chapter 6 for a 4 mm-long silicon wire OPA [12], the peak operating pump power is reduced to less than half. At the same time, the maximum on-chip gain obtained using the 2 cm-long wire here shows an improvement of more than 25 dB, while the on-chip gain bandwidth is increased by more than 2.5×.

8.4.2 Converting mid-IR signals into telecom band wavelengths

Figure 8-4(a) and (b) show representative output spectra obtained with the pump pulse train located at a wavelength of 1946 nm, with a peak power of 37.3 W at the input of the nanophotonic wire. In Figure 8-4(a) only the pump propagates through the silicon wire. The strong broadband MI near the pump and Raman Stokes are clearly seen. Moreover, two additional discrete bands originating from higher-order phase matching

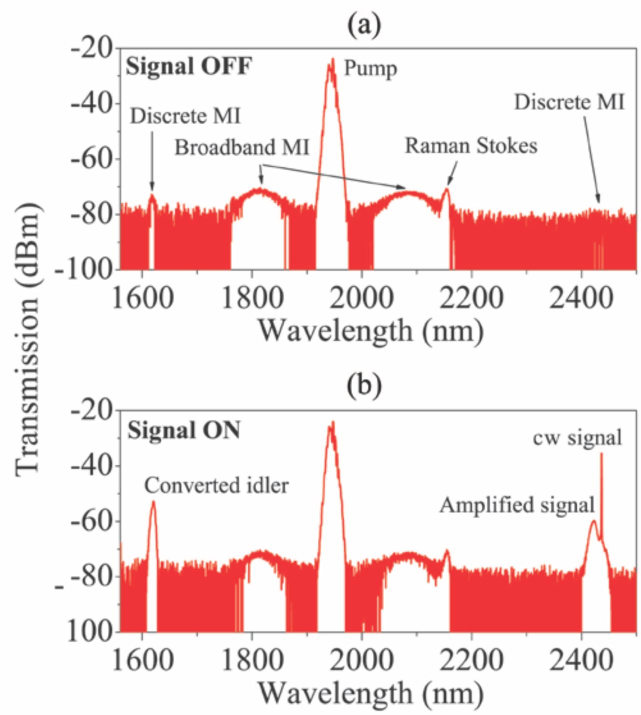

Figure 8-4 (a) Signal off: Modulation instability output spectrum generated by the exponential amplification of noise in the sidebands when pumping at 1946 nm. (b) Signal on: Parametric amplification of a continuous wave mid-IR signal at 2440 nm, and simultaneous conversion to a wavelength of 1620 nm.

are also visible in the MI spectrum, located at λ = 1620 nm and at λ = 2440 nm. This higher-order phase matching is discussed in the Section 8.2 in this chapter and is a direct consequence of the fact that the positive linear phase-mismatching contribution from β_2 grows much quicker with frequency detuning $\Delta\omega$ than the negative contribution from β_4. The output power in the 2440 nm peak is reduced due to higher input/output waveguide coupling losses at longer wavelengths. Figure 8-4(b) shows the spectrum when the discrete bands are probed by a cw mid-IR laser at 2440 nm. When the signal is tuned into this spectral band, it experiences exponential parametric gain, and is simultaneously wavelength converted to a telecom-band idler at 1620 nm. In addition, the signal and converted idler are broadened by cross-phase modulation due to the pulsed nature of the source.

By recording a series of similar spectra at different signal wavelengths, the parametric amplification and conversion efficiency can be determined as a function of wavelength within the discrete phase-matching bands [12]. This data is illustrated in Figure 8-5(a), indicating a peak net on-chip signal amplification of 18.8 dB and a conversion efficiency of 19.5 dB. The on-chip gain exceeds 10 dB over a bandwidth of 10 nm near the idler (1620 nm), and a bandwidth of 62 nm near the signal (2440 nm). The large values of idler-conversion gain indicate that silicon nanophotonic wires can potentially allow for efficient amplification of weak mid-IR signals and subsequent detection using commercially available high-sensitivity telecom receivers.

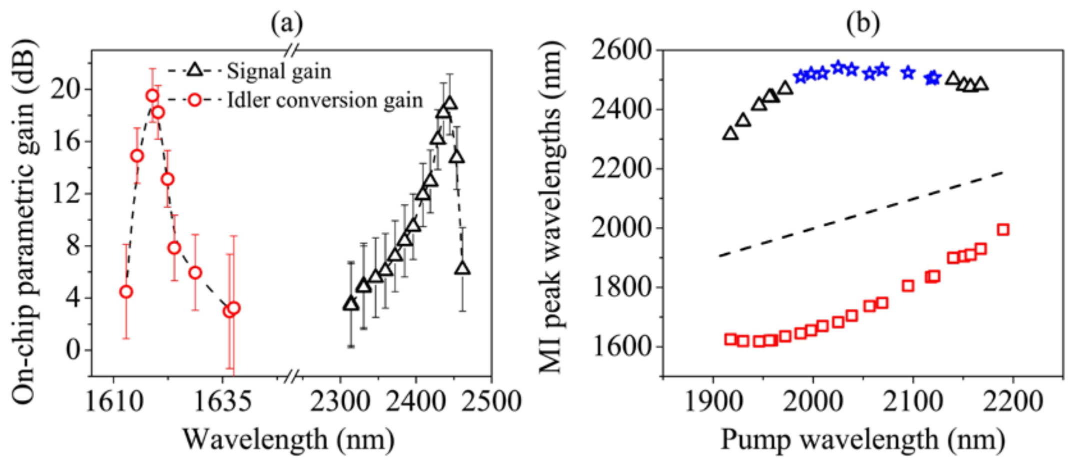

Figure 8-5 (a) On-chip parametric signal gain and idler-frequency conversion gain for the mid-infrared signals. Dashed lines are spline curves included to guide the eye. (b) Peak of the discrete modulation instability bands as a function of pump wavelength. The MI peaks indicated by the blue stars was not directly measurable, as they were located beyond the 2500 nm maximum-wavelength limit of the OSA used. Rather, the positions of these peaks were inferred from energy conservation. The dashed line tracks the position of the pump.

Figure 8-5(b) shows the location of the discrete bands as a function of pump wavelength (defined as the modulation-instability peak wavelength). Tuning the pump wavelength varies the dispersion at the pump and thus the linear phase mismatch accumulated along the silicon nanophotonic wire between pump, signal and idler waves (see Eq. (8.2.2)), and results in a spectral shift of the discrete bands where phase matching is obtained. The spectral separation of the bands becomes larger with increasing $|\beta_2|$ and decreasing $|\beta_4|$. The data illustrates that the discrete bands move closer to the pump wavelength when the pump approaches the zero dispersion wavelengths at 1810 nm and 2410 nm, i.e. when the magnitude of β_2 decreases. Further optimization of the wire dimensions so as to increase the second-order dispersion while simultaneously decreasing the fourth-order dispersion would make it possible to design a silicon wire capable of converting mid-IR signals directly to the C-band near 1550 nm.

8.5 Conclusion

This chapter has demonstrated that a major increase in the gain and bandwidth can be achieved over prior work on mid-IR-pumped silicon nanophotonic wire optical parametric amplifiers [12]. In addition, our work demonstrates use of higher-order phase matching in silicon nanophotonic wires to realize the conversion of signals from the mid-IR into the telecommunication band with a signal amplification of 18.8 dB and a conversion gain of 19.5 dB. These results are important since they can be applied to the processing of weak mid-IR signals using established high-sensitivity telecom-band optical-receiver technology. Our results also potentially offer a large sensitivity enhancement over traditional direct mid-IR detection approaches using narrow band-gap semiconductors. Moreover, our work shows that judicious dispersion engineering and improved wire loss characteristics can be leveraged to control and improve the bandwidth and gain, perhaps even extending the broad/discrete gain band to telecom wavelengths even near 1550 nm.

Reference

1. J. Hansryd, P. A. Andrekson, M. Westlund, J. Li, and P. O. Hedekvist, "Fiber-based optical parametric amplifiers and their applications," IEEE Journal of Selected Topics in Quantum Electronics **8**, 506-520 (2002).
2. J. D. Harvey, R. Leonhardt, S. Coen, G. K. L. Wong, J. C. Knight, W. J. Wadsworth, and P. S. J. Russell, "Scalar modulation instability in the normal dispersion regime by use of a photonic crystal fiber," Optics Letters **28**, 2225-2227 (2003).
3. M. R. E. Lamont, B. Luther-Davies, D. Y. Choi, S. Madden, X. Gai, and B. J. Eggleton, "Net-gain from a parametric amplifier on a chalcogenide optical chip," Optics Express **16**, 20374-20381 (2008).
4. M. A. Foster, A. C. Turner, J. E. Sharping, B. S. Schmidt, M. Lipson, and A. L. Gaeta, "Broad-band optical parametric gain on a silicon photonic chip," Nature **441**, 960-963 (2006).
5. M. A. Foster, A. C. Turner, R. Salem, M. Lipson, and A. L. Gaeta, "Broad-band continuous-wave parametric wavelength conversion in silicon nanowaveguides," Optics Express **15**, 12949-12958 (2007).
6. A. C. Turner-Foster, M. A. Foster, R. Salem, A. L. Gaeta, and M. Lipson, "Frequency conversion over two-thirds of an octave in silicon nanowaveguides," Optics Express **18**, 1904-1908 (2010).
7. R. M. Osgood, N. C. Panoiu, J. I. Dadap, X. Liu, X. Chen, I. W. Hsieh, E. Dulkeith, W. M. J. Green, and Y. A. Vlasov, "Engineering nonlinearities in nanoscale optical systems: physics and applications in dispersion-engineered silicon nanophotonic wires," Advances in Optics and Photonics **1**, 162-235 (2009).

8. C. Koos, L. Jacome, C. Poulton, J. Leuthold, and W. Freude, "Nonlinear silicon-on-insulator waveguides for all-optical signal processing," Optics Express **15**, 5976-5990 (2007).

9. A. C. Turner, C. Manolatou, B. S. Schmidt, M. Lipson, M. A. Foster, J. E. Sharping, and A. L. Gaeta, "Tailored anomalous group-velocity dispersion in silicon channel waveguides," Optics Express **14**, 4357-4362 (2006).

10. X. P. Liu, W. M. J. Green, X. G. Chen, I. W. Hsieh, J. I. Dadap, Y. A. Vlasov, and R. M. Osgood, "Conformal dielectric overlayers for engineering dispersion and effective nonlinearity of silicon nanophotonic wires," Optics Letters **33**, 2889-2891 (2008).

11. S. Zlatanovic, J. S. Park, S. Moro, J. M. C. Boggio, I. B. Divliansky, N. Alic, S. Mookherjea, and S. Radic, "Mid-infrared wavelength conversion in silicon waveguides using ultracompact telecom-band-derived pump source," Nature Photonics **4**, 561-564 (2010).

12. X. P. Liu, R. M. Osgood, Y. A. Vlasov, and W. M. J. Green, "Mid-infrared optical parametric amplifier using silicon nanophotonic waveguides," Nature Photonics **4**, 557-560 (2010).

13. A. D. Bristow, N. Rotenberg, and H. M. van Driel, "Two-photon absorption and Kerr coefficients of silicon for 850-2200 nm," Applied Physics Letters **90**, 191104-191106 (2007).

14. R. A. Soref, S. J. Emelett, and A. R. Buchwald, "Silicon waveguided components for the long-wave infrared region," Journal of Optics a-Pure and Applied Optics **8**, 840-848 (2006).

15. M. Ebrahim-Zadeh and I. T. Sorokina, *Mid-Infrared Coherent Sources and Applications* (Springer, Dordreht, 2007).

16. G. P. Agrawal, *Nonlinear Fiber Optics* (Academic, San Diego, 2001).

17. N. C. Panoiu, X. F. Chen, and R. M. Osgood, "Modulation instability in silicon photonic nanowires," Optics Letters **31**, 3609-3611 (2006).

18. J. I. Dadap, N. C. Panoiu, X. G. Chen, I. W. Hsieh, X. P. Liu, C. Y. Chou, E. Dulkeith, S. J. McNab, F. N. Xia, W. M. J. Green, L. Sekaric, Y. A. Vlasov, and R. M. Osgood, "Nonlinear-optical phase modification in dispersion-engineered Si photonic wires," Optics Express **16**, 1280-1299 (2008).

19. I. W. Hsieh, X. G. Chen, J. I. Dadap, N. C. Panoiu, R. M. Osgood, S. J. McNab, and Y. A. Vlasov, "Ultrafast-pulse self-phase modulation and third-order dispersion in Si photonic wire-waveguides," Optics Express **14**, 12380-12387 (2006).

20. V. Raghunathan, D. Borlaug, R. R. Rice, and B. Jalali, "Demonstration of a mid-infrared silicon Raman amplifier," Optics Express **15**, 14355-14362 (2007).

21. R. Claps, V. Raghunathan, D. Dimitropoulos, and B. Jalali, "Anti-Stokes Raman conversion in silicon waveguides," Optics Express **11**, 2862-2872 (2003).

22. A. S. Y. Hsieh, G. K. L. Wong, S. G. Murdoch, S. Coen, F. Vanholsbeeck, R. Leonhardt, and J. D. Harvey, "Combined effect of Raman and parametric gain on single-pump parametric amplifiers," Optics Express **15**, 8104-8114 (2007).

Chapter 9

Future research directions

The previous chapters have shown proof-of-principle experiments on mid-IR silicon-nanophotonic-wire-based optical parametric amplifiers/wavelength converters. These demonstrations raise the interesting prospect of developing a mid-IR SOI photonic platform by leveraging the existing CMOS photonic technologies. Driven by potential applications, there are several challenging future research directions in this platform. This brief chapter outlines these directions.

First, it is clear that new passive devices are required, since these devices are the essential building blocks for mid-IR technology and their performance determines the scope of applications that are possible for the SOI mid-IR platform. For example, a low-loss silicon nanophotonic wire is essential for applications involving parametric processes. Thus to avoid the increasing absorption loss in silicon dioxide incurred in moving into the mid-IR [1], a new kind of silicon waveguide system must be developed such as a suspended or partially suspended structure. In addition, a high-performance mode converter must also be developed for efficient power coupling of mid-IR wave from fibers into silicon nanophotonic wires [2]; the current polymer device has too much absorption at mid-IR wavelengths while the direct fiber-waveguide butt-coupling after cleaving through the silicon nanophotonic wires (chopping off the polymer coupler) has too much insertion loss.

A second direction will be to develop low-cost, highly reliable and efficient mid-IR light sources based on silicon. These light sources could potentially be used in medical diagnostics for ablating tissue by targeting resonant absorption peaks in water, amide bonds in collagen and other tissue chromophors [3, 4]. There are also potential applications in environmental science, such as the detection of pollutant gases and combustion products, and remote chemical and biological sensing [5]. As shown in Chapter 8, dispersion-engineered silicon nanophotonic wires are capable of very broad gain bandwidth. Therefore these silicon-based mid-IR light sources can be constructed in forms of a widely tunable optical parametric oscillator (OPO), or a multi-line oscillator. In this case the gain medium for the proposed tunable mid-IR OPO will be a low-loss dispersion-engineered silicon nanophotonic wire, which exhibits broadband gain near the pump wavelength. This OPO can be driven by a mid-IR pulsed pump with a peak power of tens of watts from an external solid-state laser system. It can be configured to oscillate in an external fiber-loop-based or free-space cavity, and wavelength tuning can be achieved by changing the optical-path length in the cavity. A multiline oscillator can be built on a high-Q dispersion-engineered mid-IR silicon micro-ring resonator and pumped by a cw mid-IR light coupled from an external laser system. With a readily achievable Q-factor $> 10^5$, the oscillation threshold could be designed to be < 100 mW coupled in the resonator.

A third research direction will be to investigate the feasibility of building an ultrahigh-speed mid-IR free-space communication link on this SOI mid-IR platform [5]. As shown in Chapter 8, very efficiency wavelength conversion between mid-IR and telecom L/U bands is possible using silicon nanophotonic wires. This demonstration is a clear indication that SOI platform has the potentials to bridge the spectral gap between mid-IR region and traditional telecommunication bands by efficient wavelength down/up conversion using the parametric processes. For the proposed ultrahigh-speed free-space mid-IR link, at the transmitter side, a data signal can be generated within the telecom bands using commercially-available high-performance telecom components and carried by an optical fiber; the signal will then be coupled into a silicon micro-ring resonator pumped by a mid-IR cw light and the carrier wavelength will be wavelength converted into mid-IR; the converted carrier will be coupled out of the silicon waveguide and transmitted into a free-space system. At the receiver side, the transmitted mid-IR signal will be collected and coupled back into a silicon micro-ring resonator for wavelength conversion with gain using the same principle; the converted signal will then be detected using the high-sensitivity and high-speed telecom receivers.

Reference

1. R. A. Soref, S. J. Emelett, and A. R. Buchwald, "Silicon waveguided components for the long-wave infrared region," Journal of Optics A-Pure and Applied Optics **8**, 840-848 (2006).
2. X. P. Liu, R. M. Osgood, Y. A. Vlasov, and W. M. J. Green, "Mid-infrared optical parametric amplifier using silicon nanophotonic waveguides," Nature Photonics **4**, 557-560 (2010).
3. B. Jalali, V. Raghtmathan, R. Shori, S. Fathpour, D. Dimitropoulos, and O. Stafsudd, "Prospects for silicon mid-IR Raman lasers," IEEE Journal of Selected Topics in Quantum Electronics **12**, 1618-1627 (2006).

4. B. Jalali and S. Fathpour, "Silicon photonics," Journal of Lightwave Technology **24**, 4600-4615 (2006).

5. M. Ebrahim-Zadeh and I. T. Sorokina, *Mid-Infrared Coherent Sources and Applications* (Springer, Dordreht, 2007).